INVESTIGATION OF THE PHOTOELECTROCHEMICAL OXYGEN EVOLUTION REACTION ON METAL OXIDE SEMICONDUCTORS

By

Soumik Das

A DISSERTATION

Submitted to
Michigan State University
in partial fulfillment of the requirements
for the degree of

Chemistry – Doctor of Philosophy

2024

ABSTRACT

Global warming and carbon emissions are among the most critical challenges of the 21st century. Hydrogen offers a promising solution to mitigate these issues. However, at the R&D level, the cost of hydrogen production is still three times that of gasoline. To commercialize hydrogen as a fuel, production costs must be reduced, particularly by enhancing the efficiency of hydrogen generation and by utilizing value-added products like oxygen generated at the anode.

Photoelectrochemical (PEC) water splitting has emerged as a viable research avenue for harnessing solar energy. This study focuses on using hematite as a photoanode material for solar water oxidation in a PEC cell, which produces oxygen—a critical and thermodynamically challenging counterpart to clean hydrogen production. Despite the hematite's attractive properties, such as good light absorption, suitable band positions, and robustness, experimental performance has consistently fallen short of theoretical expectations due to significant recombination processes that limit charge separation and collection. As a result, a large input voltage is required to oxidize water on hematite, leading to substantial efficiency losses.

In this work, hematite thin films prepared by atomic layer deposition and electrodeposition were systematically investigated under PEC conditions to explore the mechanisms of oxygen formation during water oxidation. A combination of electrochemical, photoelectrochemical, and spectroscopic analyses was employed to better understand the fundamental mechanisms behind the performance limitations under various light conditions. It was found that the hole transfer rate is highly dependent on illumination conditions, Fermi level position, and band structure.

Copyright by
SOUMIK DAS
2024

A dedication to four of the most important people in my life…
Sima Das (Maa), Chitta Ranjan Das (Baba), Soumyadeep Das (Bhai)
&
Snigdha Koner (Wife)
Without your continued love and support I wouldn't be where I am today
Thank you all

ACKNOWLEDGEMENTS

I would like to express my deepest gratitude to everyone who has supported me, both mentally and physically, throughout my PhD journey, contributing immensely to my growth as a researcher.

First and foremost, I am incredibly grateful to my advisor, Professor Thomas Hamann, for being an exceptional mentor. Your unwavering support, patience, and guidance have been instrumental in my continued progress, especially during challenging projects. I am deeply indebted to you for helping me navigate both failure and success.

I would also like to acknowledge the National Science Foundation (NSF) for funding my research, enabling me to pursue my academic endeavors.

I extend my heartfelt thanks to the past lab members—Austin, Parisa, Eric, Prabodha, Tea-yon Kim (Tim), Chenjia, and Suzi—who have not only been amazing colleagues but also dear friends and mentors. Your willingness to assist me whenever I needed help has been invaluable. To the current lab members—Femi, Xiaoyin, Chellammal, Samhita, and Michael—thank you for the stimulating discussions, spirited debates, and for making the lab an exciting and enjoyable place to work. I have truly cherished our scientific conversations and hope we stay connected. I wish you all the brightest future.

I am also grateful to my committee members, Prof. Gary Blanchard, Prof. Greg Swain and Dr. Seokhyoung Kim, for their insightful suggestions and guidance throughout my research.

A special thanks to the friends I've made over the past five years—Sourav Sil, Atanu Ghosh, Arnab Chakraborty, Joydeep Rakshit, Avirup Roy, Estak Ahmed, and Shreya Roychoudhury, Anshu Yadav, Pushpender Yadav. The camaraderie, afternoon banter,

and quick runs to Grand River restaurants have made life easier and more enjoyable, especially during tough times.

Finally, I am profoundly thankful to my parents and brother—for their endless support throughout these years. Most importantly, to my wife, who made the tremendous sacrifice of staying apart from me so I could pursue my dream career, I am forever grateful. I dedicate this dissertation to my mother for her unwavering devotion and support.

Cheers!

TABLE OF CONTENTS

LIST OF TABLES

LIST OF FIGURES

Chapter 1:

Introduction

1.1 Motivation

The last 50 years have brought unprecedented changes to our global landscape alongside tripling of our current population. This remarkable growth can be attributed to improvements in public health, nutrition, personal hygiene, and medicine, leading to an extended human lifespan.[1]

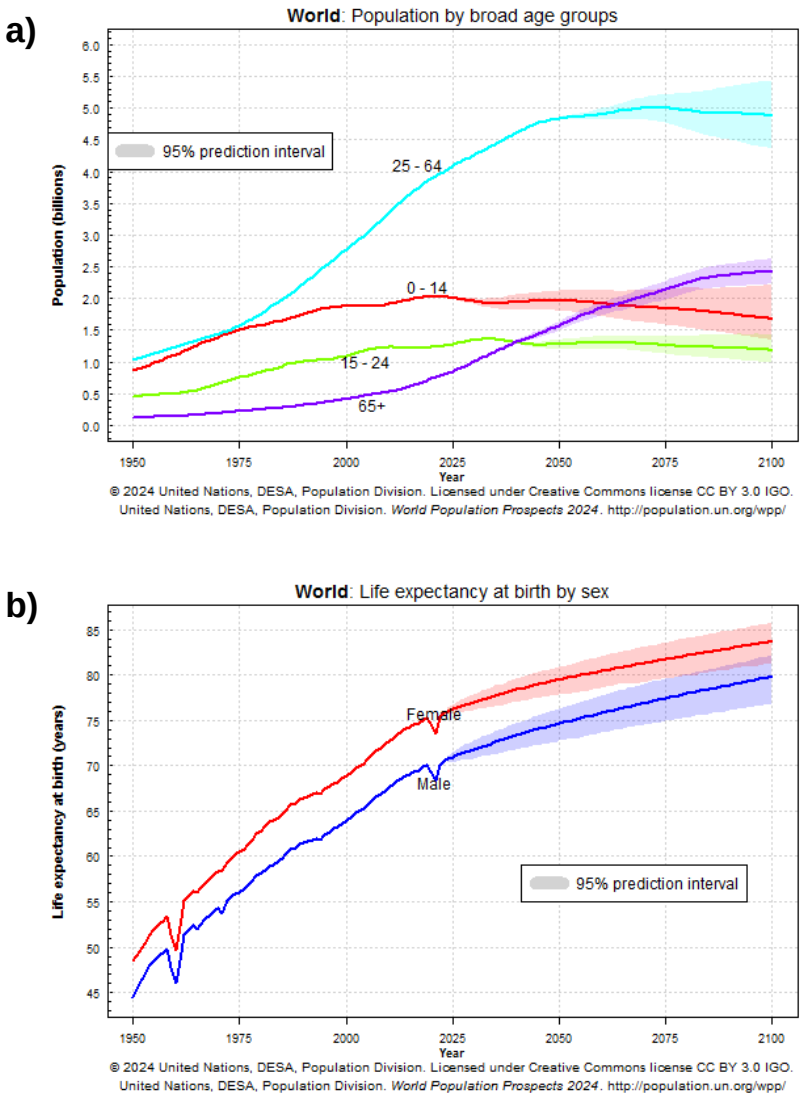

Figure 1.1: a) Prediction of World Population upto 2100 in different age group. b) Life expectancy of Male and Female is set to rise in next 70 years.[1]

As of today, the world's population is standing at 8 billion people and high and persistent fertility rates in certain countries contribute to this unprecedented increase. Interestingly, while it took 12 years for the global population to transition from 7 to 8 billion, the subsequent leap to 9 billion is expected to take approximately 15 years, signaling a slowdown in overall population growth. According to the current forecasts this number is going to reach 10 billion by 2050, alongside a continuous growth in our collective energy footprint. Unfortunately, rapid population expansion poses challenges to achieving the sustainable development goals, which represent humanity's best path toward a happy and healthy future.

Despite the environmental impact associated with population growth, it is rising per capita income that drives unsustainable patterns of production and consumption. Surprisingly, the countries with the highest consumption of material resources and greenhouse gas emissions are those where income per capita is higher, rather than those experiencing rapid population growth.[1]

Our current energy supply stands at 6.12 $x10^8$ terrajoules as of 2021.[2] 82% of the world's energy supply comes combinedly from Coal, Oil and Natural Gas; basically, non-

a)

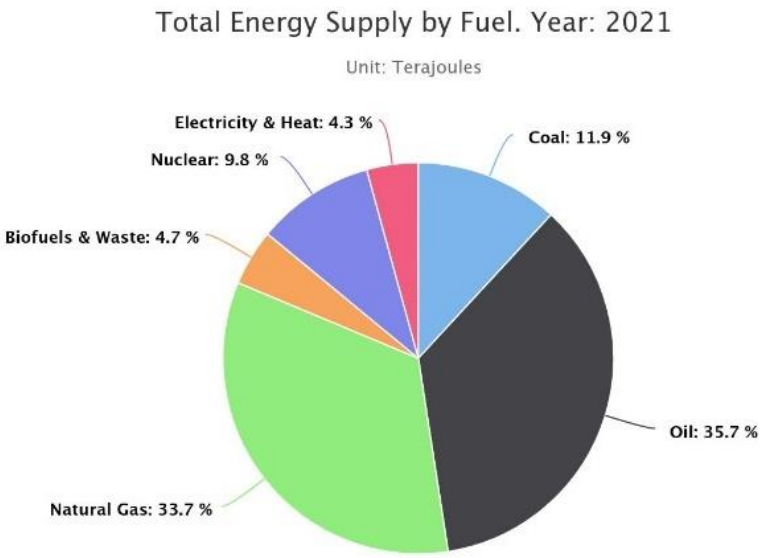

b)

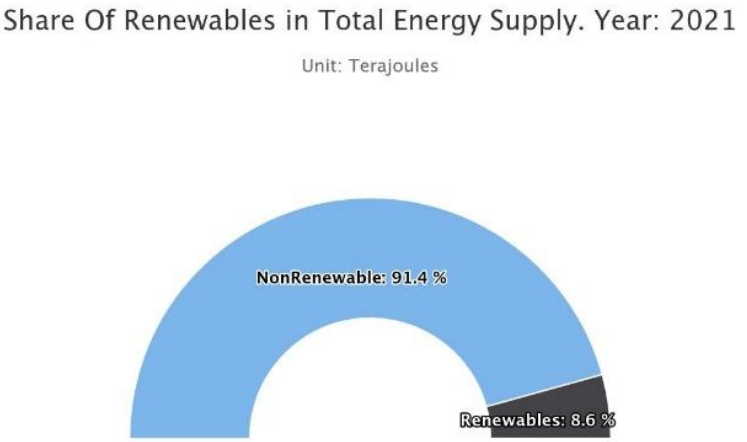

Figure 1.2: a) Total energy supply sources in the year of 2021. b) Still in 2021, non-renewable is still dominating but it is significantly down from previous years.[2]

renewable fossil fuels make up almost 91.4% share with respect to renewable, making the climate change transition from fossil fuel to renewable a huge political debate.[2]

The global fossil fuel industry, encompassing coal, oil, and gas, has seen significant growth in recent years. As of 2021, the market size was valued at $6.3 trillion [3] and is projected to reach $10.7 trillion by 2031. This growth is largely driven by increased demand due to globalization and industrialization. In 2022, fossil fuels accounted for 82% of global energy consumption,[2] with coal demand set to surpass 8 billion tons for the first time,[4] oil consumption reaching approximately 97.3 million barrels per day, [5] and natural gas consumption at 132,290,211 million cubic feet per year. However, the excessive use of fossil fuels has raised concerns about environmental sustainability and long-term energy security. As the world continues to globalize, the demand for fossil fuels is expected to rise, further driving the growth of the industry.[6]

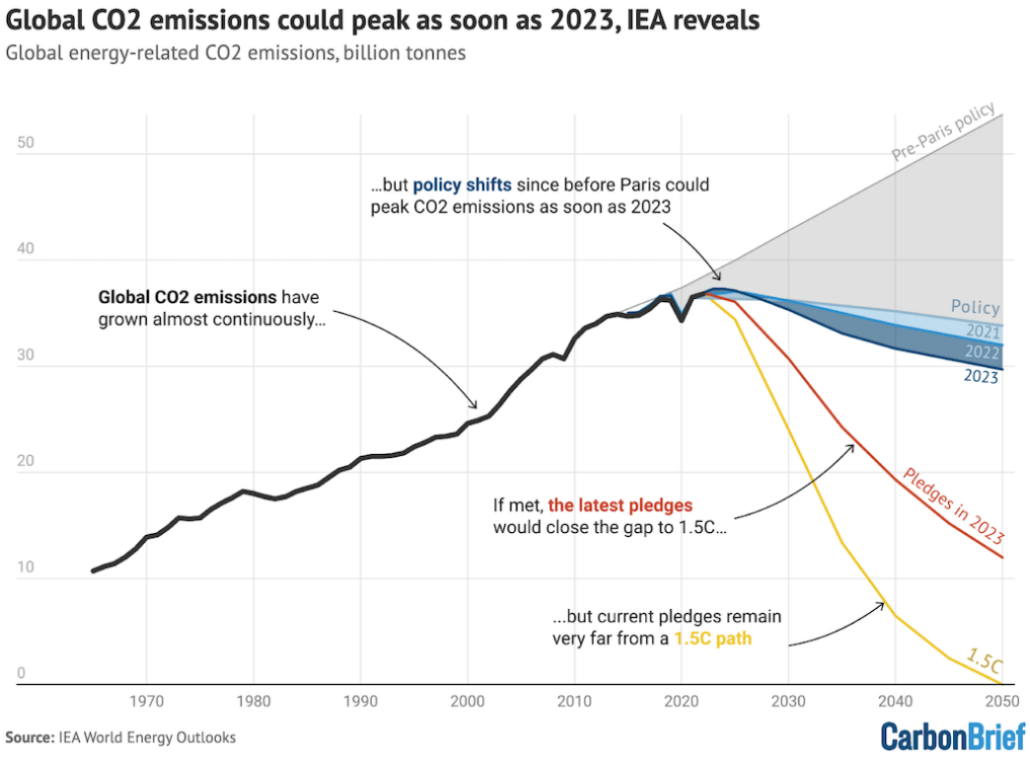

Figure 1.3: IEA World Energy forecasts the world's CO_2 emission will peak in 2023, eventually it will reduce in the coming years after adoption of strategic policy.[7]

The global CO_2 emission situation is dire, with emissions steadily rising despite temporary declines during events like the COVID-19 pandemic. According to the International Energy Agency (IEA), global CO_2 emissions rose less than initially feared in 2022 due to clean energy growth offsetting the impact of increased coal and oil use.[7] Key contributors to these emissions include the continued use of fossil fuels like coal, oil, and gas, alongside industrial processes, and deforestation.[8] Rising temperatures have led to extreme weather events, sea-level rise, and environmental degradation.[9]

To address this crisis, governments worldwide must implement effective policies and agreements. Examples include carbon pricing, regulations on emissions standards, and investments in renewable energy and clean technologies [10,11]. Cap and trade programs, such as the EU Emissions Trading System and California's Cap-and-Trade Program, have shown promise in reducing emissions while maintaining economic growth.[7,12] Positive impacts have been observed with the implementation of these policies, such as reductions in carbon pollution and advancements in clean energy technologies. However, to achieve significant progress, international cooperation and ambitious targets are necessary. The transition to renewable energy, improved energy efficiency, and sustainable transportation are essential steps in curbing emissions.[7]

The projected future without substantial intervention suggests continued increases in CO_2 emissions, leading to further climate change impacts. Urgent action is required at all levels, from individual behavior changes to global policy agreements, to avert this scenario.[9] By adopting comprehensive strategies, including emissions reductions, investment in clean technologies, and adaptation measures, we can mitigate the worst effects of climate change.

The U.S. National Clean Hydrogen Strategy and Roadmap[13] provides a comprehensive framework to accelerate the production, processing, delivery, storage, and use of clean hydrogen to meet ambitious decarbonization goals across multiple sectors of the economy. The roadmap outlines clear targets and strategic milestones for hydrogen production and utilization by 2030, 2040, and 2050, offering a detailed view of the current hydrogen landscape in the U.S. and a pathway for future development.

Key to the strategy's success is collaboration among various stakeholders, including federal agencies, industry, academia, national laboratories, state and local governments, environmental and justice groups, and labor unions. This multi-sectoral engagement is crucial to driving progress. In support of these efforts, the Biden-Harris Administration has launched the Hydrogen Interagency Task Force[14], signaling a strong commitment to advancing the hydrogen sector.

The roadmap sets ambitious goals, including producing 10 million metric tonnes (MMT) of clean hydrogen annually by 2030, 20 MMT by 2040, and 50 MMT by 2050. To help meet these targets[15], $7 billion has been allocated to construct seven hydrogen hubs, which are expected to produce 3 MMT of clean hydrogen per year by 2030. This initiative is part of broader investments in clean energy technologies.[14] The strategy is designed to be adaptable, with provisions for regular updates based on stakeholder feedback and ongoing analysis. Recent government initiatives to promote hydrogen include support for private sector projects and the construction of a green hydrogen plant. These projects reflect the nation's growing commitment to advancing hydrogen technologies and building a sustainable energy future to further support the growth of the U.S. hydrogen industry as part of its "Investing in America" agenda.[16]

Looking at the current global energy demand, driven by population growth and advancements in lifestyle and recent emergence of artificial intelligence, surge in energy consumption and increasing levels of CO_2 and other greenhouse gases in the atmosphere inevitable, leading to a rise in Earth's surface temperature. To combat global warming, it is crucial to adopt renewable energy sources and make lifestyle changes. One potential solution is hydrogen generation through conventional water electrolysis, but this process requires substantial energy input. This challenge has sparked the development of solar-to-hydrogen (STH) conversion, which uses sunlight as the energy source to power electrolyzers that split water into hydrogen (H_2) and oxygen (O_2), offering a more sustainable approach.

There are three main methods for water splitting. The 1) Photochemical approach is the most cost-effective, but it has a solar-to-hydrogen (STH) efficiency of <1% and separating the resulting hydrogen (H_2) and oxygen (O_2) is both challenging and expensive. The other two prominent methods are 2) Photovoltaic (PV) water splitting and 3) Photoelectrochemical (PEC) water splitting.

In PV water splitting, photovoltaic cells convert sunlight directly into electricity, which is then used to power an electrolyzer that splits water (H_2O) into hydrogen and oxygen via electrolysis. This process involves two electrodes submerged in water (electrolyte), with an electrical current that splits the water molecules. PV water splitting is widely used in large-scale hydrogen production and integrated renewable energy systems. While PV systems can achieve efficiencies of over 10%,[17] they are expensive, and further efficiency improvements are limited. However, advancements in PV technology, electrolyzer design,

and catalyst development can help enhance performance and improve the efficiency of hydrogen production.

In PEC (photoelectrochemical) water splitting cells, photoelectrodes absorb sunlight and generate electron-hole pairs, which then drive redox reactions at the electrode-electrolyte interface, splitting water into hydrogen and oxygen at the electrode surface. This direct approach offers potential for higher efficiency compared to PV-based methods and is well-suited for decentralized hydrogen production, such as solar-powered water-splitting devices for on-site use. Also, there is plenty of scope for improvements include developing efficient and stable photoelectrodes capable of absorbing a wide range of sunlight. Enhancing charge separation, surface reactions, and optimizing electrolytes are also crucial for boosting device performance. Focusing on creating durable photoelectrodes, improving light absorption and charge transport, and addressing issues like electrolyte stability, corrosion, and scaling up PEC systems. With its moderate efficiency and affordability, PEC water splitting holds great promise, but further advancements are needed to maximize its potential.

In my PhD research, I have spent all my time studying PEC Water Splitting Reactions to find out how water oxidation occurs at the semiconductor and electrolyte interface.

1.2 Theory of Photoelectrochemical Water Splitting

Photoelectrochemical (PEC) water splitting is a process where solar energy is harnessed and converted into chemical energy, specifically stored in hydrogen bonds. This solar-driven reaction involves two key steps: hydrogen production at the photocathode and oxygen generation at the photoanode. The oxygen evolution reaction (OER), requiring four electrons and holes (*Figure 1.4*), is the most kinetically challenging and often the rate-limiting step in the overall process.[18]

Under standard conditions, this reaction demands an energy input of 237 kJ per mole of hydrogen produced,[19] making it an endergonic (energy-absorbing) process. The field began with Boddy's[20] initial research in 1968, followed by Fujishima and Honda's pivotal work using TiO_2.[21]

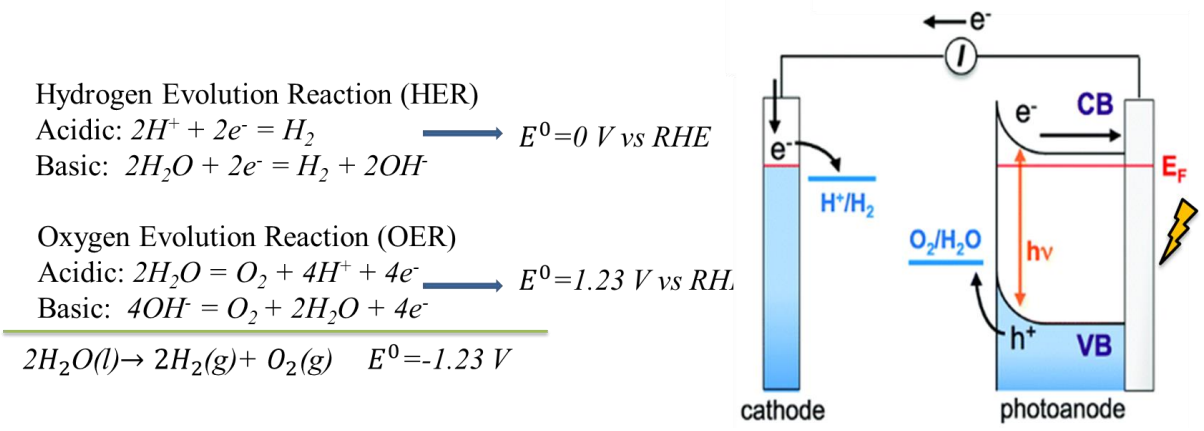

Figure 1.4: Corresponding equation of HER and OER under alkaline and acidic electrolyte. The schematic of Water Splitting reactions at cathode and anode.

Over the past five decades, a variety of semiconductors have been tested as photoanodes, including traditional metal oxides like TiO_2, WO_3, $SrTiO_3$, as well as newer

materials such as $BiVO_4$ and Cu_2O. Narrow bandgap semiconductors like GaAs and cadmium-based materials have also been studied[22–24].

However, each material faces significant challenges. For instance, titanium dioxide's wide 3.2 eV bandgap restricts light absorption to the UV spectrum, limiting efficiency to around 1.5%, which falls short of commercial viability. Tungsten trioxide, with a 2.8 eV bandgap, only achieves about 5% efficiency.[25]

An ideal photoanode must meet several criteria: it should absorb visible light effectively, enable efficient charge separation and movement, facilitate fast charge transfer at interfaces, have energy bands aligned for the desired reactions, and maintain stability in water.[25] While non-oxide semiconductors may show promise, they often degrade under operating conditions. Meanwhile, high-performance materials like III-V semiconductors remain too expensive for widespread use. Despite decades of research, no material has yet been discovered that meets all these requirements.[26,27]

When a semiconductor encounters an electrolyte, the system tries to reach equilibrium by aligning their Fermi levels. In an n-type semiconductor, where electrons are the majority carriers, the Fermi level is located just below the conduction band. At the semiconductor-electrolyte interface, a charge imbalance forms due to the difference in Fermi levels, leading to the creation of a double layer near the surface. This results in the formation of a space charge layer, where the surface of the semiconductor becomes depleted of electrons, causing "band bending" from the surface into the bulk. The extent of this band bending is influenced by the level of doping, or dopant density (N_D), which determines the depletion width (W), i.e., the thickness of the space charge layer. The depletion width can be calculated using the following equation:

$$W = \sqrt{\frac{2\kappa\varepsilon_0(V - V_{fb})}{qN_D}}$$

Where κ is the dielectric constant of the semiconductor, ε_0 is the vacuum permittivity (8.854×10^{-14} C V^{-1} cm^{-1}), q is the electronic charge, V is the applied potential, V_{fb} is the flatband potential (the potential at which no band bending occurs).

Under illumination, the difference between the quasi-Fermi levels of electrons and holes determines the magnitude of the photovoltage generated at the semiconductor-electrolyte junction *(Figure 1.5)*. This photovoltage can be harnessed to drive uphill chemical

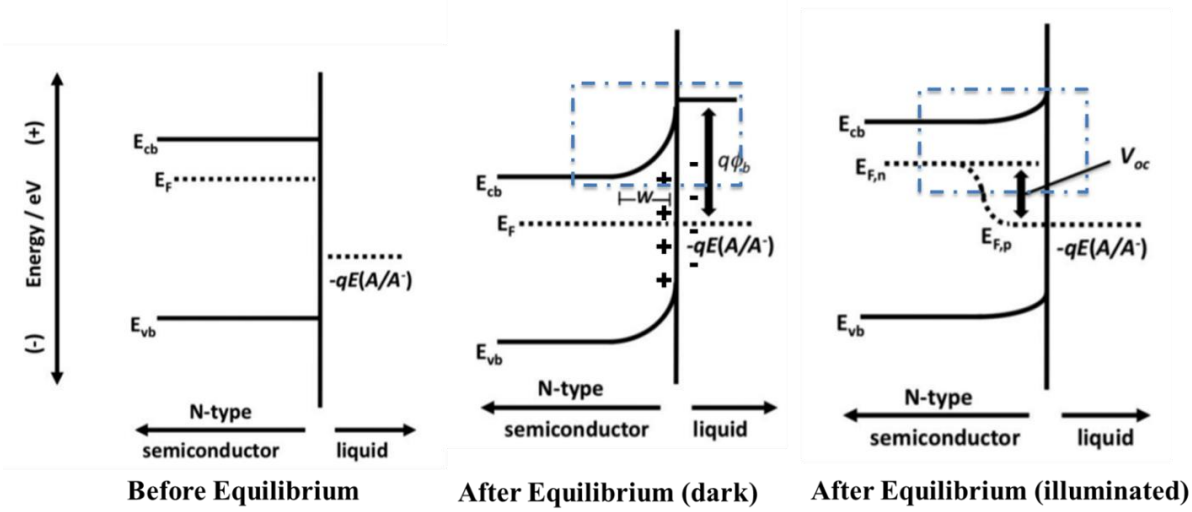

Figure 1.5: Semiconductor electrolyte interface: E_{cb} and E_{vb} are the potentials of the conduction and valence band edge, E_F is the Fermi level, W is the width of the space-charge or depletion layer, V_{oc} is open-circuit potential under illumination, $E_{F,n}$ and $E_{F,p}$ are the electron and hole quasi-Fermi levels under illumination.

reactions, such as splitting water at a potential below its thermodynamic oxidation potential. However, the actual photovoltage is often less than the theoretical maximum due to recombination losses, which affect the positions of the quasi-Fermi levels.[25]

Recombination losses, both in the space charge layer and on the surface, are the main factors limiting photovoltage during water oxidation, as they reduce the splitting between the quasi-Fermi levels. In addition, bulk recombination of photogenerated charge carriers reduces the charge separation efficiency, which lowers the photocurrent output.[28,29]

Assuming the space charge layer behaves like a parallel-plate capacitor, with depletion width as the plate spacing, parameters such as dopant density (N_D) and flatband potential (V_{fb}) can be determined using electrochemical impedance spectroscopy (EIS) and Mott-Schottky plot:

$$\frac{1}{C^2_{SC}} = \frac{2\left(V - V_{fb} - \frac{k_B T}{q}\right)}{qN_D A \kappa \varepsilon_0}$$

where C_{SC} is the space charge capacitance, k_B is the Boltzmann constant, T is the temperature, A is the active surface area of the electrode.

Upon illumination, electrons are excited from the valence band to the conduction band, creating electron-hole pairs and widening the depletion region. Under steady-state illumination, the Fermi level splits into quasi-Fermi levels for electrons and holes due to the difference in their concentrations. The quasi-Fermi levels describe the electrochemical potential of electrons and holes under illumination.

The efficiency of light absorption by the semiconductor, or light harvesting efficiency (η_{LH}), depends on the material's absorption coefficient and thickness. Once charge carriers (electrons and holes) are generated, they move within the space charge layer: electrons migrate to the bulk, and holes move towards the surface. The band bending in the space charge layer provides the energy necessary to drive these movements.

Some charge carriers undergo recombination in the bulk, reducing the efficiency of charge separation (η_{cs}). The charge carriers that successfully reach the surface without recombining accumulate in surface states (SS). Holes that reach SS can either participate in oxygen generation by reacting with the electrolyte or recombine with conduction band

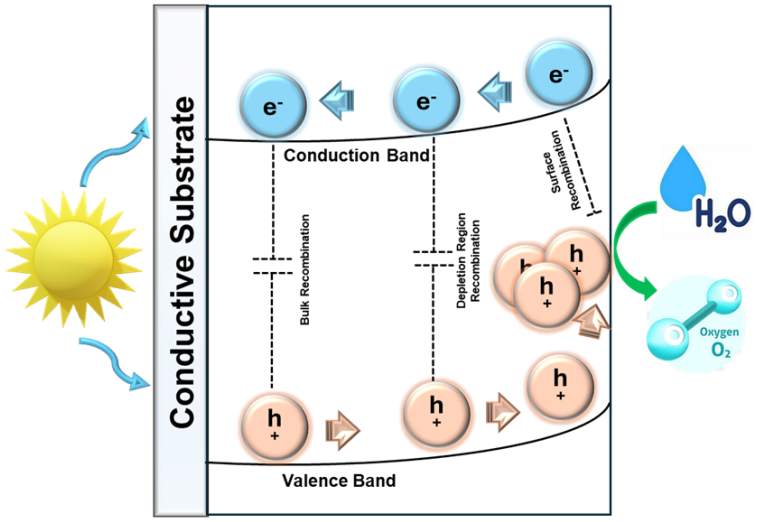

Efficiency of water oxidation= $q\Phi[\eta_{LH}(\lambda) \times \eta_{CS}(V) \times \eta_{HC}(V)]$

Figure 1.6: A general schematic of n-type semiconductor under PEC water oxidation under illumination. Efficiency is controlled by light harvesting, charge separation and hole collection process. The schematic also shows potential pathways of recombination in the bulk, depletion layer and on the surface.

electrons. The efficiency with which holes contribute to water oxidation is called hole collection efficiency (η_{HC}).

When the photoanode is at the flatband potential (V_{fb}), there is no band bending, resulting in no charge separation and no current from water oxidation. Electrons drift towards the cathode under an applied anodic potential, where they reduce water in the hydrogen evolution reaction (HER). Meanwhile, holes in the space charge layer move to the surface to drive the oxygen evolution reaction (OER).

1.3 Hematite

Hematite (α-Fe_2O_3) has emerged as a promising candidate for photoelectrochemical (PEC) water splitting, particularly for the water oxidation half-reaction. This iron oxide polymorph possesses several advantageous properties that make it an attractive material

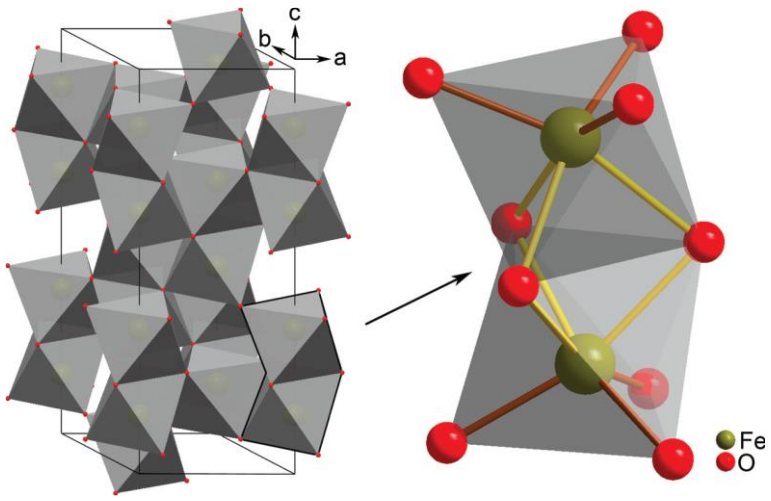

Figure 1.7: The Crystal structure of α-Fe_2O_3. The octahedral structure forming in the [001] direction.[32]

for solar energy conversion. It has attracted the attention of a wide community of researchers in the Solar Oxidation field, a simple Google Scholar search with yield 1000s of work on Hematite.[30] Hematite has a corundum-type crystal structure and an n-type semiconductor, which is the most thermodynamically stable among Fe_2O_3 polymorphs. Its structure consists of pairs of face-sharing octahedra (Fe_2O_9 dimers) aligned along the c-axis ([001] direction). This arrangement results in a hexagonal unit cell with oxygen anions (O^{2-}) arranged along the [001] direction, while iron cations (Fe^{3+}) occupy two-thirds of the octahedral interstices. [31,32]

Hematite's band gap of approximately 2.1 eV allows it to absorb visible light up to ~600 nm, making it suitable for solar energy harvesting. The valence band of hematite consists of strongly hybridized Fe *3d* and O *2p* orbitals,[33,34] as revealed by soft X-ray spectroscopy and density functional theory (DFT) studies. This hybridization contributes to its unique electronic properties. Several factors make hematite an attractive material for PEC water splitting- first hematite is extremely stable under alkaline conditions, ensuring long term viability for large-scale applications. Secondly it is non-toxic and abundant, making it economically viable for widespread use. Thirdly the valence band edge of hematite lies below the O_2/H_2O redox potential, making it suitable for water oxidation.[35]

Hematite has several challenges that limit its efficiency in PEC water splitting:

1. Hematite suffers from low minority charge carrier mobility and short lifetimes, resulting in a very short charge collection length of 2-20 nm.[35]

2. The light absorption depth can be up to 375 nm for 550 nm light, which is significantly longer than the charge collection length.[36]

3. The conduction band edge lies approximately 0.4 V positive of the H_2/H^+ potential, thus an applied bias for proton reduction is necessary.[37]

4. The water oxidation kinetics on hematite surfaces are slow, with low faradaic rate constants compared to other semiconductors like TiO_2 and WO_3.[38]

Researchers have employed various strategies to overcome these limitations. Like creating nanostructured hematite electrodes to maximize light absorption while minimizing the distance minority carriers must travel. [39,40] Introduced dopants to improve electron transport properties. [41] Applying thin overlayers of materials like Al_2O_3 and Ga_2O_3 to reduce electron hole recombination.[42] Also modifying surfaces with catalytic materials to enhance water oxidation kinetics.[43] Recent studies have provided valuable insights into the water oxidation mechanism on hematite. Both hole transfer to the electrolyte and surface electron-hole recombination are thought to occur via surface states and sluggish hole transfer kinetics result in hole accumulation at the surface, potentially causing partial Fermi-level pinning.[43] Similar intermediates have been observed for both electrochemical (dark) and photoelectrochemical (light) water oxidation, suggesting a common mechanism.[44]

1.4 Project Objective

Despite significant advancements in understanding and improving hematite photoanodes, the mechanisms and kinetics of the water oxidation reaction (OER) remain poorly understood, with many gaps still to be addressed. This thesis extensively investigates the underlying mechanism of OER, aiming to provide deeper insights into

this complex process and all the studies were done utilizing Electrochemical Impedance Spectroscopy (EIS) to track photogenerated holes on surface states during OER.

***Chapter 2*:** In this work, hematite thin films were synthesized using the Atomic Layer Deposition (ALD) technique and employed for oxygen evolution reaction (OER) in alkaline electrolyte. The rate law for OER was investigated under varying light intensities to explore the underlying mechanism. Additionally, the behavior of the band structure under high hole concentrations and changes in hole collection efficiency were examined. The kinetic model for the rate law is still under investigation, particularly in understanding the justification for higher-order reactions. Two potential explanations include band uplifting closer to the OER thermodynamic potential and the presence of multiple surface states, suggesting parallel reaction pathways for OER in hematite.

***Chapter 3*:** In this work, the surface of ALD-deposited hematite was modified with Ga_2O_3 overlayers and annealed at varying temperatures. Electrochemical Impedance Spectroscopy (EIS) was used to measure surface state capacitance across all samples, and J-V behavior was examined. The findings suggest a parallel reaction pathway during the oxygen evolution reaction (OER) of hematite, with evidence of peroxo species formation. This study also explores the dynamic interchange between peroxo and oxo surface states, shedding light on the complexity of the OER mechanism.

***Chapter 4*:** In this chapter, I explore the surface states involved in the oxygen evolution reaction (OER) of $CuWO_4$, an area that remains largely unexplored. Based on similar materials, $CuWO_4$ is expected to follow a surface-state-mediated OER pathway. To investigate the chemical nature of these surface states, I employed Photoinduced Absorption Spectroscopy (PIAS) and operando ATR-IR spectroscopy. This ongoing work

aims to optimize experimental conditions by stabilizing the electrolyte and preventing corrosion during operando studies. The findings have the potential to enhance our understanding of $CuWO_4$'s role in OER.

REFERENCES

(1) Department of Economic and Social Affairs. *World Population Prospects* **2024**. United Nations. https://population.un.org/wpp/Graphs/DemographicProfiles/Line/900.

(2) United Nations; Statistics Division; Department of Economic and Social Affairs. Energy Statistic Pocketbook. **2024**.

(3) alliedmarketresearch.com. *Fossil Fuel Energy Market Size, Share, Competitive Landscape and Trend Analysis Report, by Sources, by End-User : Global Opportunity Analysis and Industry Forecast, 2022-2031*; **2023**. https://www.alliedmarketresearch.com/fossil-fuel-energy-market-A31902.

(4) Bailey Schultz. Coal Consumption Set to Reach Record High in 2022 amid Global Energy Crisis. *USA Today*. **December 18, 2022**. https://www.usatoday.com/story/money/energy/2022/12/18/coal-consumption-record-2022-energy-crisis-iea/10921266002/.

(5) Energy Institute; KPMG; Kearney. Oil Consumption Worldwide from 1998 to 2023 (in 1,000 Barrels per Day). *Energy Institute* **2024**.

(6) IEA. *Fossil Fuel Supply*; Paris, **2023**. https://www.iea.org/reports/fossil-fuel-supply.

(7) IEA. *CO2 Emissions in 2023*; Paris, **2024**. https://www.iea.org/reports/co2-emissions-in-2023.

(8) Michiel Nivard; Bram Smeets; Peter van de Giessen; Rune van der Meijden; Christer Tryggestad. *Global Energy Perspective 2023: CO_2 Emissions Outlook*; **2024**. https://www.mckinsey.com/industries/oil-and-gas/our-insights/global-energy-perspective-2023-co2-emissions-outlook.

(9) Calvin, K.; Dasgupta, D.; Krinner, G.; Mukherji, A.; Thorne, P. W.; Trisos, C.; Romero, J.; Aldunce, P.; Barrett, K.; Blanco, G.; Cheung, W. W. L.; Connors, S.; Denton, F.; Diongue-Niang, A.; Dodman, D.; Garschagen, M.; Geden, O.; Hayward, B.; Jones, C.; Jotzo, F.; Krug, T.; Lasco, R.; Lee, Y.-Y.; Masson-Delmotte, V.; Meinshausen, M.; Mintenbeck, K.; Mokssit, A.; Otto, F. E. L.; Pathak, M.; Pirani, A.; Poloczanska, E.; Pörtner, H.-O.; Revi, A.; Roberts, D. C.; Roy, J.; Ruane, A. C.; Skea, J.; Shukla, P. R.; Slade, R.; Slangen, A.; Sokona, Y.; Sörensson, A. A.; Tignor, M.; van Vuuren, D.; Wei, Y.-M.; Winkler, H.; Zhai, P.; Zommers, Z.; Hourcade, J.-C.; Johnson, F. X.; Pachauri, S.; Simpson, N. P.; Singh, C.; Thomas, A.; Totin, E.; Alegría, A.; Armour, K.; Bednar-Friedl, B.; Blok, K.; Cissé, G.; Dentener, F.; Eriksen, S.; Fischer, E.; Garner, G.; Guivarch, C.; Haasnoot, M.; Hansen, G.; Hauser, M.; Hawkins, E.; Hermans, T.; Kopp, R.; Leprince-Ringuet, N.; Lewis, J.; Ley, D.; Ludden, C.; Niamir, L.; Nicholls, Z.; Some, S.; Szopa, S.; Trewin, B.; van der Wijst, K.-I.; Winter, G.; Witting, M.; Birt,

A.; Ha, M. *IPCC,* **2023***: Climate Change 2023: Synthesis Report. Contribution of Working Groups I, II and III to the Sixth Assessment Report of the Intergovernmental Panel on Climate Change [Core Writing Team, H. Lee and J. Romero (Eds.)]. IPCC, Geneva, Switzerland.*; 2023. https://doi.org/10.59327/IPCC/AR6-9789291691647.

(10) Gillingham, K. *The True Cost of Reducing Greenhouse Gas Emissions*; **2019**.

(11) United States; Environmental Protection Agency (EPA). *Laws & Regulations*. Environmental Protection Agency (EPA). https://www.epa.gov/laws-regulations/regulations.

(12) Lisa Song. Cap and Trade Is Supposed to Solve Climate Change, but Oil and Gas Company Emissions Are Up. *ProPublica*. **November 2019**. https://www.propublica.org/article/cap-and-trade-is-supposed-to-solve-climate-change-but-oil-and-gas-company-emissions-are-up.

(13) *U.S. National Clean Hydrogen Strategy and Roadmap*. https://www.hydrogen.energy.gov/library/roadmaps-vision/clean-hydrogen-strategy-roadmap.

(14) US Department of Energy. *Biden-Harris Administration Announces $7 Billion For America's First Clean Hydrogen Hubs, Driving Clean Manufacturing and Delivering New Economic Opportunities Nationwide*.

(15) *HYDROGEN STRATEGY Enabling A Low-Carbon Economy*. https://www.energy.gov/sites/prod/files/2020/07/f76/USDOE_FE_Hydrogen_Strategy_July**2020**.pdf.

(16) US Department of Energy. Biden-Harris Administration Announces $750 Million to Support America's Growing Hydrogen Industry as Part of Investing in America Agenda. March 13, **2024**.

(17) Chu, S.; Li, W.; Yan, Y.; Hamann, T.; Shih, I.; Wang, D.; Mi, Z. Roadmap on Solar Water Splitting: Current Status and Future Prospects. *Nano Futures* **2017**, *1* (2), 022001. https://doi.org/10.1088/2399-1984/aa88a1.

(18) Grätzel, M. Photoelectrochemical Cells. *Nature* **2001**, *414* (6861), 338–344. https://doi.org/10.1038/35104607.

(19) Peter, L. M. Semiconductor Electrochemistry. In *Photoelectrochemical Solar Fuel Production: From Basic Principles to Advanced Devices*; Giménez Sixto and Bisquert, J., Ed.; Springer International Publishing: Cham, 2016; pp 3–40. https://doi.org/10.1007/978-3-319-29641-8_1.

(20) Boddy, P. J. Oxygen Evolution on Semiconducting TiO_2. *J Electrochem Soc* **1968**, *115* (2), 199. https://doi.org/10.1149/1.2411080.

(21) FUJISHIMA, A.; HONDA, K. Electrochemical Photolysis of Water at a Semiconductor Electrode. *Nature* **1972**, *238* (5358), 37–38. https://doi.org/10.1038/238037a0.

(22) Yeh, L. -S. R.; Hackerman, N. Iron Oxide Semiconductor Electrodes in Photoassisted Electrolysis of Water. *J Electrochem Soc* **1977**, *124*, 833–836.

(23) Gerischer, H. Electrochemical Photo and Solar Cells Principles and Some Experiments. *J Electroanal Chem Interfacial Electrochem* **1975**, *58* (1), 263–274. https://doi.org/https://doi.org/10.1016/S0022-0728(75)80359-7.

(24) Grätzel, M. Mesoscopic Solar Cells for Electricity and Hydrogen Production from Sunlight. *Chem Lett* **2005**, *34* (1), 8–13. https://doi.org/10.1246/cl.2005.8.

(25) Walter, M. G.; Warren, E. L.; McKone, J. R.; Boettcher, S. W.; Mi, Q.; Santori, E. A.; Lewis, N. S. Solar Water Splitting Cells. *Chem Rev* **2010**, *110* (11), 6446–6473. https://doi.org/10.1021/cr1002326.

(26) Bolts, J. M.; Wrighton, M. S. Correlation of Photocurrent-Voltage Curves with Flat-Band Potential for Stable Photoelectrodes for the Photoelectrolysis of Water. *J Phys Chem* **1976**, *80* (24), 2641–2645. https://doi.org/10.1021/j100565a004.

(27) Butler, M. A.; Ginley, D. S. Principles of Photoelectrochemical, Solar Energy Conversion. *J Mater Sci* **1980**, *15* (1), 1–19. https://doi.org/10.1007/BF00552421.

(28) Gärtner, W. W. Depletion-Layer Photoeffects in Semiconductors. *Physical Review* **1959**, *116* (1), 84–87. https://doi.org/10.1103/PhysRev.116.84.

(29) Reichman, J. The Current-Voltage Characteristics of Semiconductor-Electrolyte Junction Photovoltaic Cells. *Appl Phys Lett* **1980**, *36* (7), 574–577. https://doi.org/10.1063/1.91551.

(30) Zboril, R.; Mashlan, M.; Petridis, D. Iron(III) Oxides from Thermal ProcessesSynthesis, Structural and Magnetic Properties, Mössbauer Spectroscopy Characterization, and Applications. *Chemistry of Materials* **2002**, *14* (3), 969–982. https://doi.org/10.1021/cm0111074.

(31) Sivula, K.; Zboril, R.; Le Formal, F.; Robert, R.; Weidenkaff, A.; Tucek, J.; Frydrych, J.; Grätzel, M. Photoelectrochemical Water Splitting with Mesoporous Hematite Prepared by a Solution-Based Colloidal Approach. *J Am Chem Soc* **2010**, *132* (21), 7436–7444. https://doi.org/10.1021/ja101564f.

(32) Sivula, K.; Le Formal, F.; Grätzel, M. Solar Water Splitting: Progress Using Hematite (α-Fe_2O_3) Photoelectrodes. *ChemSusChem* **2011**, *4* (4), 432–449. https://doi.org/10.1002/cssc.201000416.

(33) Ma, Y.; Johnson, P. D.; Wassdahl, N.; Guo, J.; Skytt, P.; Nordgren, J.; Kevan, S. D.; Rubensson, J.-E.; Boske, T.; Eberhardt, W. *Electronic Structures of A-Fez03 and $Fe_3 0_4$ from 0 E-Edge Absorption and Emission Spectroscopy*; 1993; Vol. 48.

(34) Bandyopadhyay, A.; Velev, J.; Butler, W. H.; Sarker, S. K.; Bengone, O. Effect of Electron Correlations on the Electronic and Magnetic Structure of Ti-Doped α-Hematite. *Phys Rev B Condens Matter Mater Phys* **2004**, *69* (17). https://doi.org/10.1103/PhysRevB.69.174429.

(35) Dare-Edwards, M. P.; Goodenough, J. B.; Hamnett, A.; Trevellick, P. R. Electrochemistry and Photoelectrochemistry of Iron(III) Oxide. *Journal of the Chemical Society, Faraday Transactions 1: Physical Chemistry in Condensed Phases* **1983**, *79* (9), 2027. https://doi.org/10.1039/f19837902027.

(36) Goodenough, J. B. Metallic Oxides. *Progress in Solid State Chemistry* **1971**, *5*, 145–399. https://doi.org/https://doi.org/10.1016/0079-6786(71)90018-5.

(37) Kennedy, J. H.; Frese, K. W. Flatband Potentials and Donor Densities of Polycrystalline α-Fe_2O_3 Determined from Mott-Schottky Plots. *J Electrochem Soc* **1978**, *125* (5), 723–726. https://doi.org/10.1149/1.2131535.

(38) Upul Wijayantha, K. G.; Saremi-Yarahmadi, S.; Peter, L. M. Kinetics of Oxygen Evolution at α-Fe_2O_3 Photoanodes: A Study by Photoelectrochemical Impedance Spectroscopy. *Physical Chemistry Chemical Physics* **2011**, *13* (12), 5264. https://doi.org/10.1039/c0cp02408b.

(39) Ling, Y.; Wang, G.; Wheeler, D. A.; Zhang, J. Z.; Li, Y. Sn-Doped Hematite Nanostructures for Photoelectrochemical Water Splitting. *Nano Lett* **2011**, *11* (5), 2119–2125. https://doi.org/10.1021/nl200708y.

(40) Rangaraju, R. R.; Panday, A.; Raja, K. S.; Misra, M. Nanostructured Anodic Iron Oxide Film as Photoanode for Water Oxidation. *J Phys D Appl Phys* **2009**, *42* (13), 135303. https://doi.org/10.1088/0022-3727/42/13/135303.

(41) Zandi, O.; Klahr, B. M.; Hamann, T. W. Highly Photoactive Ti-Doped α-Fe_2O_3 Thin Film Electrodes: Resurrection of the Dead Layer. *Energy Environ. Sci.* **2013**, *6* (2), 634–642. https://doi.org/10.1039/C2EE23620F.

(42) Hisatomi, T.; Le Formal, F.; Cornuz, M.; Brillet, J.; Tétreault, N.; Sivula, K.; Grätzel, M. Cathodic Shift in Onset Potential of Solar Oxygen Evolution on Hematite by 13-Group Oxide Overlayers. *Energy Environ. Sci.* **2011**, *4* (7), 2512–2515. https://doi.org/10.1039/C1EE01194D.

(43) Klahr, B.; Gimenez, S.; Fabregat-Santiago, F.; Hamann, T.; Bisquert, J. Water Oxidation at Hematite Photoelectrodes: The Role of Surface States. *J Am Chem Soc* **2012**, *134* (9), 4294–4302. https://doi.org/10.1021/ja210755h.

(44) Klahr, B.; Hamann, T. Water Oxidation on Hematite Photoelectrodes: Insight into the Nature of Surface States through In Situ Spectroelectrochemistry. *The Journal of Physical Chemistry C* **2014**, *118* (19), 10393–10399. https://doi.org/10.1021/jp500543z.

Chapter 2:

Rate Law Analysis of Photoelectrochemical Oxygen Evolution Reaction (OER) on Thin Film Hematite Deposited by Atomic Layer Deposition

2.1 Abstract

Thin film hematite (α-Fe_2O_3) of ~50 nm was deposited on FTO using Atomic Layer Deposition (ALD). The photoelectrochemical (PEC) water oxidation performance was evaluated through cyclic voltammetry under alkaline conditions (pH 13.6), revealing a linear increase in PEC activity with rising light intensity. This enhanced activity is attributed to the increased number of holes generated at the surface state during oxygen evolution reaction (OER). Photoelectrochemical impedance spectroscopy (PEIS) measurements showed that the surface state capacitance (C_{ss}) increased with light intensity but plateaued beyond a certain threshold. C_{ss} was quantified as the hole density at the interface, identifying a rate-limiting step. The accumulation of holes at the interface induced a potential drop in the Helmholtz layer, contributing to Tafel behavior. This demonstrates that the rate of hole transfer to the electrolyte, which impacts OER kinetics, is light dependent. These findings illuminate the origin of the linear PEC activity with light intensity and provide insights into the underlying mechanism.

2.2 Introduction

Global warming has driven the search for renewable, zero-carbon energy sources. Photoelectrochemical (PEC) water splitting holds great promise for commercial applications and has significant potential for improvement. It can also be integrated with Photovoltaic (PV) cells to utilize broad spectrum of light, Fuel cells to produce electricity on demand, CO_2 reduction catalyst to simultaneously generate valuable C-H chemicals, creating a vertically integrated system.[1,2] PEC water splitting reaction involves two key reactions: the hydrogen evolution reaction (HER), a two-electron process, and the oxygen evolution reaction (OER), a more complex four-electron process crucial to both natural and synthetic photosynthesis [3,4]. The OER is the bottleneck in splitting water into hydrogen and oxygen, which is critical for sustainable fuel production. Understanding the mechanism of this multi-electron reaction—whether it occurs stepwise or concertedly, and whether charge carriers accumulate on single or multiple sites—remains a challenge in the field of electrochemistry [5–8]. In photosynthesis, the oxygen evolution reaction (OER) is driven by a Mn_4CaO_x cluster in photosystem II, which stores four oxidizing equivalents to split water into oxygen [9,10]. This process involves multiple light-induced oxidation steps, with proton release helping to prevent charge buildup before the formation of the O-O bond, the slowest step [11,12] Synthetic catalysts for water oxidation have similarly focused on multimetal centers or surfaces [13,14]. Metal oxides, due to their stability under solar-driven conditions, are being investigated, though their exact role in facilitating multielectron reactions or stabilizing intermediates remain uncertain.

Recent studies have uncovered a novel mechanism in photoelectrochemical OER on semiconducting oxides, revealing a multihole process. Using photoinduced absorption

spectroscopy (PIAS), Durrant's group investigated photoanodes like hematite (α-Fe_2O_3) and found that the OER rate solely depends on the accumulation of photogenerated holes at the electrode/electrolyte interface.[15,16] From their PIAS studies, they observed the accumulation of holes at the surface state during OER and how that leads to photocurrent and concluded that the rate of OER follows a power law, transitioning from first order at low light intensity to third-order at higher concentrations, meaning 3 holes are required to accumulate at the surface state during water oxidation. This behavior was also observed in other oxides like TiO_2, $BiVO_4$, and WO_3, suggesting that multihole accumulation is a universal feature of metal oxide photocatalysts.[15] Similarly in photosystem II in plants, where hole accumulation happens first then O-O bond formation. However, studying the active sites and intermediates in heterogeneous OER remains challenging. Progress in spectroscopic techniques has made it possible to detect key intermediates, such as Fe(IV)=O in α-Fe_2O_3 [17,18].Recent work on IrO_2 also shows that water oxidation proceeds via nucleophilic attack on surface oxyl, with the OER rate depending exponentially on surface hole concentration [19].

In this study, we developed a temperature-controlled three-electrode system to investigate the OER mechanism on hematite under very low light intensity to very high light intensity (upto ~6Sun) under alkaline conditions. By varying light intensity, we conducted photoelectrochemical impedance spectroscopy (PEIS) measurements and analyzed the data using equivalent circuit models to decipher surface reactions. The capacitance (C_{ss}) data revealed that holes accumulate prior to OER, but hole density saturates after a certain light intensity, even as the photocurrent continues to increase linearly. This indicates that hole accumulation alone does not drive the OER. Mott-

Schottky analysis with a hole scavenger and cyclic voltammetry (CV) data showed shifts in flatband potential, confirming that band alignment plays a crucial role in enhancing OER rates [20].

2.3 Experimental Section

Hematite thin films were deposited on 1.1 mm thick aluminoborosilicate glass substrate (Solaronix, 10 Ω/sq) with fluorine doped tin oxide (FTO) coated on one side. FTO substrates were cleaned by sonication in soap, water and isopropyl alcohol each for 10 min followed by drying with N_2 stream. Previously described procedure [21,22] was modified to make the hematite films using atomic layer deposition (Savannah 100, Cambridge Nanotech Inc.) technique. 'Wet ozone' has been observed to serve as a better oxidation source compared to only ozone, with improved growth rate and uniformity. The FTO substrate was heated to 200°C, and ferrocene precursor was heated to 70°C. A single cycle consisted of a 20 s ferrocene pulse followed by an oxidation subcycles which included 10 cycles of a 0.015 s H_2O pulse followed by a 2 s ozone pulse, where each subcycle was separated by a 5 s N_2 purge. All films in this experiment were prepared by 1000 ALD cycles and measured to be ~50 nm by absorption measurements (Perkin-Elmer, Lambda 35 with a Labsphere integrating sphere) corrected for FTO substrate.[21] Hematite was first annealed at 500°C, temperature was raised at a rate of 30°C/min, kept at 500°C for 30mins and then cooled to room temperature overnight. Then the electrode was further annealed in a preheated furnace at 800°C for 4 mins followed by quenching at room temperature. The characterization of films was done by Raman Spectroscopy to ensure the generation of hematite. An O-ring was used to attach the photoelectrode to the custom cell, where 0.28 cm^2 hole area was defined as the active area for all

photoelectrochemical measurements, since it's the only area where photoelectrode is in contact with the electrolyte. All the experiments were performed in 1M KOH aqueous solution (pH 13.6, determined with Fisher Scientific Accumet pH meter). Hematite electrodes were clamped to a custom-made glass electrochemical cell. A homemade saturated Ag/AgCl electrode was used as a reference electrode and high surface area platinum mesh was used as the counter electrode. All potentials were converted to the reversible hydrogen electrode (RHE) scale by the equation $V_{RHE} = V_{Ag/AgCl} + 0.197\ V + pH \times (0.059\ V)$. Electrochemical Impedance spectroscopy (EIS) and photoelectrochemical measurements were made with an Eco Chemie Autolab potentiostat coupled with Nova electrochemical software. EIS was done using a 10 mV amplitude perturbation of between 10000 Hz and 0.1 Hz. Data were fitted using Zview software (Scribner Associates). The light source was a 450 W Xe arc lamp (Horiba John). An AM 1.5 solar filter was used to simulate sunlight at 100 mW cm^2 (1 sun), convex lens was placed between the light source and custom cell to focus the light source onto 0.28 cm^2 electrode area to go beyond 1 Sun light intensity. Neutral density filters were used to adjust the intensity ranging from 0.25 Sun to 6.21 Sun. Since the experiments were performed at very high light intensity, the temperature was kept by circulating 25^oC water throughout the course of all experiments otherwise kinetic study might be convoluted due to temperature contribution. All photoelectrochemical measurements were performed by shining light on the hematite electrode through the FTO substrate (back illumination) such that there was no competitive light absorption from the electrolyte. Light and Dark J–V curves were measured at a scan rate of 20 mV s^{-1}.

Hole scavenger study was conducted in presence of both 1 M KOH and 100 mM $K_4[Fe(CN)_6]$.(Sigma Aldrich) Potassium ferrocyanide follows one electron quick redox process, which is very ideal to perform controlled study to validate the hole collection efficiency of our system. Higher concentration of redox couple was chosen to avoid mass transportation limitations

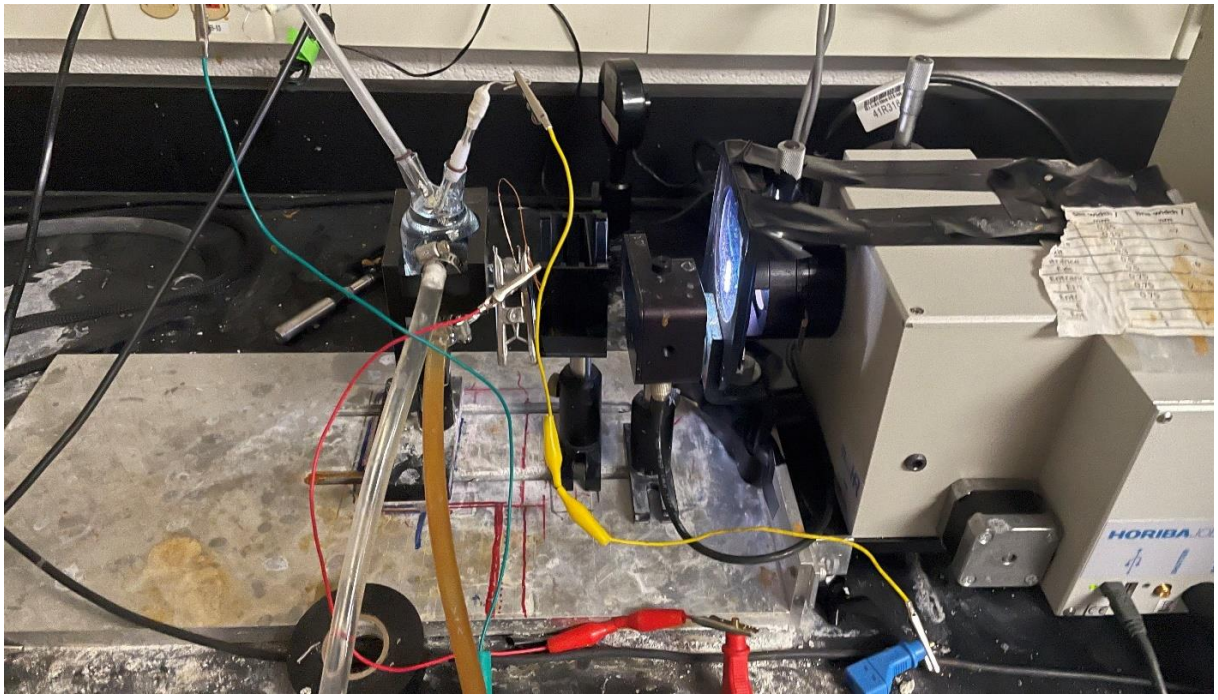

Figure 2.1: Custom made temperature controlled (25°C) three electrode setup; light source is focused using convex lens and series of neutral density filters. This same experimental setup has been used during all our photoelectrochemical studies.

Another experiment was done to study the rapid charging and discharging of surface states under light, which can also further confirm the hole accumulation phenomenon on the surface of the hematite, those are called Transient Experiment. First

chronoamperometry was done at a constant potential in dark, after 30 sec the manual shutter was turned on to illuminate the electrode (back illumination) where after the illumination we get an instantaneous anodic transient spike and let it stabilize for over 10 sec, then the shutter was turned off, where we get the cathodic transient spike. Later we plot the cathodic spike for different biases at different light intensity, integrate the cathodic spike to calculate how much charge has passed through that electrode in those experimental conditions.

Our active working area was 0.28 cm^2, it was adjusted for a roughness factor of 1.5 [23], which make the actual area 0.42 cm^2. All the experimental data and graph plots were adjusted for the actual area. In order to keep consistency of all our experiments and data, all EIS, photoelectrochemical measurements both in water and hole scavenger was performed during one big experiment at one time. The transient experiment and attempt to determine helmoltz capacitance was performed during another experimental attempt, keeping all the parameters of experimental conditions same.

2.4 Results

2.4.1 Thin Film Characterization

During the optimization of photoanodes for this investigation, additional thin films were deposited using Atomic Layer Deposition (ALD) to facilitate thorough characterization. Powder X-ray Diffraction (PXRD) was performed on the 1000-cycle hematite samples; however the data was only dominated by the peaks arriving from FTO substrate due to thinner and planar nature of hematite. However, prior studies under similar experimental conditions with thicker samples (3700 ALD cycles, ~200 nm thickness [21], have been reported from our lab and α-Fe_2O_3 was characterized.[24,25] Raman spectroscopy was employed to analyze the structure of the iron oxide films due to the distinct spectral signatures of common iron oxides, such as hematite (α-Fe_2O_3), maghemite (γ-Fe_2O_3), and magnetite (Fe_3O_4). The Raman spectrum obtained from the 1000 ALD-cycle iron oxide deposited on FTO showed (*Figure 2a*) peaks corresponding to the crystal structure of α-Fe_2O_3. The peak observed at 1300 cm^{-1}, identified as an overtone peak, is expected to be Raman inactive.[26] Both XRD [21] and Raman data confirm that the only observable crystallographic phase in the iron oxide deposited using ferrocene and ozone as precursors is α-Fe_2O_3 (hematite).

Absorbance and reflectance measurements were conducted using a Perkin-Elmer Lambda 35 UV−vis spectrometer equipped with a Labsphere integrating sphere. Building on previous investigations from our lab, we corrected the absorbance spectra to account for reflectance and the absorbance of the FTO substrate (*Figure 2b*). Klahr et al.[21] reported a linear growth in films for up to 500 ALD cycles, with a consistent absorption coefficient and a growth rate of 0.62 Å per cycle; beyond 500 cycles, however, the growth

rate shows slight nonlinearity. Considering our sample is 1000 cycle and following similar recipe for ALD synthesis and obtained highest absorption peak at 410 nm, our sample corresponds to a thickness of ~50 nm. To determine bandgap, absorbance data was utilized to plot $\alpha h\nu^{1/\gamma}$ vs $h\nu$ was plotted which is called Tauc plot and γ =2 considering indirect bandgap for hematite[21] and the value of 2.2 eV was obtained as shown in *Figure 2c*.

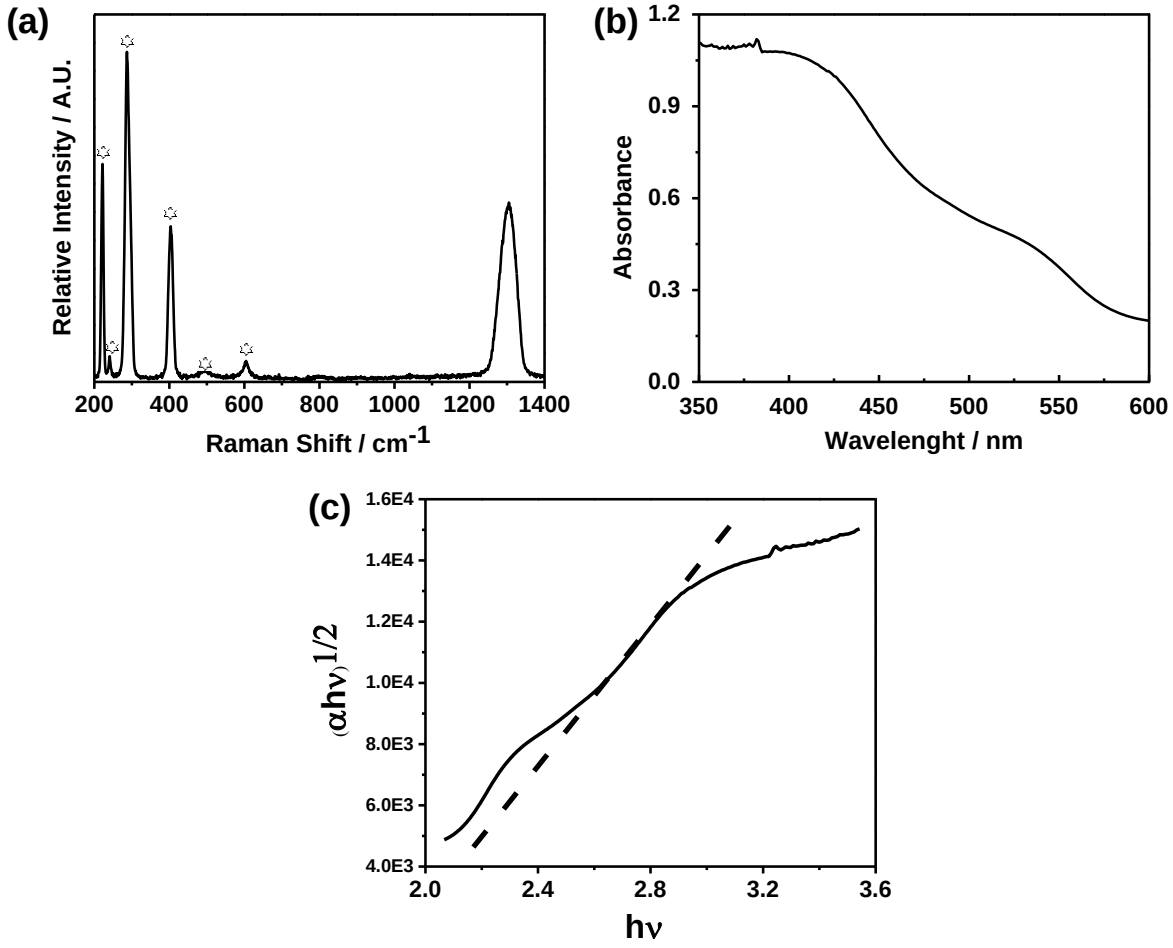

Figure 2.2: a) Raman spectroscopy plot b) Absorbance of our thin film hematite, corrected for FTO substrate, reflectance and derived from transmittance data. c) Tauc plot for band-gap calculation of 1000 ALD cycle Hematite.

2.4.2 Photoelectrochemical Measurements

The overall trend observed in the current-voltage (*J-V*) responses is pretty much consistent with PEC OER meaning there is no observed photocurrent in dark *J-V* and with increasing light intensity the photocurrent is also increasing, as illustrated in *Figure 3a*. Electrochemical impedance spectroscopy (EIS) was conducted on hematite following the same parameters as the *J-V* measurements under same variable light intensities. Nyquist plots were generated using EIS studies where in presence of surface states participating in OER and where photogenerated holes can be stored, two peaks are expected to form near the onset potential[22]. The small semi-circle gets dissolved in higher potential or in dark. Similarly for our system we observed similar features like two capacitive components emerged near the onset potential in the nyquist plots, all our observations are consistent with prior findings, indicating towards a charge accumulation step before the OER. [22,23] To analyze different capacitance (charge storage and bulk) and resistance (charge transfer, trap state and solution) processes in the bulk semiconductor and at the interface, Nyquist plots can be deconvoluted by fitting them with an appropriate equivalent circuit in *Figure 3b* [22] This approach provides valuable insights into the accumulation of charge carriers at the surface under PEC conditions. In this study, a modified Randle's circuit *(Figure 3c)* was used when two semicircles were observed, while a standard Randle's circuit *(Figure 3d)* was applied when only one semicircle was

present. The equivalent circuit encompasses various components: a space-charge capacitance (C_{bulk}) representing the bulk hematite, a surface state capacitance (C_{ss}), and resistances including a series resistance (R_S), a resistance reflecting hole trapping in surface states (R_{trap}), and a charge transfer resistance from surface states to the solution (R_{ct}). In regions where higher bias voltage prevails, characterized by the presence of a single semicircle in the Nyquist plots, a simplified Randles circuit was utilized to analyze impedance spectra. Under different light conditions, C_{ss} exhibits a Gaussian peak around

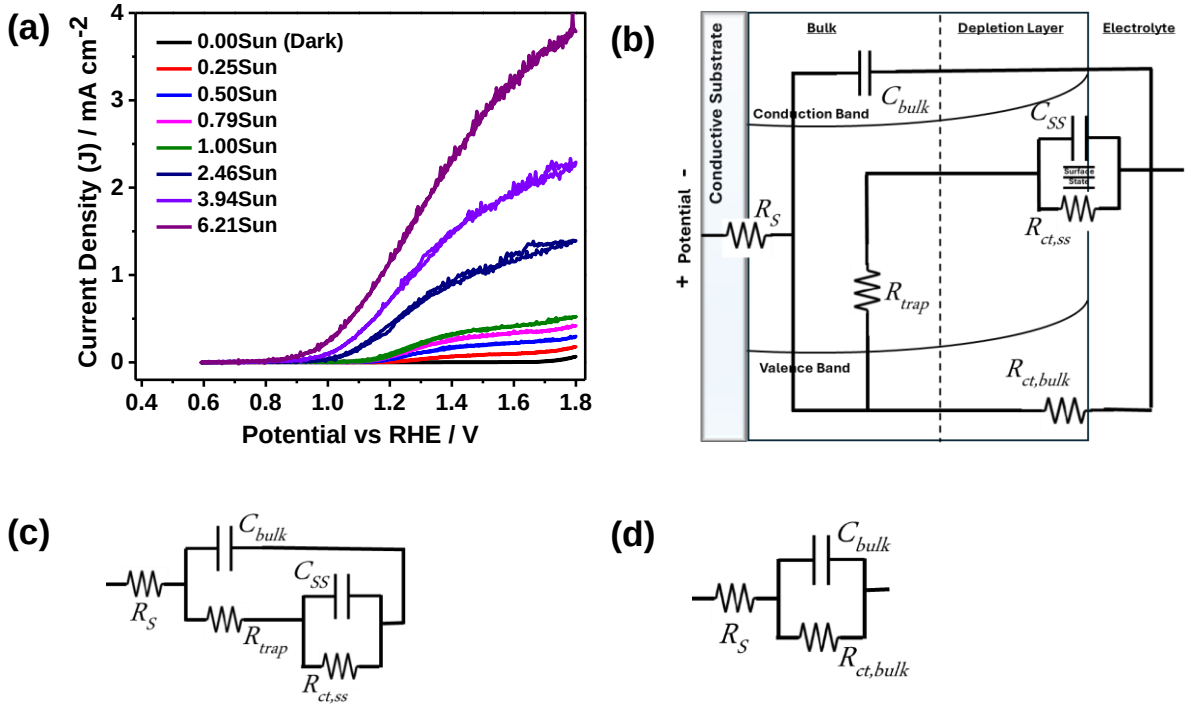

Figure 2.3: a) Photoelectrochemical OER (*J-V*) performance under 1M KOH, pH 13.6; Light intensity started from dark and slowly increased upto 6.21 Sun. b) Various charge transfer and storage phenomenon happening at different regions of a semiconductor during OER, depicted as equivalent circuits. c) and d) are consecutively modified Randal's circuit and Simple Randal's circuit.

the onset of photocurrent, attributed to the accumulation of surface holes.[22] Beyond 1.3 V_{RHE} in potential for water oxidation, the impedance spectra lose the low-frequency semicircle, forming a single semicircle, making it challenging to isolate C_{ss} in the Nyquist plots due to notable fitting errors. In such instances, the simple Randle's circuit is employed for fitting these impedance spectra. Consequently, the raw C_{ss} plots (potentially up to 1.5 V_{RHE}) from *Figure 4a* were further analyzed by fitting with a Gaussian function for extrapolation across the entire dataset. This facilitates further investigation into hole storage, as depicted in *Figure 4b*.

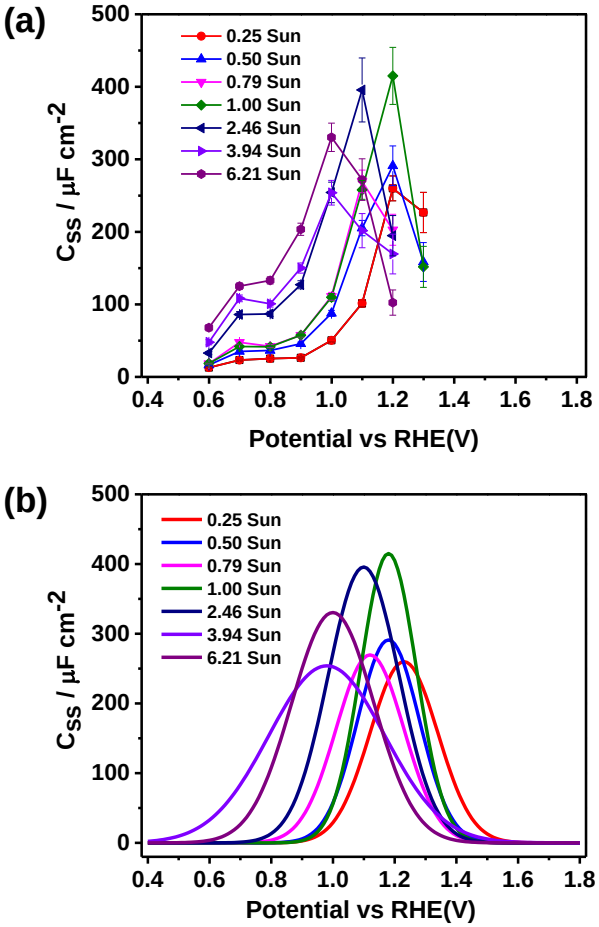

Figure 2.4: a) Raw *Css* obtained from fitting Nyquist plots with appropriate equivalent circuits. b) Fitted *Css* curves were obtained by fitting raw *Css* peaks using Gauss function.

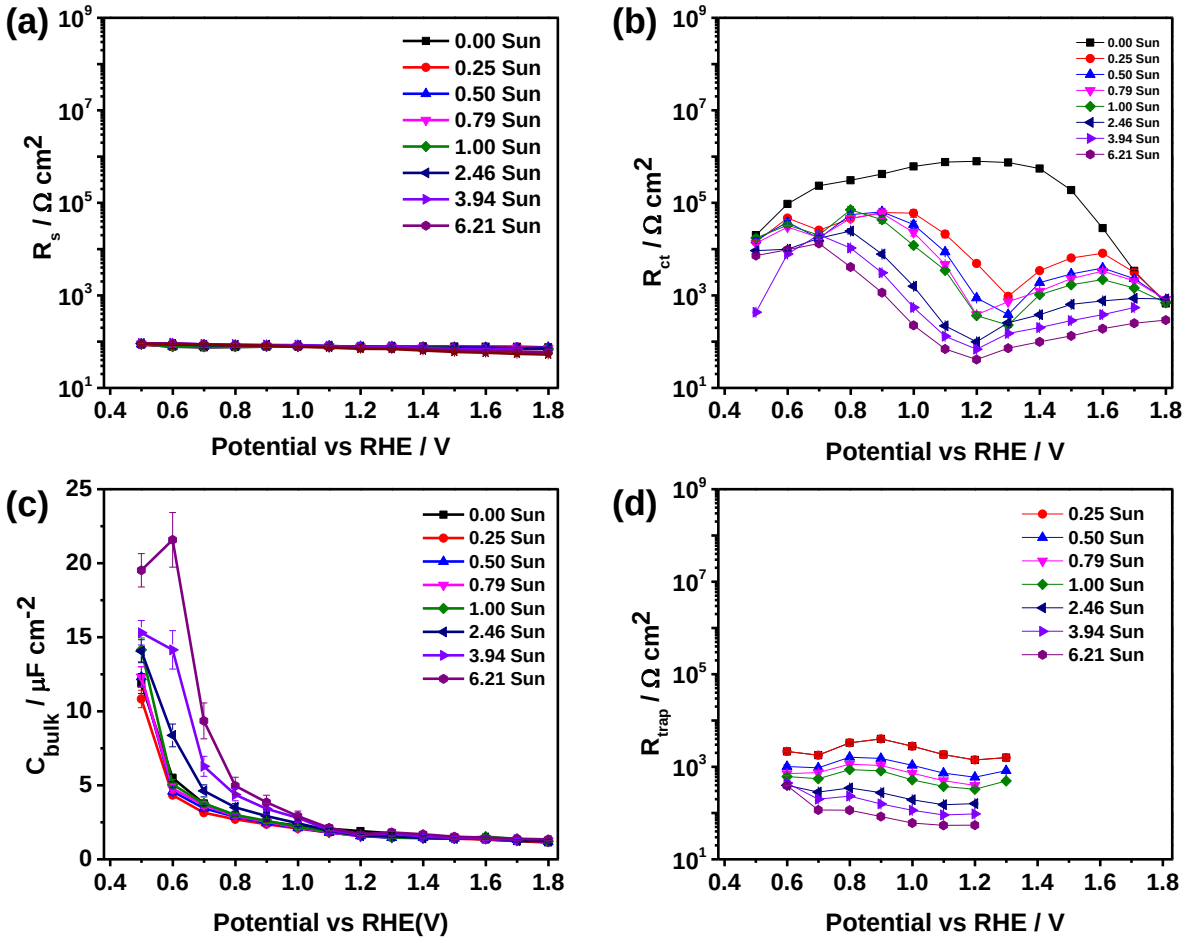

Figure 2.5: All the EIS parameters are plotted here. a) Series resistance *(R_s)*, b) Charge transfer resistance *(R_{ct})*, c) Bulk capacitance *(C_{bulk})*, d) Trap resistance *(R_{trap})* under different light intensity under OER condition.

All the EIS parameters, including resistance and capacitance from the equivalent circuits, are plotted here, with particular attention to C_{bulk} and R_{ct}. These parameters reveal a crucial insight: R_{ct} exhibits a dip around the thermodynamic potential for water oxidation, aligning with the peak behavior of C_{ss}. Both parameters shift cathodically with increasing light intensity, indicating that as hole accumulation occurs at a specific light intensity, water oxidation becomes easier at higher intensities. This shift towards more negative potential

with increasing light intensity is a phenomenon documented previously.[22] The peak of C_{ss} corresponds with a decrease in R_{ct} (*Figure 5b*), suggesting that interfacial charge transfer during water oxidation is linked to the charging of these surface states.

Examining the C_{ss} plot in *Figure 4b*, it is evident that there is an accumulation of holes near the onset potential, though saturation may occur beyond a certain light intensity. To

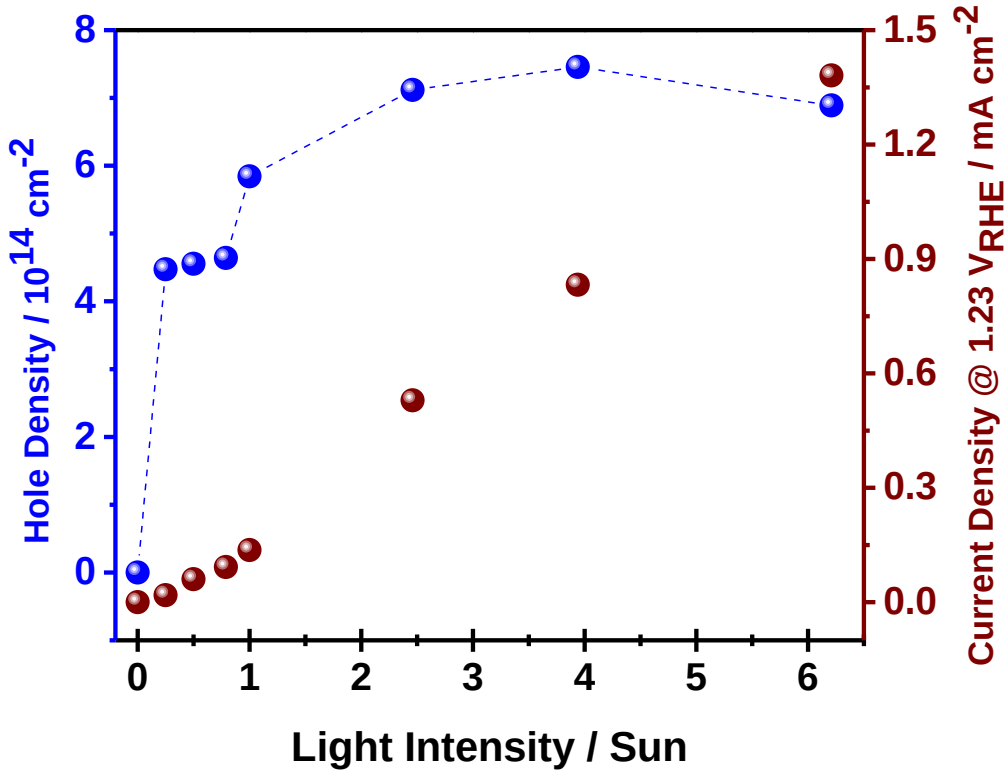

Figure 2.6: Hole density and current density from *Figure 2.3.a* at 1.23 V_{RHE} plotted against light intensity. The hole density is saturating at higher light intensity followed by rapid increase at the initial stage.

quantify this hole accumulation preceding water oxidation, we can analyze C_{ss} plots and calculate the number of holes stored on the surface. Utilizing the formula Q = CV, where Q represents charge and C is the capacitance, we integrate C_{ss} over the entire voltage

range from 0.4 V_{RHE} to 1.8 V_{RHE} to obtain the total stored charge. Since the charge of a hole is the opposite of that of an electron, which is (+) 1.602 x 10^{-19} coulombs, dividing the total stored charge by the charge of a hole enables us to determine the number of holes or hole density stored at the hematite surface under a specific light intensity.

$$\frac{1}{{C_{bulk}}^2} = \frac{2}{\varepsilon\varepsilon_0 A^2 e N_D}\left(V - V_{fb} - \frac{k_B T}{q}\right) \quad \ldots\ldots(1)$$

Our measurements of hole density under various light intensities *(Figure 6)* align in similar ranges of previous findings. For instance, Klahr et al. reported a hole density of 2.9 × 10^{14} cm^{-2} under 1 sun illumination [17], Piccinin et al. [27]observed 1.05 holes/nm^2, Durrant et al.[15] reported range of 0.1-4.0 holes/nm^2, and Hupp et al.[28] found a range of 0.05-0.3 holes/nm^2.

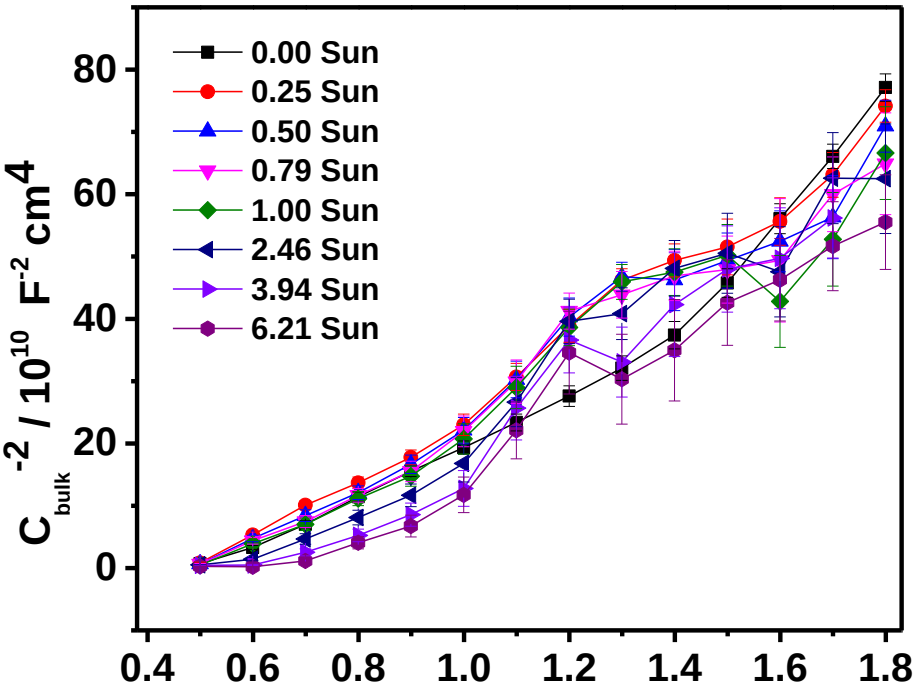

Figure 2.7: Mott-Schottky plots were made using C_{bulk} value and using Eqn 1 under different light intensity.

We applied Mott–Shottky (M–S) analysis using Eqn 1 to our impedance data, focusing on C_{bulk} values, using a dielectric constant of 32 [29] for hematite and the roughness factor adjusted actual surface area (0.42 cm^2) of the electrodes shown in *Figure 7*. Where we can clearly observe the change of slope and intercept in the potential range between 1.0 V_{RHE} to 1.4 V_{RHE}. Which arises from the fact that OER is changing the flatband potential i.e. the band edges of the semicondcutor or dopant density. Further investigation is needed to confirm this hypothesis.

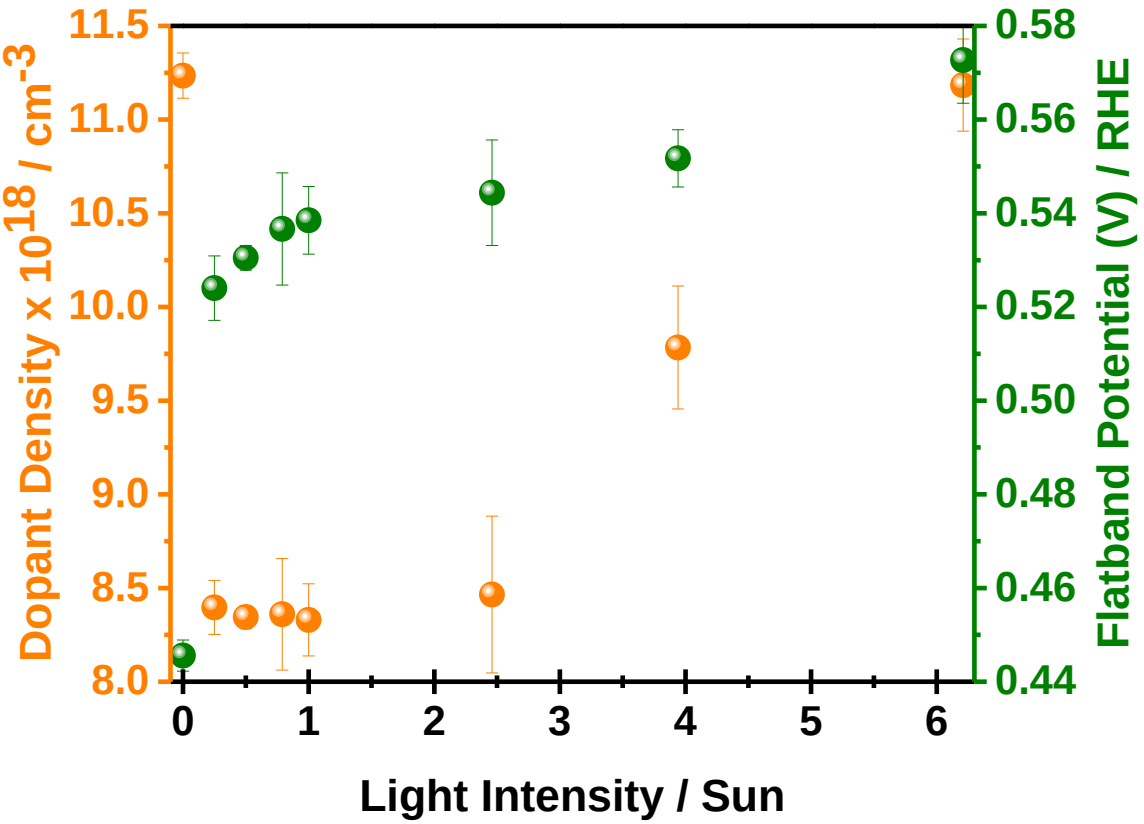

Figure 2.8: Dopant density (N_D) and flatband potential (V_{fb}) were calculated from M-S analysis using Eqn 1 and plotted against incident light intensity during OER.

The flat band potential (V_{fb}) and dopant density (N_D) for various light intensities are depicted in *Figure 2.8*. N_D, around 10^{18} cm^{-3}, ideally should remain relatively stable across conditions. And we observed a consistent rise in flat band potential with increasing light intensity, which is counter intuitive since our onset potential as well as peak of C_{ss} and dip in R_{ct} is moving cathodically. M-S analysis is always not an effective method to explain the band structure movement and dopant density, ideally the dopant density is expected to remain unchanged due to its intrinsic nature.[20,30]

For metal oxide semiconductors, changes in applied potential influence the capacitance across the space charge and Helmholtz layers. The slope of the Mott-Schottky (M−S) plot, determined by the M−S equation, depends on dopant density, assuming a constant dielectric constant [31]. However, when there is a possibility of increasing hole accumulation at the surface it attracts negatively charged species from the solvent to create a double layer across the interface or helmoltz layer, leading to a significant potential drop and it has huge implications in kinetics. the Helmholtz capacitance causes a constant shift in

$$W = \sqrt{\frac{2\kappa\varepsilon_0 V_{bi}}{qN_D}} \qquad \ldots\ldots(2)$$

the x-axis intercept, which must be accounted for when calculating the flat band potential [32]. Erratic dopant density significantly influences the depletion width, W, calculated using Equation 2 at 1.23 V_{RHE} based on dopant densities from M−S plots *(Figure 2.9)*.

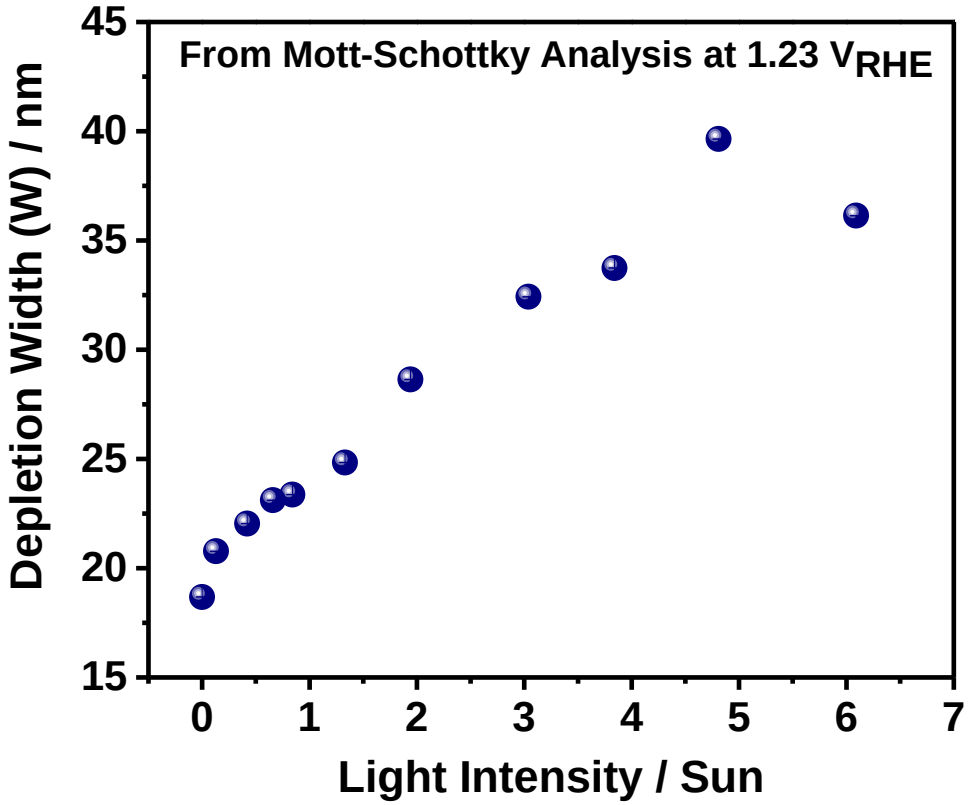

Figure 2.9: Depletion layer width calculated using Eqn 2 and obtained dopant density from M-S analysis under different light intensity.

The Helmholtz capacitance effect causes a consistent shift in the x-axis intercept, which must be accounted for when calculating the flat band potential from M−S plots. This shift in flat-band potential (V_{fb}) is associated with the charging of surface states, expressed as $\Delta V_{charging} = Q_{tot} / C_H$, where Q_{tot} is the integrated value of C_{bulk} over voltage: $Q_{tot} = \int C_{bulk}\, dV$. This calculation results in a Helmholtz capacitance value of C_H = 2.2x10^{-4} F cm^{-2}, aligning with earlier studies [22]. Nevertheless, relying on this value to determine Helmholtz capacitance is not advisable, as explaining such a high value poses difficulties. And with any analytical technique it is almost impossible to estimate the exact C_H parameter.

We explored alternative methods to minimize the V_{fb} and N_D ranges by assuming reasonable C_H values for hematite thin films under alkaline OER conditions. By correcting

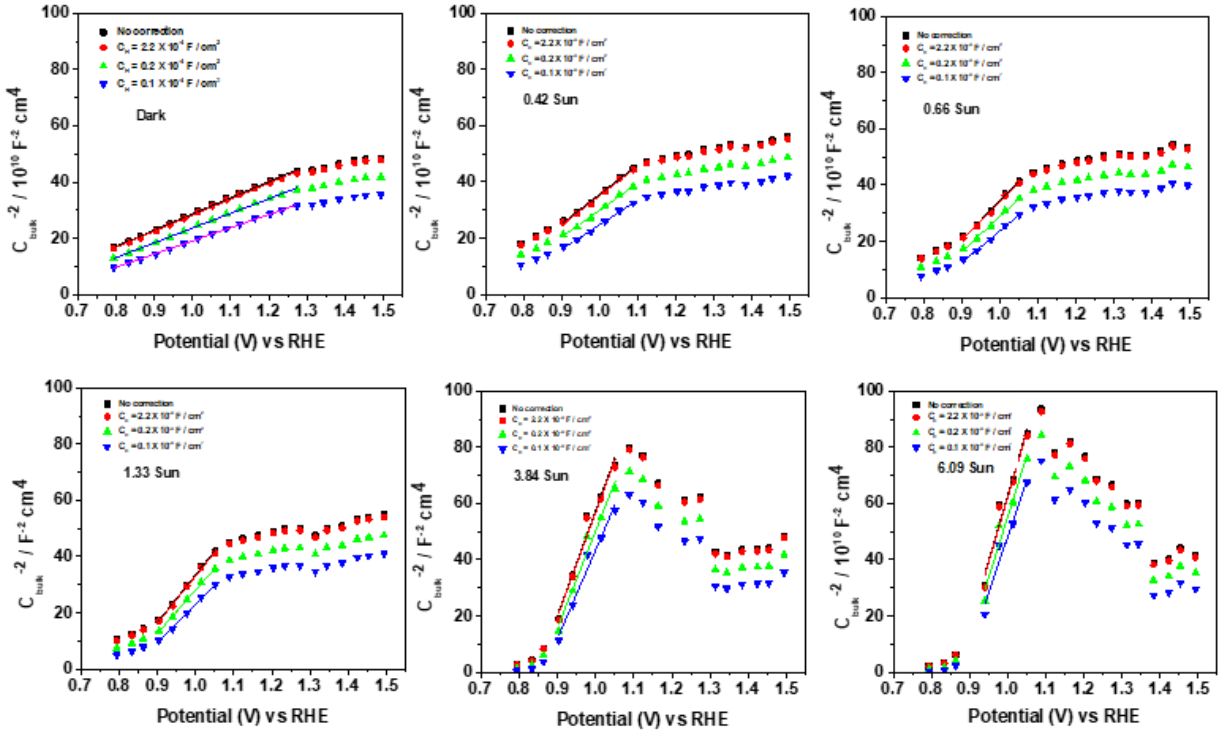

Figure 2.10: Mott-Schottky analysis and fitting in order to analytically calculate helmoltz capacitance (C_H); Three different C_H values were plotted to correct C_{bulk} data. After C_H correction V_{fb} and N_D values were calculated again to observe any significant changes.

C_{bulk} accordingly, we performed M-S analysis to determine the V_{fb} and N_D values. We also adjusted V_{fb} and N_D using more typical Helmholtz capacitance values for hematite under alkaline working condition, specifically 0.1 and 0.2 x 10^{-4} F cm^{-2}.[30] This correction involved adjusting the C_{bulk} for these C_H values, as well as the 2.2 x 10^{-4} F cm^{-2} we previously calculated. These adjustments were tested under various light conditions, including dark, 0.42, 0.66, 1.33, 3.84, and 6.09 Sun shown in *Figure 2.10*.

The correction for helmoltz capacitance using this above method doesn't explain the trends in V_{fb} and N_D we observe in our system. The assumption of C_H might have shortened the range (*Figure 2.11*) still the implications are not clear, and there might be another analytical method where we can determine the dopant density and flatband potential with even more confidence.

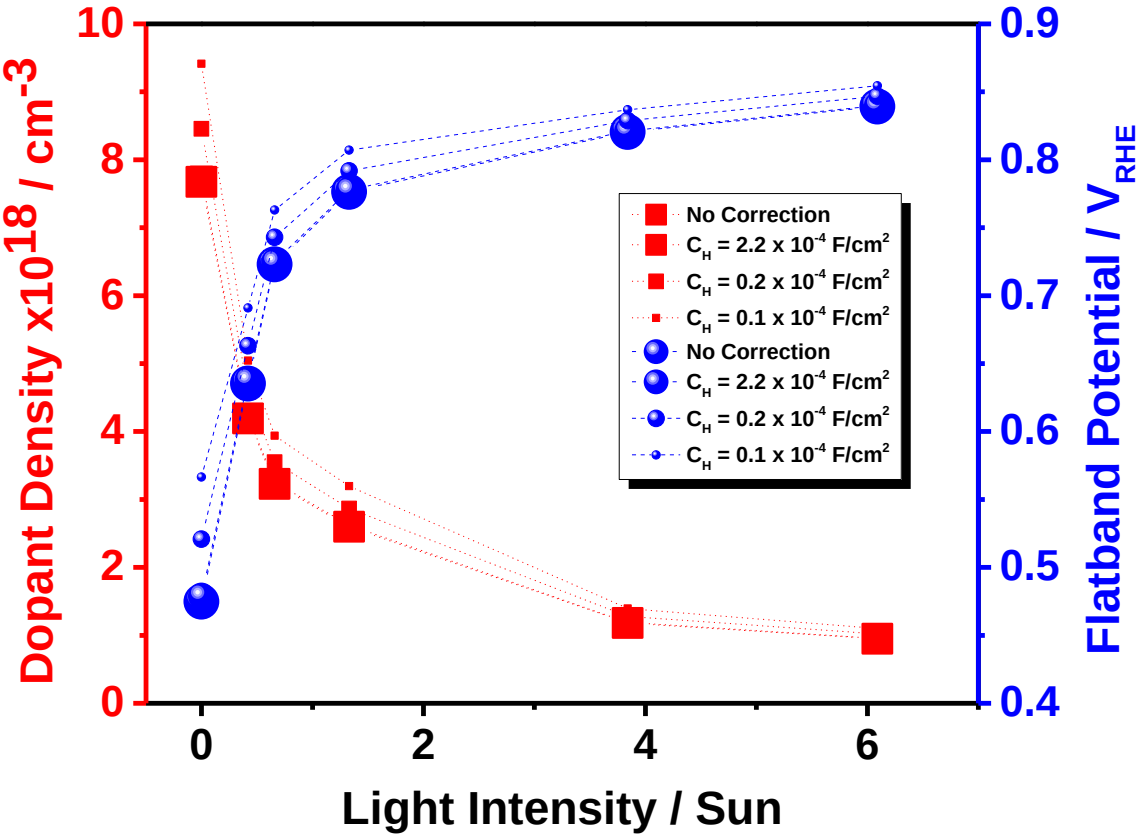

Figure 2.11: Differences in N_D and V_{fb} after correction of C_{bulk} values against three different C_H values, this analysis turned out not so useful to explain the band movement of hematite at different light intensity during OER.

The flat band potential derived from M−S intercepts is often unreliable under high light intensity due to massive amount hole generation, which causes significant helmoltz

capacitance (C_H) and it convolute the C_{bulk}, makes it very difficult to analyze C_{bulk} data to investigate the band edge movements during OER. Instead, the photocurrent onset potential in the presence of a hole scavenger can provide a better estimate. A combined approach of EIS followed by M-S analysis in the presence of a hole scavenger could effectively determine the dopant density across different light intensities. This method has previously demonstrated good agreement with flat band potentials derived from M−S plots for nondegenerate doped hematite electrodes [23,33]. Using a 100 mM $K_4[Fe(CN)_6]$ hole scavenger (high concentration was optimized to prevent mass transport limitations) as the electrolyte, cyclic voltammetry and EIS were performed under the same conditions.

The M-S plot slopes remained constant (*Figure 12b*), yielding a dopant density of 9.54 (±0.24) x 10^{18} cm^{-3}. From the CV data, the flat band potential was identified at varying light intensities (*Figure 12a*).

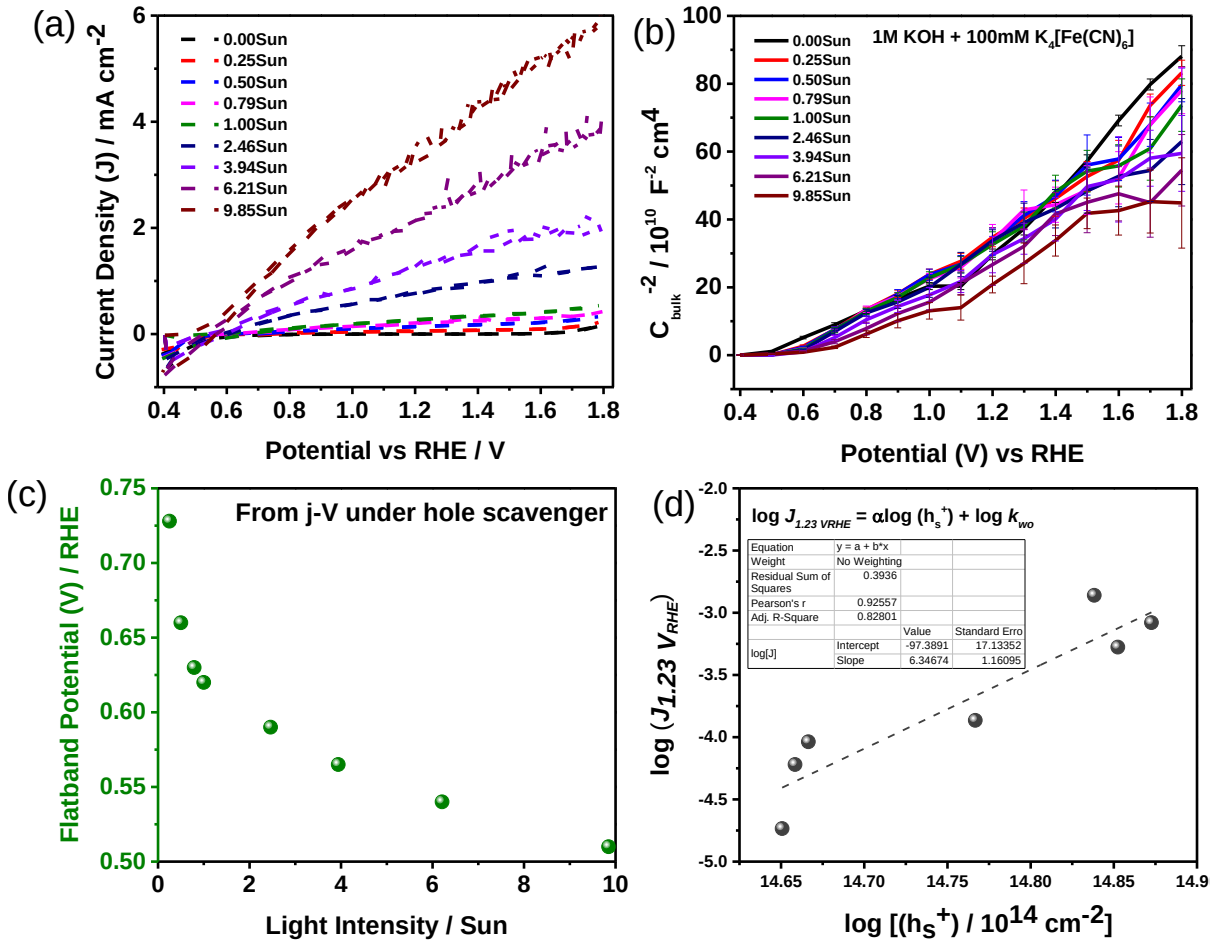

Figure 2.12: a) *J-V* measurement done under increasing light intensity conditions in presence of hole scavenger. b) M-S analysis in presence of hole scavenger shows unchanged slope with respect to increasing light intensity, hinting towards unchanged N_D according to Eqn 1. c) The onset potential of *Figure 2.12.a* provides the value of V_{fb}, and its moving cathodically with increasing light intensity. d) Our hole density and Current Density at 1.23 V_{RHE} obtained during OER in presence of 1 M KOH (no hole scavenger) was plotted against Durrant Model.

From *Figure 2.12.c* the negative (Cathodic) shift of the flatband potential in hematite during OER under increasing light intensity signifies significant changes in its band structure. This cathodic shift indicates that less external potential is required to achieve zero band bending, suggesting a reduction in the depletion width and band bending near the semiconductor-electrolyte interface.[34] As more photogenerated charge carriers are injected into the space-charge region, they partially neutralize the surface charge, leading to a "flattening" effect on the band structure.[35] This results in the conduction and valence bands effectively moving closer to the thermodynamic potential of OER i.e. 1.23 V_{RHE}, improving the OER efficiency.[36] The decreased band bending also leads to a narrower space-charge region and a lower internal electric field. While the intrinsic band edges remain relatively fixed, their apparent position at the interface shifts, aligning more favorably with the electrolyte's potential.[37] This photoinduced modification of charge dynamics enhances interfacial reaction rates due to increased carrier availability and reduces the overpotential required for OER[38] as we have witnessed in our *Figure 2.3.a* and *Figure 2.4.b*. Consequently, hematite becomes more effective at facilitating OER under higher illumination, with its band alignment improving relative to the electrolyte's requirements for the reaction. This phenomenon underscores the complex interplay between light intensity, charge carrier dynamics, and electrochemical processes at the semiconductor-electrolyte interface during photoelectrochemical water splitting.

When the OER data *(Figure 2.6)* was analyzed using the Durrant model [15], the observed rate order deviated from the reported values (*Figure 2.12.d*). Several factors are likely to contribute to this discrepancy. First, their PIAS measurements were conducted at 1.5 V_{RHE}, a condition that minimizes recombination. Second, significant methodological

differences exist between PIAS and EIS techniques. Third, their higher-performing sample was fabricated using PCVD, whereas ours was produced via ALD. More critically, the model's assumptions—light-independent band edges and k_{wo} —limit its applicability, as it is based on a mononuclear reaction pathway governed by surface-state hole density (Fe^{IV}=O).

The Tafel equation is a vital tool for studying reaction kinetics. By considering the potential drop across the Helmholtz layer as directly related to hole density and modifying the Tafel equation accordingly, [20,39] our experimental data reveal that the water oxidation rate constant k_{wo} strongly depends on light intensity *(Figure 2.13.a)*, increasing linearly. This behavior contradicts the assumptions of the Durrant model Model,[15] further supporting the notion that a high hole density at surface states induces a significant potential drop in the Helmholtz layer, substantially influencing the reaction kinetics.

In summary, the higher photocurrent observed under intense illumination arises primarily from a decrease in band bending and an increase in k_{wo}. Despite reduced band bending, the increase in k_{wo} dominates the kinetics, accelerating the hole transfer from the semiconductor to the electrolyte and reducing charge transfer resistance R_{ct}. This observation suggests enhanced hole transport efficiency at high light intensities. However, an additional hypothesis proposes the existence of a parallel pathway where k_{wo} is even faster, albeit with a short lifetime. This scenario aligns with *Figure 2.6*, where hole density at surface states saturates, but rapid k_{wo} driven transfer results in a linear increase in photocurrent. This hypothesis warrants further investigation and experimental validation.

Ongoing efforts focus on developing a refined rate law that incorporates k_{wo} and activation energy into the model to better explain the OER mechanism for hematite.

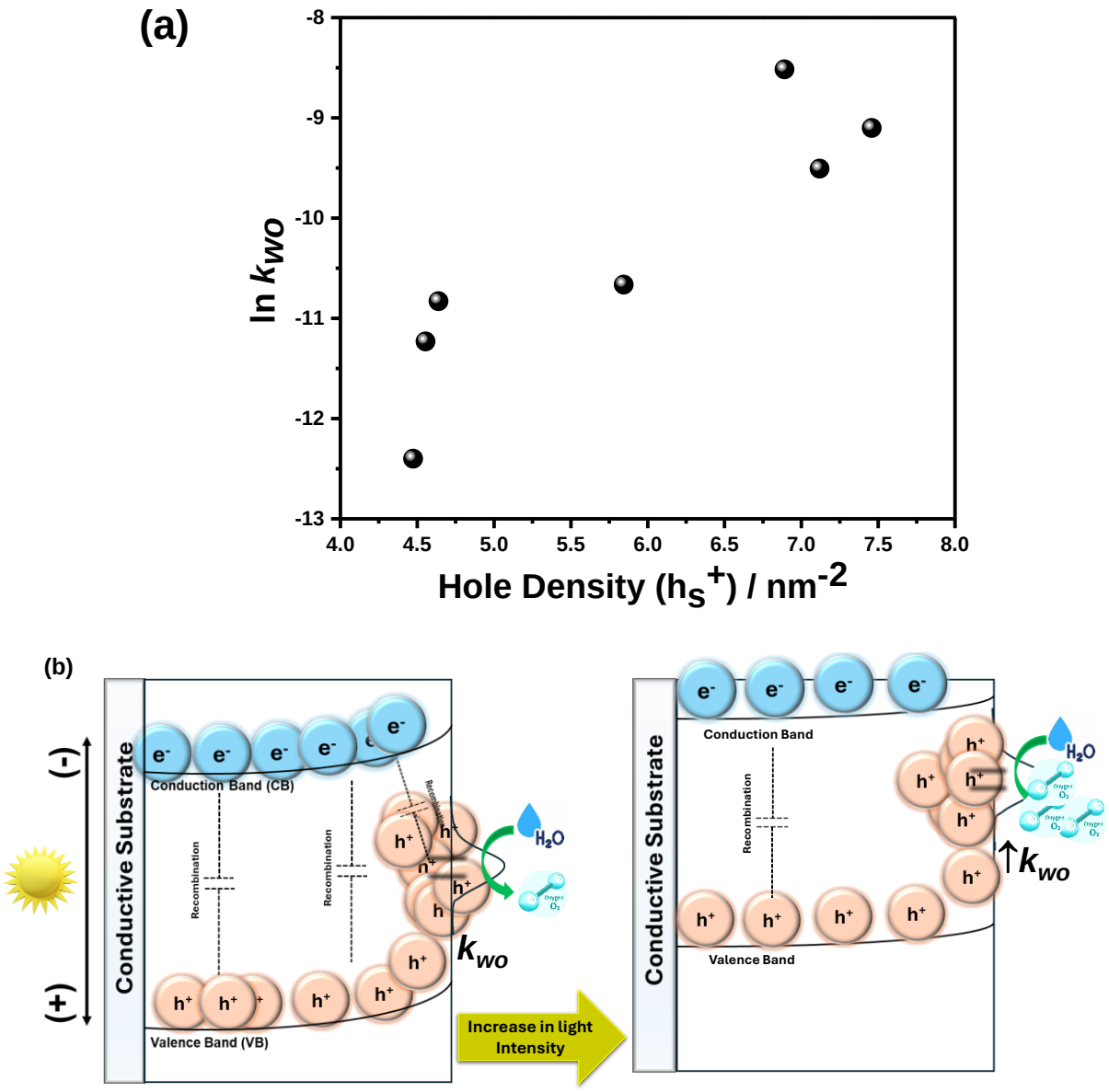

Figure 2.13: a) Tafel analysis using our data shows the change of k_{wo} with respect to light intensity. b) First hypothesis; Rate of water oxidation dependent on hole density, band upliftment and change of water oxidation rate constant.

2.5. Conclusion

This study provides key insights into the oxygen evolution reaction (OER) mechanism of hematite. Notably, increased light intensity causes a cathodic shift in the flatband potential, moving band edges closer to the OER thermodynamic potential. This shift reduces the external bias needed for OER, enhancing efficiency by achieving favorable band alignment under illumination. Photoelectrochemical impedance spectroscopy (EIS) revealed that the surface state capacitance (C_{ss}), rises with light intensity before reaching a saturation. This plateau identifies a rate-limiting step, as sufficient charge carrier accumulation at the interface is critical to driving the multihole OER process effectively. Furthermore, increasing light intensity strengthens the internal electric field and reduces band bending, which narrows the depletion width and lowers recombination, allowing more charge carriers to participate in the reaction. The C_{ss} data are inversely related to charge transfer resistance (R_{ct}), with higher illumination reducing R_{ct} and promoting faster hole transfer to the electrolyte, thereby improving OER kinetics. Tafel analysis further supports these findings, showing that OER kinetics are strongly dependent on light, as evidenced by an increase in the water oxidation rate constant k_{wo} with light intensity. This dependence suggests that higher illumination helps overcome rate limitations by facilitating hole transfer processes. The study's combination of EIS and Mott-Schottky analyses confirms the interconnected roles of flatband potential shifts, surface state capacitance, and charge transfer resistance in the OER mechanism on hematite thus underscores the importance of band alignment, charge separation, and intermediate's role in enhancing OER rates, offering valuable strategies for optimizing hematite for efficient solar water splitting.

REFERENCES

(1) Liu, B.; Wang, S.; Zhang, G.; Gong, Z.; Wu, B.; Wang, T.; Gong, J. Tandem Cells for Unbiased Photoelectrochemical Water Splitting. *Chem Soc Rev* **2023**, *52* (14), 4644–4671. https://doi.org/10.1039/D3CS00145H.

(2) Fan, R.; Cheng, S.; Huang, G.; Wang, Y.; Zhang, Y.; Vanka, S.; Botton, G. A.; Mi, Z.; Shen, M. Unassisted Solar Water Splitting with 9.8% Efficiency and over 100 h Stability Based on Si Solar Cells and Photoelectrodes Catalyzed by Bifunctional Ni–Mo/Ni. *J Mater Chem A Mater* **2019**, *7* (5), 2200–2209. https://doi.org/10.1039/C8TA10165E.

(3) Dau, H.; Limberg, C.; Reier, T.; Risch, M.; Roggan, S.; Strasser, P. The Mechanism of Water Oxidation: From Electrolysis via Homogeneous to Biological Catalysis. *ChemCatChem* **2010**, *2* (7), 724–761. https://doi.org/https://doi.org/10.1002/cctc.201000126.

(4) Rao, R. R.; Stephens, I. E. L.; Durrant, J. R. Understanding What Controls the Rate of Electrochemical Oxygen Evolution. *Joule* **2021**, *5* (1), 16–18. https://doi.org/10.1016/J.JOULE.2020.12.017.

(5) Vinyard, D. J.; Ananyev, G. M.; Charles Dismukes, G. Photosystem II: The Reaction Center of Oxygenic Photosynthesis*. *Annu Rev Biochem* **2013**, *82* (Volume 82, 2013), 577–606. https://doi.org/https://doi.org/10.1146/annurev-biochem-070511-100425.

(6) Cox, N.; Retegan, M.; Neese, F.; Pantazis, D. A.; Boussac, A.; Lubitz, W. Electronic Structure of the Oxygen-Evolving Complex in Photosystem II Prior to O-O Bond Formation. *Science (1979)* **2014**, *345* (6198), 804–808. https://doi.org/10.1126/science.1254910.

(7) Walter, M. G.; Warren, E. L.; McKone, J. R.; Boettcher, S. W.; Mi, Q.; Santori, E. A.; Lewis, N. S. Solar Water Splitting Cells. *Chem Rev* **2010**, *110* (11), 6446–6473. https://doi.org/10.1021/cr1002326.

(8) Lewis, N. S.; Nocera, D. G. Powering the Planet: Chemical Challenges in Solar Energy Utilization. *Proceedings of the National Academy of Sciences* **2006**, *103* (43), 15729–15735. https://doi.org/10.1073/pnas.0603395103.

(9) Cox, N.; Pantazis, D. A.; Lubitz, W. Current Understanding of the Mechanism of Water Oxidation in Photosystem II and Its Relation to XFEL Data. *Annu Rev Biochem* **2020**, *89* (Volume 89, 2020), 795–820. https://doi.org/https://doi.org/10.1146/annurev-biochem-011520-104801.

(10) Pantazis, D. A. Missing Pieces in the Puzzle of Biological Water Oxidation. *ACS Catal* **2018**, *8* (10), 9477–9507. https://doi.org/10.1021/acscatal.8b01928.

(11) Siegbahn, P. E. M. Nucleophilic Water Attack Is Not a Possible Mechanism for O–O Bond Formation in Photosystem II. *Proceedings of the National Academy of Sciences* **2017**, *114* (19), 4966–4968. https://doi.org/10.1073/pnas.1617843114.

(12) Suga, M.; Akita, F.; Yamashita, K.; Nakajima, Y.; Ueno, G.; Li, H.; Yamane, T.; Hirata, K.; Umena, Y.; Yonekura, S.; Yu, L.-J.; Murakami, H.; Nomura, T.; Kimura, T.; Kubo, M.; Baba, S.; Kumasaka, T.; Tono, K.; Yabashi, M.; Isobe, H.; Yamaguchi, K.; Yamamoto, M.; Ago, H.; Shen, J.-R. An Oxyl/Oxo Mechanism for Oxygen-Oxygen Coupling in PSII Revealed by an x-Ray Free-Electron Laser. *Science (1979)* **2019**, *366* (6463), 334–338. https://doi.org/10.1126/science.aax6998.

(13) Sala, X.; Romero, I.; Rodríguez, M.; Escriche, L.; Llobet, A. Molecular Catalysts That Oxidize Water to Dioxygen. *Angewandte Chemie International Edition* **2009**, *48* (16), 2842–2852. https://doi.org/https://doi.org/10.1002/anie.200802659.

(14) Wiechen, M.; Najafpour, M. M.; Allakhverdiev, S. I.; Spiccia, L. Water Oxidation Catalysis by Manganese Oxides: Learning from Evolution. *Energy Environ. Sci.* **2014**, *7* (7), 2203–2212. https://doi.org/10.1039/C4EE00681J.

(15) Le Formal, F.; Pastor, E.; Tilley, S. D.; Mesa, C. A.; Pendlebury, S. R.; Grätzel, M.; Durrant, J. R. Rate Law Analysis of Water Oxidation on a Hematite Surface. *J Am Chem Soc* **2015**, *137* (20), 6629–6637. https://doi.org/10.1021/jacs.5b02576.

(16) Mesa, C. A.; Francàs, L.; Yang, K. R.; Garrido-Barros, P.; Pastor, E.; Ma, Y.; Kafizas, A.; Rosser, T. E.; Mayer, M. T.; Reisner, E.; Grätzel, M.; Batista, V. S.; Durrant, J. R. Multihole Water Oxidation Catalysis on Haematite Photoanodes Revealed by Operando Spectroelectrochemistry and DFT. *Nat Chem* **2020**, *12* (1), 82–89. https://doi.org/10.1038/s41557-019-0347-1.

(17) Klahr, B.; Hamann, T. Water Oxidation on Hematite Photoelectrodes: Insight into the Nature of Surface States through In Situ Spectroelectrochemistry. *The Journal of Physical Chemistry C* **2014**, *118* (19), 10393–10399. https://doi.org/10.1021/jp500543z.

(18) Zandi, O.; Hamann, T. W. Determination of Photoelectrochemical Water Oxidation Intermediates on Haematite Electrode Surfaces Using Operando Infrared Spectroscopy. *Nat Chem* **2016**, *8* (8), 778–783. https://doi.org/10.1038/nchem.2557.

(19) Nong, H. N.; Falling, L. J.; Bergmann, A.; Klingenhof, M.; Tran, H. P.; Spöri, C.; Mom, R.; Timoshenko, J.; Zichittella, G.; Knop-Gericke, A.; Piccinin, S.; Pérez-Ramírez, J.; Cuenya, B. R.; Schlögl, R.; Strasser, P.; Teschner, D.; Jones, T. E. Key Role of Chemistry versus Bias in Electrocatalytic Oxygen Evolution. *Nature* **2020**, *587* (7834), 408–413. https://doi.org/10.1038/s41586-020-2908-2.

(20) Bevan, K. H.; Peter, L. M. Do Potential Dependent Kinetics Play a Role in Photocatalytic Rate Trends? *Environ. Sci.: Nano* **2024**, *11* (2), 645–656. https://doi.org/10.1039/D3EN00436H.

(21) Klahr, B. M.; Martinson, A. B. F.; Hamann, T. W. Photoelectrochemical Investigation of Ultrathin Film Iron Oxide Solar Cells Prepared by Atomic Layer Deposition. *Langmuir* **2011**, *27* (1), 461–468. https://doi.org/10.1021/la103541n.

(22) Klahr, B.; Gimenez, S.; Fabregat-Santiago, F.; Hamann, T.; Bisquert, J. Water Oxidation at Hematite Photoelectrodes: The Role of Surface States. *J Am Chem Soc* **2012**, *134* (9), 4294–4302. https://doi.org/10.1021/ja210755h.

(23) Klahr, B.; Gimenez, S.; Fabregat-Santiago, F.; Bisquert, J.; Hamann, T. W. Electrochemical and Photoelectrochemical Investigation of Water Oxidation with Hematite Electrodes. *Energy Environ. Sci.* **2012**, *5* (6), 7626–7636. https://doi.org/10.1039/C2EE21414H.

(24) Souza, F. L.; Lopes, K. P.; Longo, E.; Leite, E. R. The Influence of the Film Thickness of Nanostructured α-Fe_2O_3 on Water Photooxidation. *Phys. Chem. Chem. Phys.* **2009**, *11* (8), 1215–1219. https://doi.org/10.1039/B811946E.

(25) Wang, Q.; Moser, J.-E.; Grätzel, M. Electrochemical Impedance Spectroscopic Analysis of Dye-Sensitized Solar Cells. *J Phys Chem B* **2005**, *109* (31), 14945–14953. https://doi.org/10.1021/jp052768h.

(26) León, C. P.; Kador, L.; Zhang, M.; Müller, A. H. E. In Situ Laser-Induced Formation of α-Fe_2O_3 from Fe^{3+} Ions in a Cylindrical Core-Shell Polymer Brush. *Journal of Raman Spectroscopy* **2004**, *35* (2), 165–169. https://doi.org/https://doi.org/10.1002/jrs.1125.

(27) Righi, G.; Plescher, J.; Schmidt, F.-P.; Campen, R. K.; Fabris, S.; Knop-Gericke, A.; Schlögl, R.; Jones, T. E.; Teschner, D.; Piccinin, S. On the Origin of Multihole Oxygen Evolution in Haematite Photoanodes. *Nat Catal* **2022**, *5* (10), 888–899. https://doi.org/10.1038/s41929-022-00845-9.

(28) Kim, D. W.; Riha, S. C.; DeMarco, E. J.; Martinson, A. B. F.; Farha, O. K.; Hupp, J. T. Greenlighting Photoelectrochemical Oxidation of Water by Iron Oxide. *ACS Nano* **2014**, *8* (12), 12199–12207. https://doi.org/10.1021/nn503869n.

(29) Glasscock, J. A.; Barnes, P. R. F.; Plumb, I. C.; Bendavid, A.; Martin, P. J. Structural, Optical and Electrical Properties of Undoped Polycrystalline Hematite Thin Films Produced Using Filtered Arc Deposition. *Thin Solid Films* **2008**, *516* (8), 1716–1724. https://doi.org/https://doi.org/10.1016/j.tsf.2007.05.020.

(30) Hankin, A.; Bedoya-Lora, F. E.; Alexander, J. C.; Regoutz, A.; Kelsall, G. H. Flat Band Potential Determination: Avoiding the Pitfalls. *J. Mater. Chem. A* **2019**, *7* (45), 26162–26176. https://doi.org/10.1039/C9TA09569A.

(31) Gomes, W. ~P.; Cardon, F. Electron Energy Levels in Semiconductor Electrochemistry. *Prog Surf Sci* **1982**, *12* (2), 155–215. https://doi.org/10.1016/0079-6816(82)90002-8.

(32) Van Den Meerakker, J. E. A. M.; Meulenkamp, E. A.; Scholten, M. (Photo)Electrochemical Characterization of Tin-Doped Indium Oxide. *J Appl Phys* **1993**, *74* (5), 3282–3288. https://doi.org/10.1063/1.354549.

(33) Zandi, O.; Hamann, T. W. Enhanced Water Splitting Efficiency Through Selective Surface State Removal. *J Phys Chem Lett* **2014**, *5* (9), 1522–1526. https://doi.org/10.1021/jz500535a.

(34) Iandolo, B.; Zhang, H.; Wickman, B.; Zorić, I.; Conibeer, G.; Hellman, A. Correlating Flat Band and Onset Potentials for Solar Water Splitting on Model Hematite Photoanodes. *RSC Adv* **2015**, *5* (75), 61021–61030. https://doi.org/10.1039/C5RA10215D.

(35) Xi, L.; Lange, K. M. Surface Modification of Hematite Photoanodes for Improvement of Photoelectrochemical Performance. *Catalysts* **2018**, *8* (11), 497. https://doi.org/10.3390/catal8110497.

(36) Gao, R.-T.; Zhang, J.; Nakajima, T.; He, J.; Liu, X.; Zhang, X.; Wang, L.; Wu, L. Single-Atomic-Site Platinum Steers Photogenerated Charge Carrier Lifetime of Hematite Nanoflakes for Photoelectrochemical Water Splitting. *Nat Commun* **2023**, *14* (1), 2640. https://doi.org/10.1038/s41467-023-38343-6.

(37) Patel, M. Y.; Mortelliti, M. J.; Dempsey, J. L. A Compendium and Meta-Analysis of Flatband Potentials for TiO_2, ZnO, and SnO_2 Semiconductors in Aqueous Media. *Chemical Physics Reviews* **2022**, *3* (1). https://doi.org/10.1063/5.0063170.

(38) Yu, Y.; Click, K. A.; Chien, S.-C.; Sun, J.; Curtze, A.; Lin, L.-C.; Wu, Y. Decoupling PH Dependence of Flat Band Potential in Aqueous Dye-Sensitized Electrodes. *The Journal of Physical Chemistry C* **2019**, *123* (14), 8681–8687. https://doi.org/10.1021/acs.jpcc.9b00710.

(39) Zhang, S.; Leng, W. Questioning the Rate Law in the Analysis of Water Oxidation Catalysis on Haematite Photoanodes. *Nat Chem* **2020**, *12* (12), 1097–1098. https://doi.org/10.1038/s41557-020-00569-y.

Chapter 3:

Surface State Passivation of Hematite by Gallium Overlayer: Insight into Water Oxidation Reaction by Electrochemical Impedance Spectroscopy

3.1 Abstract

Hematite holds promise as a catalyst for photoelectrochemical water oxidation, though its overall efficiency remains low. Enhancing this efficiency requires a better understanding of the underlying photocatalytic mechanisms, which are difficult to fully capture through experimental methods alone. In this study, we investigated water oxidation on bare hematite and analyzed the influence of a Gallium Oxide overlayer using electrochemical impedance, photoelectrochemical methods, and Raman spectroscopy. Our findings reveal notable shifts in surface state capacitance and trap resistance, pointing to surface state passivation rather than improved catalysis. The reaction mechanism seems largely unaffected by specific surface terminations and involves peroxo intermediates from lattice oxygen. It's also likely that various surface terminations coexist and shift during the reaction. Additionally, midgap states in hematite significantly impact water oxidation by trapping holes and facilitating recombination.

3.2 Introduction

From the previous chapter, it is evident that water oxidation proceeds via long-lived surface states[1], commonly referred to as holes, whose chemical nature has been explored in the transition from Fe-OH to Fe=O.[2,3] Consistently in our study reported in previous chapter alongside with Le Format et. al.[4], the saturation of hole density has been observed, despite increasing photocurrent, leading to two hypotheses. The first, which we validated in the previous chapter, suggests an increase in the water oxidation rate constant (k_{wo}). The second hypothesis claims the existence of another surface state, difficult to detect through optical measurements. Recent work by Rothschild et al. observed double-peak cathodic discharge waves, indicating the presence of two metastable intermediates with distinct redox potentials. These peaks, revealed after long time delays, suggest parallel reaction pathways rather than the traditionally accepted sequential four proton-coupled electron transfer (PCET) or hydroxide-coupled hole transfer steps. This challenges the idea that intermediates follow the same reaction pathway in sequence.[5] Further investigation into these mechanisms reveals two possible routes: the bi-functional mechanism, where H^+ transfers to an adjacent acceptor during O-O bond formation, and the bi-nuclear mechanism, where two adjacent *=O moieties couple. The latter provides a promising way to overcome the high thermodynamic overpotential in the mono-nuclear mechanism by breaking universal scaling relationships between adsorbates.[6,7] Patzke et al. noted a transition in iron-oxo kinetics from first order to third-order at higher hole densities, suggesting that the accumulation of iron-oxo species lowers activation energy and leads to a third-order reaction pathway. This implies the generation of iron-peroxo species following O-O bond formation.[8] A prior study by

Hamann et al.[3] demonstrated that applying an alumina overlayer on hematite reduces surface state capacitance, meaning that hole accumulation decreases with Al_2O_3 surface modification. However, this also leads to a reduction in photocurrent. Despite its benefits, alumina is known to be highly unstable under harsh water oxidation conditions. Gallium oxide (Ga_2O_3), another material with a corundum structure, presents a potential alternative for modifying hematite surfaces. Previous research has shown that Ga_2O_3 can passivate surface states prone to recombination, thereby making more holes available at active sites for water oxidation.[9–11]

In this chapter we have explored the possible presence of peroxo surface state participating in the OER. Series of *J-V*, EIS and characterization has proved the presence of a surface state which doesn't get to participate in OER after modification with gallium monolayer.

3.3 Experimental Section

3.3.1 Hematite Layer

Hematite thin films were deposited onto 1.1 mm thick aluminoborosilicate glass substrates (Solaronix, 10 Ω/sq) coated with fluorine-doped tin oxide (FTO) on one side. To prepare the FTO substrates, they were cleaned through sonication in soap solution, water, and isopropyl alcohol for 10 minutes each, followed by drying with a nitrogen stream. Hematite films were then fabricated using a modified version of a previously established,[12,13] employing atomic layer deposition (ALD) with the Savannah 100 system from Cambridge Nanotech Inc. Utilizing 'wet ozone' instead of standard ozone proved to be more effective, enhancing the growth rate and film uniformity. The FTO substrates were heated to 200°C, while the ferrocene precursor was maintained at 70°C. Each ALD cycle consisted of a 20-second ferrocene exposure, followed by an oxidation sequence that included 10 subcycles of a 0.015-second H_2O pulse and a 2-second ozone pulse, with each step separated by a 5-second nitrogen purge. The hematite films were synthesized using 1000 ALD cycles, were measured to be approximately 50 nm thick (Detailed in *Chapter 2*) via absorption spectroscopy (Perkin-Elmer Lambda 35 with an integrating sphere) with correction for reflection and substrate. The deposited films were initially annealed at 500°C, heated at a rate of 30°C per minute, held for 30 minutes, and then allowed to cool to room temperature overnight. Subsequently, the electrodes were annealed again at 800°C for 4 minutes in a preheated furnace, followed by rapid cooling to room temperature. Confirmation of the hematite phase was obtained through characterization, as detailed in *Chapter 2*.

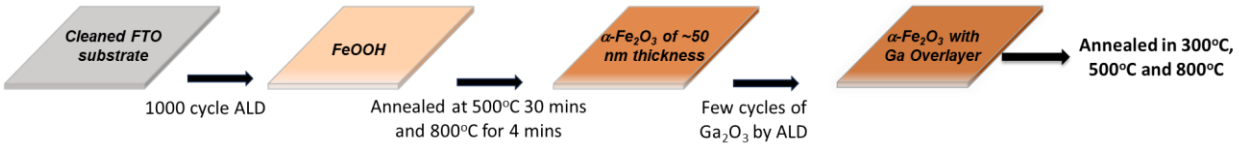

Figure 3.1: Synthesis schematics of GaO_x overlayer Hematite, followed by annealing.

3.3.2 Gallium Overlayer

The synthesis of gallium oxide (Ga_2O_3) was performed following a previously reported procedure. Ga_2O_3 was deposited onto a hematite layer using Atomic Layer Deposition (ALD). Tris-(dimethylamido) gallium(III) ($Ga_2(NMe_2)_6$) from Strem Chemicals Inc. was employed as the gallium precursor, while H_2O served as the oxidizing agent, following a

Cycles of Gallium Layer	Annealing Temperature	Sample Name
0	No annealing	0Ga
1	300°C 10 min	1Ga300
3	300°C 10 min	3Ga300
9	300°C 10 min	9Ga300
1	500°C 10 min	1Ga500
3	500°C 10 min	3Ga500
9	500°C 10 min	9Ga500
1	800°C 10 min	1Ga800
3	800°C 10 min	3Ga800
9	800°C 10 min	9Ga800

Table 3.1: The tables depict all the sample made using different Ga layers and annealing.

modified method from earlier studies.[14] During deposition, the gallium precursor was

maintained at 150°C, and the substrate temperature was held at 200°C. The deposition cycle included a 0.2-second pulse of the gallium precursor with an 8-second exposure, followed by a 12-second N_2 purge. Then, a 0.015-second H_2O pulse was introduced for oxidation under the same exposure and purge conditions. This process was repeated across different cycles to prepare three samples (1, 3, and 9 cycles). The observed growth rate of Ga_2O_3 was approximately 1.1 Å per cycle, consistent with prior report.[14] Ga^{3+} ions can be deposited as $Ga(OH)_3$ or GaO(OH), which convert to crystalline Ga_2O_3 at temperatures between 300–400°C.[15] Hematite and Ga_2O_3 share the same corundum crystal structure, with minimal lattice mismatches of 1.10% for the a-plane and 2.46% for the c-plane.[16] After deposition, all samples were annealed at 300°C, 500°C, and 800°C for 10 minutes. *Table 1* above lists all the required abbreviations for the samples that are used here within this work. Although it's prudent to say that only few cycles of ALD won't produce 3D crystal architecture of Ga_2O_3, from now on in this study few atomic layer of this synthesis can be considered as GaO_x.

3.3.3 Photoelectrochemical Measurements

An O-ring was used to attach the photoelectrode to the custom cell, where 0.28 cm^2 hole area was defined as the active area for all photoelectrochemical measurements, since it's the only area where photoelectrode is in contact with the electrolyte. The experiments were conducted in 1M KOH aqueous solution (pH 13.6, measured with a Fisher Scientific Accumet pH meter). Gallium-overlayered hematite electrodes were secured in a custom-made glass electrochemical cell. A homemade saturated Ag/AgCl electrode was used as the reference electrode, and a high-surface-area platinum mesh served as the counter electrode. Potentials were converted to the reversible hydrogen electrode (RHE) scale

using the equation: $V_{RHE} = V_{Ag/AgCl} + 0.197 + pH\ (0.059)$. Electrochemical Impedance Spectroscopy (EIS) and photoelectrochemical measurements were conducted using an Eco Chemie Autolab potentiostat with Nova electrochemical software. EIS was performed with a 10 mV amplitude perturbation over a frequency range of 10,000 Hz to 0.1 Hz. Data was analyzed with ZView software (Scribner Associates). A 450 W xenon arc lamp (Horiba John) served as the light source, and an AM 1.5 solar filter was used to simulate sunlight at 100 mW cm² (1 sun). All photoelectrochemical measurements were conducted by illuminating the Gallium-overlayered hematite electrodes through the FTO substrate (back illumination) to prevent competing light absorption from the electrolyte. Light and dark *J*–*V* curves were recorded at a scan rate of 20 mV/s.

3.3.4 Raman Spectroscopy

X-ray diffraction (XRD) is commonly used to measure crystallinity, but for the ultrathin films studied here, it is difficult to distinguish hematite peaks from the FTO substrate using PXRD. Instead, Raman spectroscopy, a more surface-sensitive technique, is well-suited for examining amorphous crystalline transitions, oxygen defects, stress, and quantum size effects in metal oxides. Phonon confinement effects,[17,18] which occur when crystal domains are very small, can lead to frequency shifts and asymmetrical broadening in Raman spectra. Thus, Raman spectroscopy was used to assess the crystallinity of the thin films in this study.

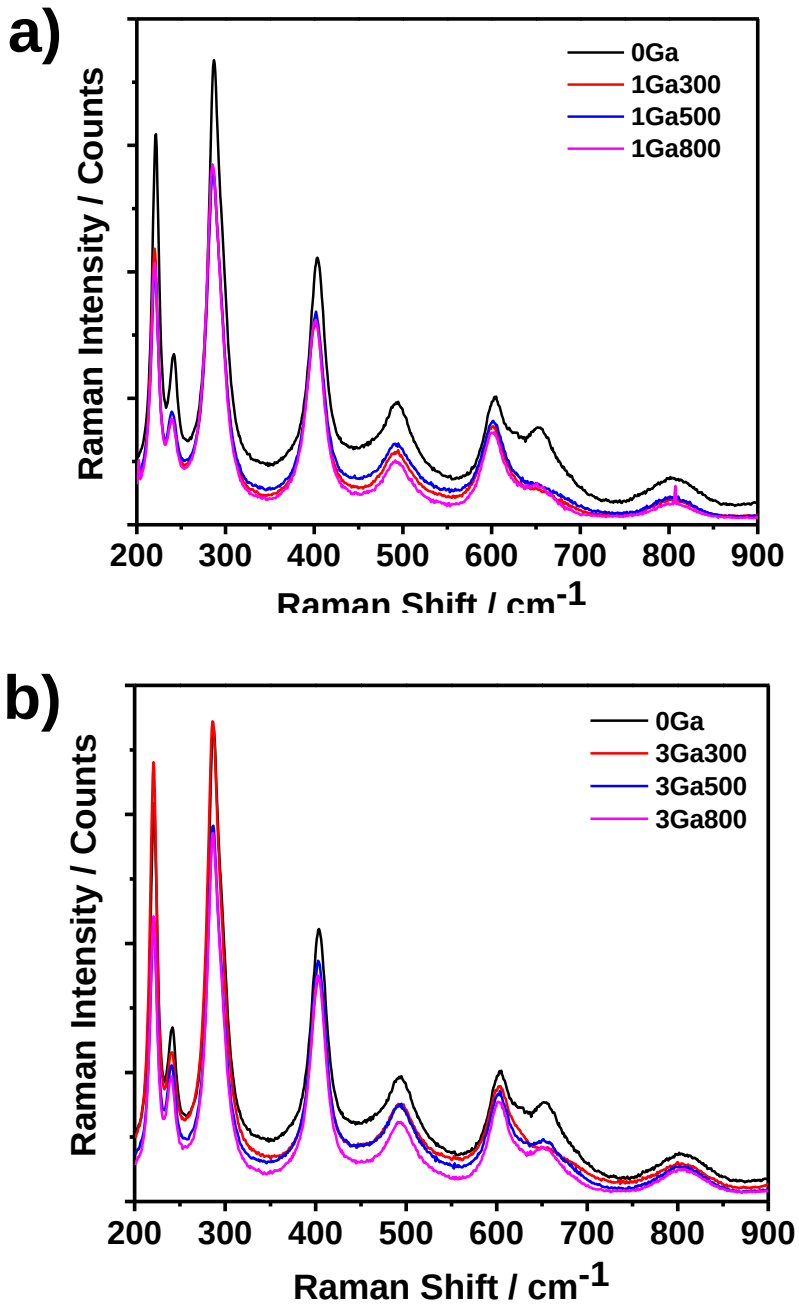

Figure 3.2: Raman Spectroscopy images of a) 1Ga, b) 3Ga and c) 9Ga samples and how it differs due to annealing temperature. Bare hematite without any gallium oxide overlayer has been shown alongside each graph for reference.

Figure 3.2 (cont'd)

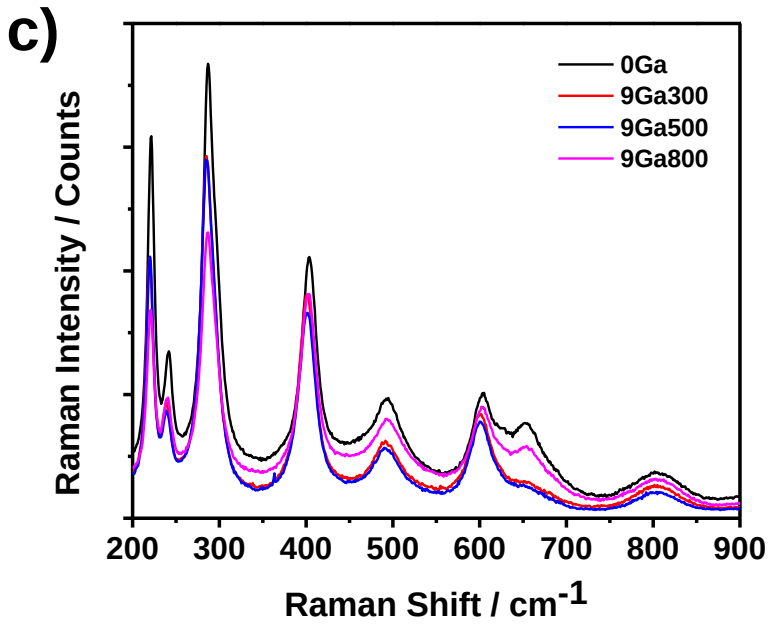

Figure 3.2 illustrates various vibrational modes corresponding to hematite[19], with peaks observed at 220 cm^{-1} (A_{1g}), 240 cm^{-1} (E_g), 280 cm^{-1} (E_g), 400 cm^{-1} (E_g), 500 cm^{-1} (A_{1g}), and 600 cm^{-1} (E_g). These peaks display reduced intensity when a gallium overlayer is applied, irrespective of annealing temperature[14], indicating significant alterations in the surface characteristics and crystallinity of the photoelectrode. Notably, most hematite peaks show increased intensity with elevated annealing temperatures and the presence of a gallium overlayer, suggesting that high temperature annealing with Ga_2O_3 influences crystal growth, resulting in a reduced bandgap[20]. Additionally, the 660 cm^{-1} peak, attributed to magnetite contamination, consistently decreases across all samples after gallium overlayer application and annealing.[19,21]

3.4 Results and Discussion

The photoelectrochemical water oxidation behavior of our all 10 samples (*Table 1*) was evaluated in an alkaline electrolyte under 1 Sun illumination in *Figure 3.3*. Despite variations in annealing temperature and the presence of a gallium overlayer, none of the samples showed improved photocurrent or a shift in the onset potential for OER efficiency. Previous studies have demonstrated that coating hematite with non-catalytic oxides like Ga_2O_3 and In_2O_3[10,22] can enhance OER performance by cathodically shifting the onset potential. Currently it is quite well established that during OER, holes accumulate on a surface states rather than directly transfer from the valence band edge; this surface state acts as reaction intermediates in water oxidation rather than merely serve as charge traps,[23] leading to site for electron-hole recombination. Recent findings suggest that a Fe^{IV}=O intermediate[24] may play a role in water oxidation and it was linked to the absorption peak at 572 nm observed in Photo induced Absorption Spectroscopy (PIAS)

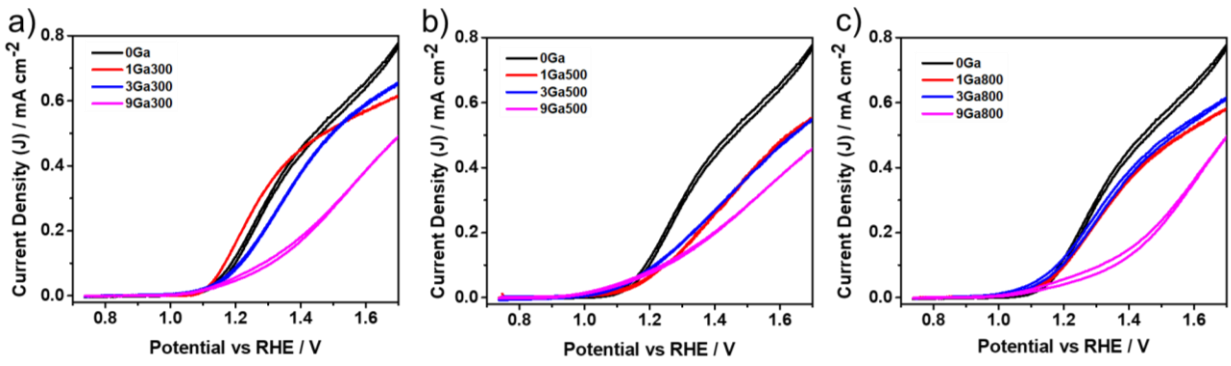

Figure 3.3: Three graphs show the *j-V* response in presence of 1 M KOH, pH 13.6 under 1 Sun illumination. a) Annealing temperature 300°C b) Annealing temperature 500°C c) Annealing temperature 800°C. Bare hematite without any further annealing has been shown for reference.

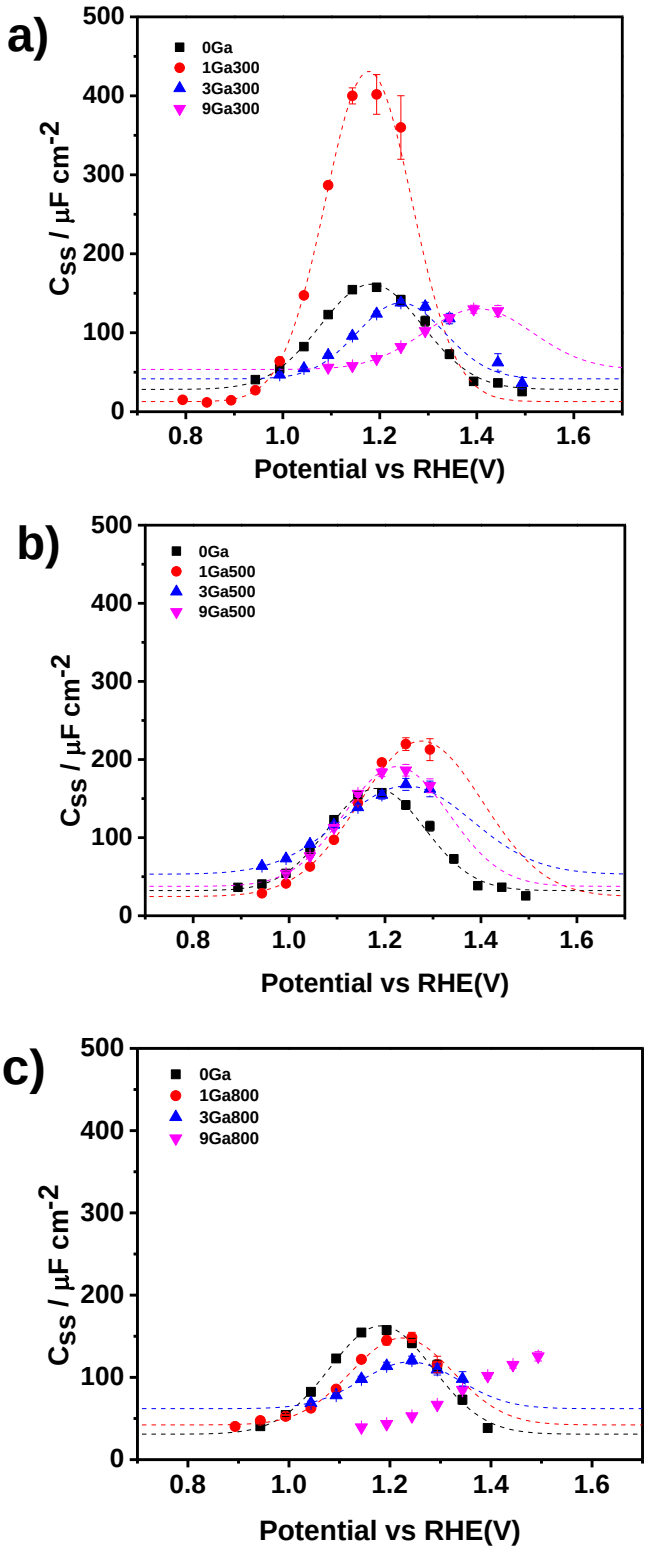

Figure 3.4: C_{ss} or Surface capacitances calculated from Nyquist plots in 1 M KOH and 1

Figure 3.4 (cont'd)

Sun illumination. a) Annealing temperature 300°C b) Annealing temperature 500°C c) Annealing temperature 800°C.

studies and peak at 898 cm^{-1} in operando *ATR-IR* measurement.[2,3] Additionally, recent studies indicate that a peroxo adsorbate is a stable species in OER[8,11,25], prompting questions about its involvement in water oxidation and potential contribution to midgap states.

Photoelectrochemical Impedance Spectroscopy (EIS) was conducted under water oxidation conditions, and the Nyquist plots were fitted to equivalent circuits previously discussed. These circuits model electron-hole generation, recombination, and transfer as various capacitances and resistances. The surface state capacitance (C_{ss}) helps explain how hole accumulation at the surface is a key step in initiating water oxidation, while this accumulation reduces charge transfer resistance (R_{ct}) as shown in both *Figure 3.4* and *Figure 3.5.d, 3.5.e and 3.5.f*.

In *Figure.3.4.a*, the 1Ga sample shows significant hole accumulation before water oxidation, yet no corresponding increase in photocurrent, suggesting many holes do not participate in the oxygen evolution reaction (OER). Instead, they may be trapped in mid-gap states, leading to recombination with bulk electrons in hematite. Computational studies[11] suggest that 1Ga-modified hematite may form peroxo terminations during OER, with two types of mid-gap states: one acting as a "spectator" where holes recombine rather than contribute to water oxidation, and the other involved in the reaction.

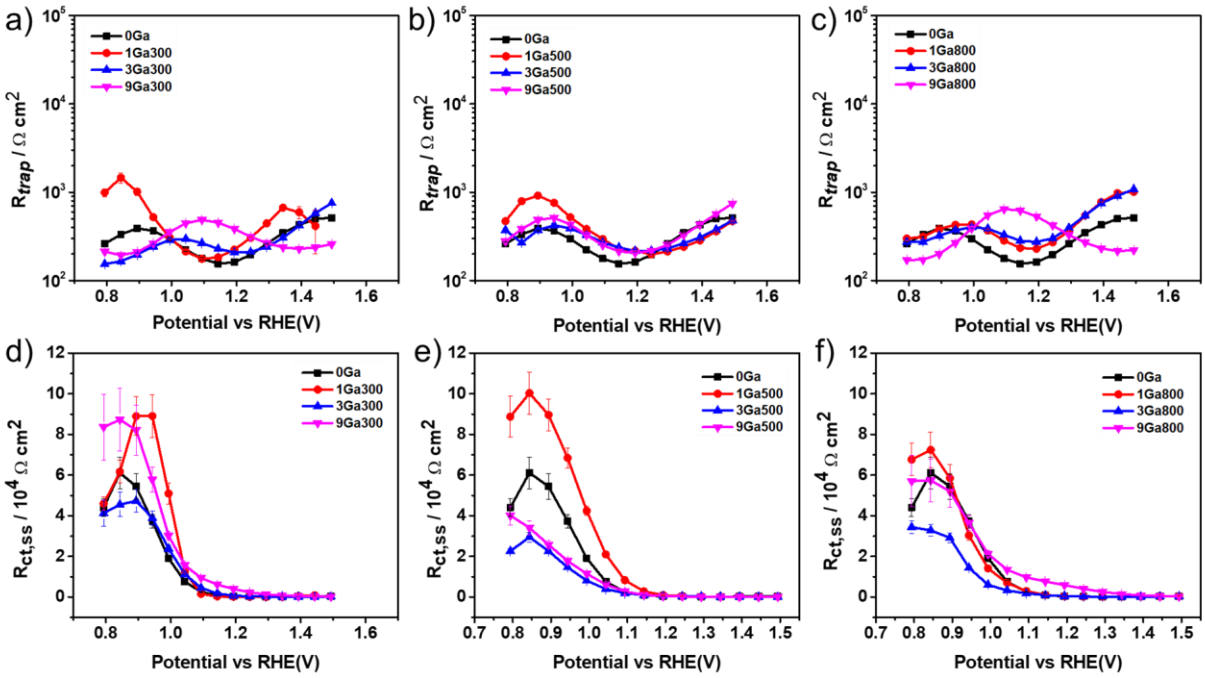

Figure 3.5: illustrates the R_{ct} and R_{trap} parameters extracted from Nyquist plots after EIS measurements in 1M KOH under 1 Sun illumination. The graphs display data for 1Ga, 3Ga, and 9Ga samples. Panels a), b), and c) show trap resistance for samples annealed at 300°C, 500°C, and 800°C, respectively. Panels d), e), and f) present charge transfer resistance for the same annealing temperatures (300°C, 500°C, and 800°C).

In contrast, at the 0Ga surface (without peroxo species, bare hematite), a competition exists between active water oxidation sites and other surface states, which trap holes. The Ga_2O_3 layer passivates these trapping sites, freeing holes for active water oxidation. Additionally, the conduction band of Ga_2O_3 is higher in energy than that of hematite, preventing photogenerated electron recombination at the surface.

In *Figure 3.4*, particularly for the 1Ga samples (*Figure 3.4.a*), we see that increasing the annealing temperature reduces C_{ss}, indicating a decrease in hole trapping at the midgap peroxo termination, earler referred as the 'spectator' state. This aligns with findings by Zandi et al.,[26] where high-temperature annealing of ALD-hematite removed surface states at lower potentials, resulting in improved OER efficiency. Thus, eliminating these trapping states could increase the availability of holes for OER in bare hematite. This is further corroborate by *Figure 3.5.a, 3.5.b* and *3.5.c* where we see R_{trap} is decreasing with increasing annealing temperature.

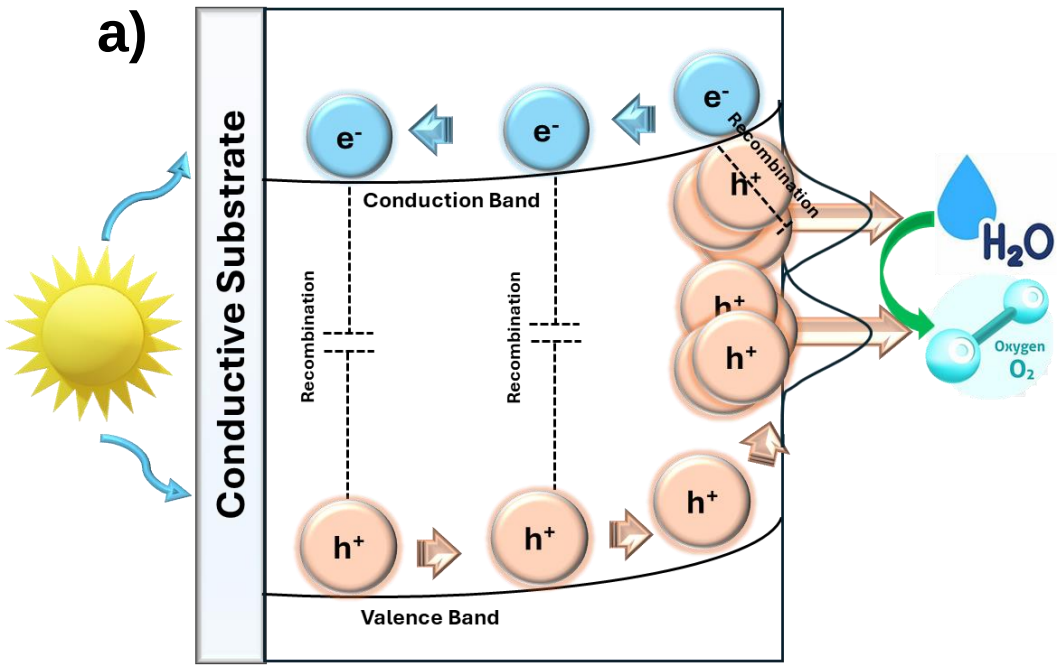

Figure 3.6: Schematics of OER in presence of two surface states and how the population of holes change at the peroxo surface state before a) and after b) high temperature annealing, acting merely as a 'Spectator'.

Figure 3.6 (cont'd)

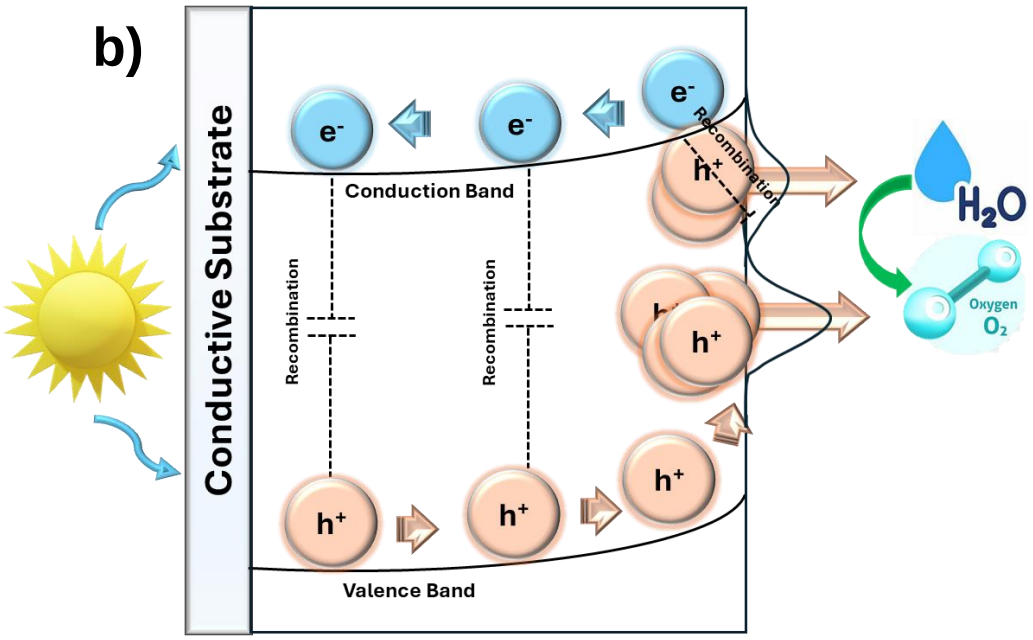

Sample	Dopant Density (N_D) / cm^{-3}	Flatband Potential (V_{fb}) / V_{RHE}
0Ga	1.72 (±0.06) x 10^{19}	0.84 (±0.02)
1Ga300	6.60 (±0.26) x 10^{18}	0.84 (±0.01)
3Ga300	2.35 (±0.07) x 10^{19}	0.76 (±0.02)
9Ga300	6.30 (±0.61) x 10^{19}	0.75 (±0.07)
1Ga500	1.01 (±0.04) x 10^{19}	0.91 (±0.02)
3Ga500	1.45 (±0.07) x 10^{19}	0.92 (±0.02)
9Ga500	1.62 (±0.02) x 10^{19}	0.81 (±0.01)
1Ga800	1.96 (±0.05) x 10^{19}	0.78 (±0.02)
3Ga800	2.18 (±0.05) x 10^{19}	0.78 (±0.02)
9Ga800	4.38 (±0.23) x 10^{19}	0.86 (±0.04)

Table 3.2: Flatband potential and Dopant Density for different samples after Mott-Schottky analysis.

EIS data, specifically C_{bulk} parameters, were analyzed to understand bulk phenomena,

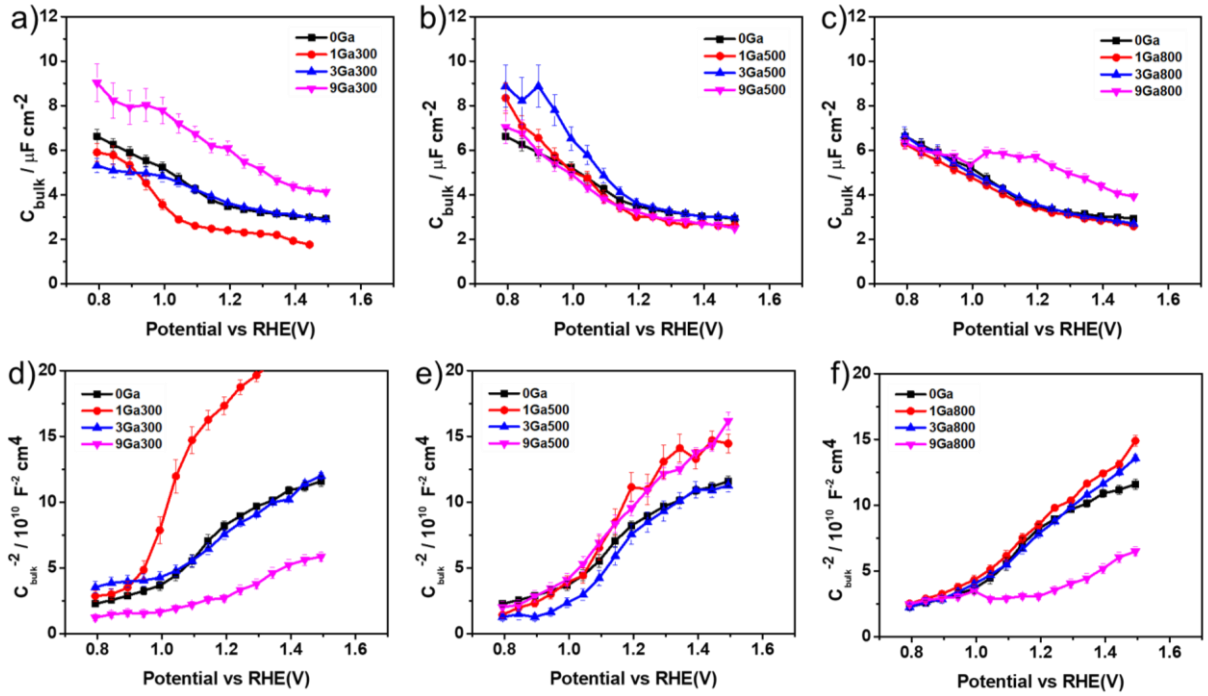

Figure 3.7: presents the bulk capacitance (C_{bulk}) derived from Nyquist plots following EIS measurements in 1M KOH under 1 Sun illumination, alongside Mott-Schottky analysis using C_{bulk} data. The graphs depict results for the 1Ga, 3Ga, and 9Ga samples. Panels a), b), and c) illustrate the bulk capacitance for samples annealed at 300°C, 500°C, and 800°C, respectively, while panels d), e), and f) show the corresponding Mott-Schottky analysis for these temperatures. The Mott-Schottky analysis allows for determining key parameters such as flatband potential (V_{fb}) and donor density (N_D).

and Mott-Schottky analysis (Discussed in *Chapter 2*) was conducted for further insights

into the band structure (*Figure 3.7*). In surface state passivation, no changes in flatband potential (V_{fb}) or dopant density (N_D) are typically expected.[22] Any variations in these parameters suggest possible changes in band structure. For our samples, calculations of V_{fb} and N_D showed no significant trends as shown in *Table 3.2* above, supporting the hypothesis that gallium overlayer passivates surface states, reducing charge accumulation that pins band edges, which acts as a spectator trap site for holes. This passivation un-pins the band edges, stabilizing their position This trap site coexists with iron oxo sites on hematite[11], interacting dynamically during the OER, complicating the overall mechanism.[5]

Among the experimental results, the 9Ga samples stand out as outliers. These samples exhibit significantly lower *J-V* activity (*Figure 3.3*), and their *Css* (*Figure 3.4*) curves show minimal surface charge accumulation. The C_{ss} peak shifts toward anodic potential, matching the *J-V* onset. Interestingly, after exposing the thicker 9Ga samples to continuous PEC conditions for one hour, the photocurrent increases (*Figure 3.8.a, b and c*), and the onset potential shifts cathodically. A similar effect was reported by Gratzel et al.,[10] who observed Ga_2O_3 nanoparticle formation after 24 hours of PEC, confirmed by XPS data. During fast cyclic voltammetry experiment as shown in *Figure. 3.8.e*, the lower potential peak decreases post-PEC, supporting the hypothesis that Ga_2O_3 modification

increases hole density at 'spectator' trap sites which is the peak at 0.7 V_{RHE}. As Ga_2O_3 forms nanoparticles, hematite is exposed, causing the lower potential peak to diminish.

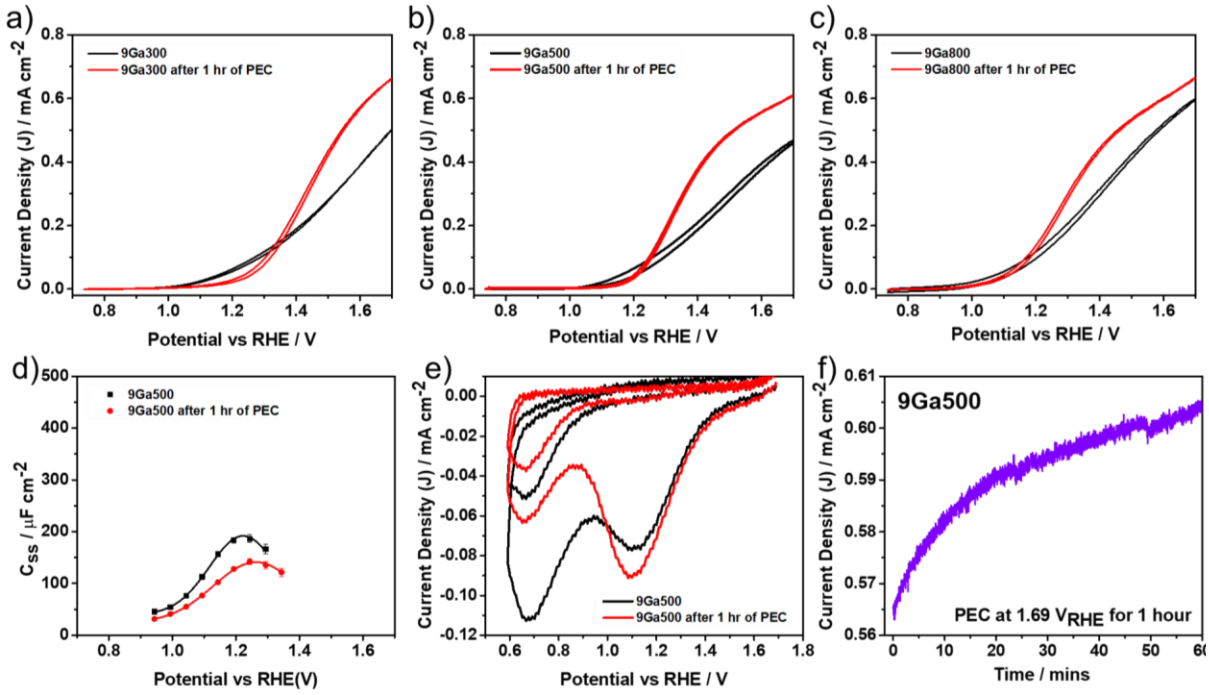

Figure 3.8: Presents data for the 9Ga samples. Chronoamperometry (PEC) was performed at 1.69 V_{RHE} for 1 hour under 1 Sun illumination, with *J-V* measurements taken both before and after the chronoamperometry. Panels a), b), and c) show the *J-V* curves for 9Ga samples annealed at 300°C, 500°C, and 800°C, respectively. Panel d) displays the C_{ss} characteristics of the 9Ga500 sample before and after 1 hour of PEC. In panel e), a fast cyclic voltammetry (CV) experiment is shown for the 9Ga500 sample, conducted before and after PEC. The fast CV method involved holding the system at 2.0 V_{RHE} for 60 seconds under 1 Sun illumination, then switching off the light and scanning CV from high to low potentials for several cycles. f) demonstrates how current density increased over the course of the 1-hour PEC experiment, suggesting Ga etching.

3.5 Conclusion

In this chapter, we explored the effect of a Ga_2O_3 overlayer on ALD hematite using Raman spectroscopy*, J-V* measurements, and EIS under PEC OER conditions. The experiments suggest hematite has two surface states, one of them is well established iron oxo, another can be the speculated iron peroxo, due gallium modification this peroxo terminal ets modified or passvated in this case, where during OER the holes get accumulated and eventually recombined. During higher temperature anneal this peroxo state gets passivated even more so less holes acmulates then. This species accumulates holes, which eventually recombine, shedding light on the presence of parallel water oxidation pathways driven by multiple surface states, further complicating the 4-electron mechanism of water oxidation. However, some aspects remain unclear: (1) the exact proof of chemical nature of the peroxo surface state is still uncertain. While Zhao et al.[25] demonstrated the existence of this complex using ATR-IR in OER, their choice of electrolyte raises questions due to potential IR absorption interference; (2) experimentally inhibiting iron-oxo intermediates from participating in OER could help clarify the role of these peroxo surface states.

REFERENCES

(1) Pendlebury, S. R.; Cowan, A. J.; Barroso, M.; Sivula, K.; Ye, J.; Grätzel, M.; Klug, D. R.; Tang, J.; Durrant, J. R. Correlating Long-Lived Photogenerated Hole Populations with Photocurrent Densities in Hematite Water Oxidation Photoanodes. *Energy Environ. Sci.* **2012**, *5* (4), 6304–6312. https://doi.org/10.1039/C1EE02567H.

(2) Zandi, O.; Hamann, T. W. Determination of Photoelectrochemical Water Oxidation Intermediates on Hematite Electrode Surfaces Using Operando Infrared Spectroscopy. *Nat Chem* **2016**, *8* (8), 778–783. https://doi.org/10.1038/nchem.2557.

(3) Klahr, B.; Hamann, T. Water Oxidation on Hematite Photoelectrodes: Insight into the Nature of Surface States through In Situ Spectroelectrochemistry. *The Journal of Physical Chemistry C* **2014**, *118* (19), 10393–10399. https://doi.org/10.1021/jp500543z.

(4) Le Formal, F.; Pastor, E.; Tilley, S. D.; Mesa, C. A.; Pendlebury, S. R.; Grätzel, M.; Durrant, J. R. Rate Law Analysis of Water Oxidation on a Hematite Surface. *J Am Chem Soc* **2015**, *137* (20), 6629–6637. https://doi.org/10.1021/jacs.5b02576.

(5) Tsyganok, A.; Monroy-Castillero, P.; Piekner, Y.; Yochelis, A.; Rothschild, A. Parallel Water Photo-Oxidation Reaction Pathways in Hematite Photoanodes: Implications for Solar Fuel Production. *Energy Environ. Sci.* **2022**, *15* (6), 2445–2459. https://doi.org/10.1039/D1EE03953A.

(6) Fabbri, E.; Schmidt, T. J. Oxygen Evolution Reaction—The Enigma in Water Electrolysis. *ACS Catal* **2018**, *8* (10), 9765–9774. https://doi.org/10.1021/acscatal.8b02712.

(7) Busch, M. Water Oxidation: From Mechanisms to Limitations. *Curr Opin Electrochem* **2018**, *9*, 278–284. https://doi.org/https://doi.org/10.1016/j.coelec.2018.06.007.

(8) Li, J.; Wan, W.; Triana, C. A.; Chen, H.; Zhao, Y.; Mavrokefalos, C. K.; Patzke, G. R. Reaction Kinetics and Interplay of Two Different Surface States on Hematite Photoanodes for Water Oxidation. *Nat Commun* **2021**, *12* (1), 255. https://doi.org/10.1038/s41467-020-20510-8.

(9) Steier, L.; Herraiz-Cardona, I.; Gimenez, S.; Fabregat-Santiago, F.; Bisquert, J.; Tilley, S. D.; Grätzel, M. Understanding the Role of Underlayers and Overlayers in Thin Film Hematite Photoanodes. *Adv Funct Mater* **2014**, *24* (48), 7681–7688. https://doi.org/https://doi.org/10.1002/adfm.201402742.

(10) Hisatomi, T.; Le Formal, F.; Cornuz, M.; Brillet, J.; Tétreault, N.; Sivula, K.; Grätzel, M. Cathodic Shift in Onset Potential of Solar Oxygen Evolution on Hematite by

13-Group Oxide Overlayers. *Energy Environ. Sci.* **2011**, *4* (7), 2512–2515. https://doi.org/10.1039/C1EE01194D.

(11) Ulman, K.; Nguyen, M.-T.; Seriani, N.; Piccinin, S.; Gebauer, R. A Unified Picture of Water Oxidation on Bare and Gallium Oxide-Covered Hematite from Density Functional Theory. *ACS Catal* **2017**, *7* (3), 1793–1804. https://doi.org/10.1021/acscatal.6b03162.

(12) Klahr, B.; Gimenez, S.; Fabregat-Santiago, F.; Hamann, T.; Bisquert, J. Water Oxidation at Hematite Photoelectrodes: The Role of Surface States. *J Am Chem Soc* **2012**, *134* (9), 4294–4302. https://doi.org/10.1021/ja210755h.

(13) Klahr, B. M.; Martinson, A. B. F.; Hamann, T. W. Photoelectrochemical Investigation of Ultrathin Film Iron Oxide Solar Cells Prepared by Atomic Layer Deposition. *Langmuir* **2011**, *27* (1), 461–468. https://doi.org/10.1021/la103541n.

(14) Zandi, O.; Beardslee, J. A.; Hamann, T. Substrate Dependent Water Splitting with Ultrathin α-Fe2O3 Electrodes. *The Journal of Physical Chemistry C* **2014**, *118* (30), 16494–16503. https://doi.org/10.1021/jp4116657.

(15) Taş, A. C.; Majewski, P. J.; Aldinger, F. Synthesis of Gallium Oxide Hydroxide Crystals in Aqueous Solutions with or without Urea and Their Calcination Behavior. *Journal of the American Ceramic Society* **2002**, *85* (6), 1421–1429. https://doi.org/https://doi.org/10.1111/j.1151-2916.2002.tb00291.x.

(16) Kaneko, K.; Nomura, T.; Kakeya, I.; Fujita, S. Fabrication of Highly Crystalline Corundum-Structured α-$(Ga_{1-x}Fe_x)_2O_3$ Alloy Thin Films on Sapphire Substrates. *Applied Physics Express* **2009**, *2* (7), 75501. https://doi.org/10.1143/APEX.2.075501.

(17) Balaji, S.; Djaoued, Y.; Robichaud, J. Phonon Confinement Studies in Nanocrystalline Anatase-TiO_2 Thin Films by Micro Raman Spectroscopy. *Journal of Raman Spectroscopy* **2006**, *37* (12), 1416–1422. https://doi.org/https://doi.org/10.1002/jrs.1566.

(18) Subramanian, B.; Djaoued, Y.; Robichaud, J. Phonon Confinement Studies in Nanocrystalline Anatase-TiO_2 Thin Films by Micro Raman Spectroscopy. *Journal of Raman Spectroscopy* **2006**, *37*, 1416–1422. https://doi.org/10.1002/jrs.1566.

(19) Jubb, A. M.; Allen, H. C. Vibrational Spectroscopic Characterization of Hematite, Maghemite, and Magnetite Thin Films Produced by Vapor Deposition. *ACS Appl Mater Interfaces* **2010**, *2* (10), 2804–2812. https://doi.org/10.1021/am1004943.

(20) Makeswaran, N.; Battu, A. K.; Swadipta, R.; Manciu, F. S.; Ramana, C. V. Spectroscopic Characterization of the Electronic Structure, Chemical Bonding, and Band Gap in Thermally Annealed Polycrystalline Ga_2O_3 Thin Films. *ECS Journal of Solid State Science and Technology* **2019**, *8* (7), Q3249–Q3253. https://doi.org/10.1149/2.0461907jss.

(21) Rao, R.; Rao, A. M.; Xu, B.; Dong, J.; Sharma, S.; Sunkara, M. K. Blueshifted Raman Scattering and Its Correlation with the [110] Growth Direction in Gallium Oxide Nanowires. *J Appl Phys* **2005**, *98*, 94312.

(22) Le Formal, F.; Tétreault, N.; Cornuz, M.; Moehl, T.; Grätzel, M.; Sivula, K. Passivating Surface States on Water Splitting Hematite Photoanodes with Alumina Overlayers. *Chem. Sci.* **2011**, *2* (4), 737–743. https://doi.org/10.1039/C0SC00578A.

(23) Young, K. M. H.; Klahr, B. M.; Zandi, O.; Hamann, T. W. Photocatalytic Water Oxidation with Hematite Electrodes. *Catal. Sci. Technol.* **2013**, *3* (7), 1660–1671. https://doi.org/10.1039/C3CY00310H.

(24) Yatom, N.; Neufeld, O.; Caspary Toroker, M. Toward Settling the Debate on the Role of Fe_2O_3 Surface States for Water Splitting. *The Journal of Physical Chemistry C* **2015**, *119* (44), 24789–24795. https://doi.org/10.1021/acs.jpcc.5b06128.

(25) Zhang, Y.; Zhang, H.; Liu, A.; Chen, C.; Song, W.; Zhao, J. Rate-Limiting O–O Bond Formation Pathways for Water Oxidation on Hematite Photoanode. *J Am Chem Soc* **2018**, *140* (9), 3264–3269. https://doi.org/10.1021/jacs.7b10979.

(26) Zandi, O.; Hamann, T. W. Enhanced Water Splitting Efficiency Through Selective Surface State Removal. *J Phys Chem Lett* **2014**, *5* (9), 1522–1526. https://doi.org/10.1021/jz500535a.

Chapter 4:

Investigation of Photoelectrochemical Water Oxidation Intermediates on $CuWO_4$ surface using Spectroelectrochemical Techniques

4.1 Abstract

Understanding the mechanism is crucial for developing effective electrocatalysts to accelerate oxygen evolution reactions (OER). Identifying reaction intermediates is equally important for this purpose. Currently, there are few reports on the surface states involved in $CuWO_4$. In this study, we employed a series of spectroelectrochemical techniques to investigate the optical and chemical properties of the surface states associated with water oxidation. Photoinduced absorption spectroscopy (PIAS) indicates the formation of an intermediate involved in charge transfer reactions, likely to represent oxo, peroxo, or superoxo species. Additionally, operando ATR-IR experimental data further supports the PIAS findings by providing strong evidence for the presence of oxo and superoxo species. Together, these results confirm the nature of the surface states as intermediates in the water oxidation process on the $CuWO_4$ photoanode.

4.2 Introduction

$CuWO_4$ is a promising n-type material with an indirect bandgap of 2.3 eV. Under the AM 1.5 solar spectrum, $CuWO_4$ has a theoretical photocurrent density of 9 mA cm^{-2} in an ideal PEC cell, with a maximum theoretical solar-to-hydrogen efficiency of 11%. Composed of earth-abundant elements, $CuWO_4$ performs well in neutral to slightly basic PEC reaction conditions and exhibits long-term stability.[1]

However, the PEC performance of $CuWO_4$ is constrained by limitations in charge separation and hole collection efficiencies[23] To address these challenges, several strategies have been employed, including nanostructuring[4] and doping[2]. A significant barrier to practical application lies in the limited understanding of the material's fundamental properties, particularly regarding:

1. **Bulk Charge Separation:** The mechanisms involved in charge separation within the bulk of $CuWO_4$ are not well understood.
2. **Charge Transfer at the Electrode/Electrolyte Interface:** The interactions between the electrode and the electrolyte play a crucial role in the efficiency of the reaction yet remain poorly characterized.
3. **Nature and Role of Surface States:** The surface states that potentially influenced charge dynamics are not fully elucidated.

Research conducted by Gao et al.[3] utilized intensity-modulated photocurrent spectroscopy (IMPS) to study the hole collection properties of $CuWO_4$, examining various hole scavengers. Additionally, studies by Bartlett and coworkers[5] indicated that low charge separation efficiency may arise from a mid-gap state between the valence band (VB) and conduction band (CB), which contributes to significant surface recombination

under both dark and illuminated conditions. This intrinsic mid-gap state arises from the delocalized Cu(*3d*) orbitals and is present even in the dark.

Holes from the VB can either directly oxidize water or become trapped in the mid-gap state before transferring into the solution. Meanwhile, photogenerated electrons in the CB can migrate to the bulk, recombine with VB holes, or transfer to the mid-gap state.

Recent work by Yuan Gao[6] from our group suggested that the surface states involved in water oxidation on the $CuWO_4$ surface are not intrinsic but rather evolve as intermediates during the water oxidation reaction, like Fe_2O_3. This indicates that the maximum number of holes is stored on the surface until water oxidation is initiated. We hypothesize that these surface states evolve as intermediates during the water oxidation reaction in $CuWO_4$. However, to date, there have been no reports detailing the nature and role of these surface states. In this chapter, we employ various spectroelectrochemical techniques to investigate the intermediates involved in the OER, while also acknowledging some experimental limitations of our study and proposing strategies to further advance this research. In our hypothesis, a wide range of metal oxo, peroxo and superoxo intermediates are probable intermediates, confirmed by a peak at 440 nm in PIAS and IR peaks at 750 cm^{-1}, 1050 cm^{-1} and 1300 cm^{-1} during ATR-IR operando experiments.

4.3 Experimental Section

4.3.1 $CuWO_4$ film preparation

$CuWO_4$ thin films were synthesized via a sol-gel technique (Spray Pyrolysis) using an adapted version of a previously established method. [7] The films were deposited onto a 1.1 mm thick aluminoborosilicate glass substrate (Solaronix, 10 Ω/sq) that was coated on one side with fluorine-doped tin oxide (FTO). The FTO substrates underwent a cleaning process involving sonication in soap solution, water, and isopropyl alcohol, each for 10 minutes, followed by drying with a nitrogen (N_2) stream. An aqueous precursor solution containing $CuCl_2$ and ammonium metatungstate (AMT) was prepared, maintaining equimolar concentrations of Cu^{2+} and W^{6+} ions (0.01 M). The FTO substrate was then placed on a hot plate set to 275 °C, and the precursor solution was sprayed onto the heated surface using a glass nozzle with a deposition cycle of 1-second spraying and a 5-second resting interval (*Figure 4.1*). This 5-second pause between sprays allowed the solvent to evaporate during each cycle. The reaction proceeded according to the following equation:

$$12CuCl_2(aq) + (NH_4)_6H_2W_{12}O_{40}(aq) + 8H_2O(l) = 12CuWO_4(s) + 6NH_3(g) + 24HCl(g)$$

The film thickness was regulated by adjusting the total volume of the precursor solution used. Post-deposition, the films were subjected to crystallization through annealing in a furnace for 1 hour at 550 °C. For this experiment, a total of 20 mL of the precursor solution was used to fabricate the $CuWO_4$ thin film, and all subsequent characterizations and experiments were conducted using this sample.

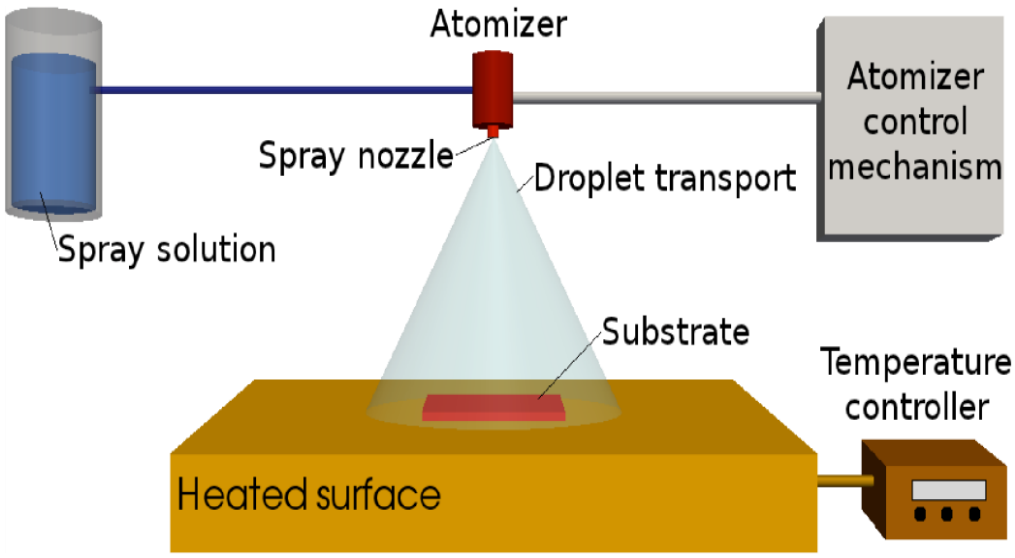

Figure 4.1: Experimental setup for $CuWO_4$ preparation by Spray Pyrolysis method.

4.3.2 Film Characterization

Powder X-ray diffraction (PXRD) was carried out using a Bruker Davinci Diffractometer operating at 40 kV and 40 mA with Cu Kα radiation. The PXRD analysis (*Figure 4.2.b*) confirmed the formation of $CuWO_4$ (PDF 01-080-5325), which was further verified by Raman Spectroscopy (*Figure 4.2.d*). X-ray photoelectron spectroscopy (XPS) measurements were performed at a takeoff angle of 45° utilizing a Perkin Elmer Phi 5600 ESCA system equipped with a magnesium Kα X-ray source. The XPS spectra displayed (*Figure 4.2.c*) the characteristic W *4d*, Cu *2p*, and O *2p* peaks corresponding to $CuWO_4$. The thickness of the film prepared from the 20 mL precursor solution was determined to be 300 nm through cross-sectional scanning electron microscopy (SEM) using a Carl Zeiss Microscope. The cross-sectional image is shown in (*Figure 4.2.a*), while the top-view reveals the surface morphology and crystallite structure of the film.

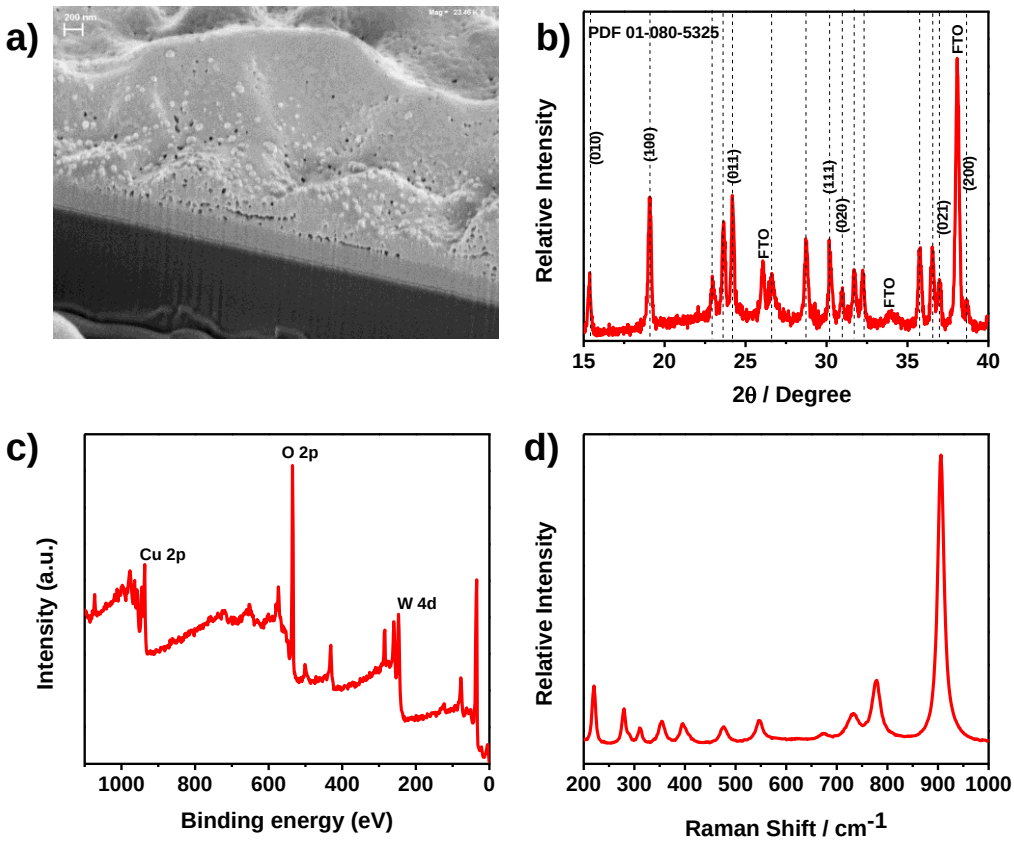

Figure 4.2: a) Shows the Cross Section SEM images which confirms a thickness of 300 nm, also it offers the top view of $CuWO_4$. b) Powder X-ray Diffraction analysis of $CuWO_4$ thin film. c) X-ray Photoelectron Spectroscopy shows the presence of Cu *2p*, O *2p* and W *4d* states. d) Raman spectroscopy of $CuWO_4$.

4.3.3 Photoelectrochemical Measurements

$CuWO_4$ on FTO was used as the working electrode in a three-electrode photoelectrochemical setup with an Eco Chemie Autolab potentiostat (Nova electrochemical software) in back illumination configuration (photon passing through the electrode surface before reaching the solution). A homemade saturated Ag/AgCl, and Pt mesh were used as reference and counter electrode. All measurements were carried out

at room temperature in 1.0 M KBi buffer solution at pH 9 (Fisher Scientific Accumet pH meter) made up of KOH pallets and H_3BO_3. Aqueous solutions were prepared with ultra-pure water (resistivity 18 MΩ.cm) from a Milli-Q water purifier.

A 450 W Xe arc lamp (Horiba Jobin Yvon) was used as white light source with an AM 1.5 solar filter to obtain simulated solar spectrum with 100 mW cm^{-2} (1 sun) intensity. All electrochemical potentials are reported with respect to the reversible hydrogen electrode (RHE)

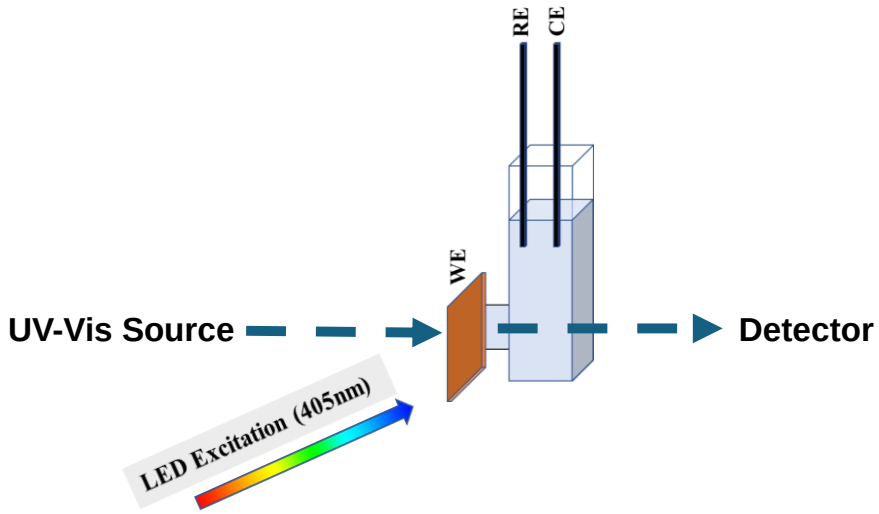

Figure 4.3: Schematic of PIAS experimental setup. WE was mounted on a side of Cuvette with a hole. Cuvette was placed in between Source and Detector of the spectrophotometer. 405 nm laser excitation source was pointed towards the WE making sure it's targeting the place where WE is in touch with the electrolyte.

4.3.4 Photo Induced Absorption Spectroscopy (PIAS)

The electrodes were secured to a 1 cm quartz cuvette that had a cut-out to enable electrolyte contact with the electrode surface. A 2 mm homemade Ag/AgCl electrode served as the reference, while a 0.5 mm platinum wire functioned as the counter

electrode. This entire arrangement was positioned inside a PerkinElmer Lambda 35 UV-vis spectrometer. Electrical connections from a μAUTOLAB III unit were integrated into the UV-vis chamber. To illuminate the $CuWO_4$ sample with monochromatic light, a 405 nm, 40 mW laser diode (Sanyo), managed by a ThorLabs benchtop current controller, was employed. Four pieces of a 475 nm long-pass filter were placed to block the laser from reaching the UV-vis detector, ensuring an optimal signal-to-noise ratio. The experimental setup is illustrated in *Figure 4.3.*

4.3.5 Operando ATR-IR Spectroscopy

The experimental setup was inspired by one of our previous studies where operando ATR-IR was done to investigate the chemical nature of surface states involved during OER of Hematite in alkaline media[8]. The $CuWO_4$ electrodes were cut into dimensions of 1 cm x 5 cm, and two small holes were drilled at both ends to accommodate the counter electrode (CE) and reference electrode (RE). Copper wires were attached to the electrodes using silver paste, and the electrical connections were then insulated with epoxy resin (Loctite EA-1C). Given that the ATR beam penetrates only a few microns in depth, a very thin layer of electrolyte (20 μL) was utilized (either 0.1 M KCl in D_2O with pH 7.3 or 1.0 M KBi in H_2O with pH 9). The electrolyte was applied between the ZnSe ATR crystal and the $CuWO_4$ photoanode. A custom-made small Ag/AgCl reference electrode and a platinum wire as the counter electrode were employed. The RE and CE were positioned through the small holes on the backside of the $CuWO_4$ working electrode (WE) to ensure electrical contact through the thin electrolyte layer. The $CuWO_4$ electrode was securely held in place using a Teflon holder. For the photoelectrochemical (PEC) measurements, a UV LED flashlight (395 nm) served as the light source. The

experimental setup for operando PEC IR measurements is depicted in (*Figure 4.4*). All potentials in the KBi buffer were referenced to the reversible hydrogen electrode (RHE). Infrared (IR) spectra were collected using a Magna-IR 550 Spectrometer equipped with a Gateway Flow Through Top-Plate cell in a multi-reflection ATR setup (Specac). A ZnSe

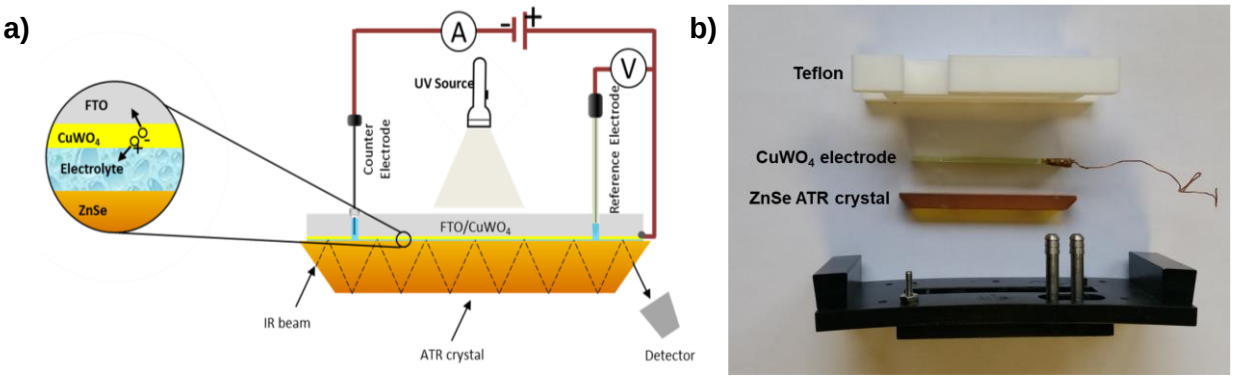

Figure 4.4: Schematic of the experimental setup for operando ATR-IR measurements. a) Depicts a thin layer of electrolyte was introduced between WE and ZnSe crystal, then CE and RE was mounted on the setup. b) Actual picture of the customize setup, the WE was placed between ATR setup and Teflon station.

crystal with a 45° angle and a cut-off energy of 625 cm^{-1} was employed. Operando measurements were performed as a function of both light illumination and applied potential. Each IR spectrum was obtained by averaging 64 scans at a resolution of 4 cm^{-1}, with background correction applied before each measurement. All electrochemical measurements were conducted using a micro-Autolab potentiostat.

4.4 Results and Discussion

The photoelectrochemical (PEC) water oxidation behavior of $CuWO_4$, prepared from a 20 mL precursor solution, was assessed by measuring the current density (J) versus the applied potential (V) in a 1 M KBi buffer (pH=9) under both illuminated (1 Sun) and dark conditions as shown in *Figure 4.5* In alignment with previous studies, $CuWO_4$ exhibited a lower efficiency than hematite.[6] Prior research[6,9] has shown that the oxygen evolution reaction (OER) on $CuWO_4$ is facilitated by surface hole accumulation, like hematite[10]. This was predominantly verified through electrochemical impedance spectroscopy (EIS) conducted under PEC OER conditions over a range of applied potentials, where the surface state capacitance (C_{ss}) displayed a Gaussian trend centered around the photocurrent onset potential (1.0 V_{RHE}). Additional confirmation came from rapid cyclic voltammetry, which

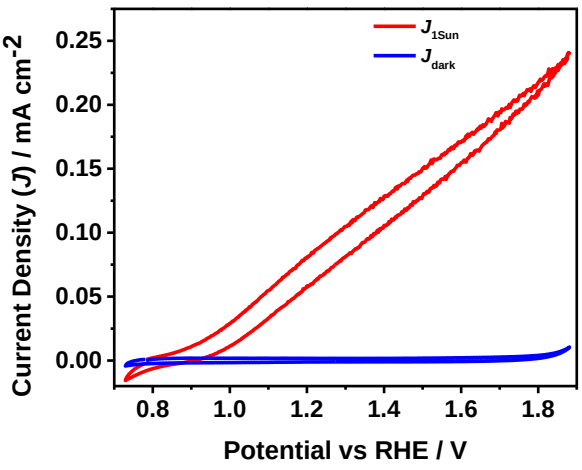

Figure 4.5: *J-V* responses of $CuWO_4$ electrode measured in 1.0 M Potassium borate buffer (KBi) at pH 9 in the dark (blue solid line) and under 1 Sun illumination (solid red line).

demonstrated the charging and discharging of surface states. These combined findings underscore the crucial role of surface states as intermediates during the OER process on $CuWO_4$.[3]

$CuWO_4$ has an indirect band gap of 2.3 eV, corresponding to an absorption edge around 540–560 nm.[7] This indicates that absorbance begins to rise within this wavelength range, transitioning from the visible to the UV region. The indirect nature of the band gap is evidenced by a gradual increase in absorption near the band edge, rather than a sharp cutoff. In the visible range (400–600 nm), charge transfer and *d-d* transitions involving Cu^{2+} ions are anticipated.[11] Additionally, a strong absorption band is observed in the UV region (300–400 nm), attributed to charge transfer transitions from oxygen *2p* orbitals to the metal cation orbitals (Cu^{2+} and W^{6+}).

For water oxidation, $CuWO_4$ can form oxo, peroxo, and superoxo species on its surface. Cu^{2+} ions may interact with molecular oxygen, resulting in the formation of transient complexes. While *d-d* transitions in $CuWO_4$ are typically Laporte-forbidden and therefore weak, they may become partially allowed due to vibronic coupling and the distorted octahedral coordination of Cu^{2+} ions.[11]

To investigate the presence of oxo, peroxo, or superoxo species in $CuWO_4$ systems, we utilized Photoinduced Absorption Spectroscopy (PIAS) at a low light intensity of 1 mW/cm^2, chosen to minimize vigorous O_2 evolution, although this may influence the transmittance data. In the PIAS setup, we first measured the current-voltage (*i-V*) performance under the reaction conditions and light intensity. As evident from *Figure 4.6* No significant UV absorption was observed in the 500-600 nm range, likely due to LaPorte forbidden transitions.[11] Our UV scans were limited to 475 nm due to experimental

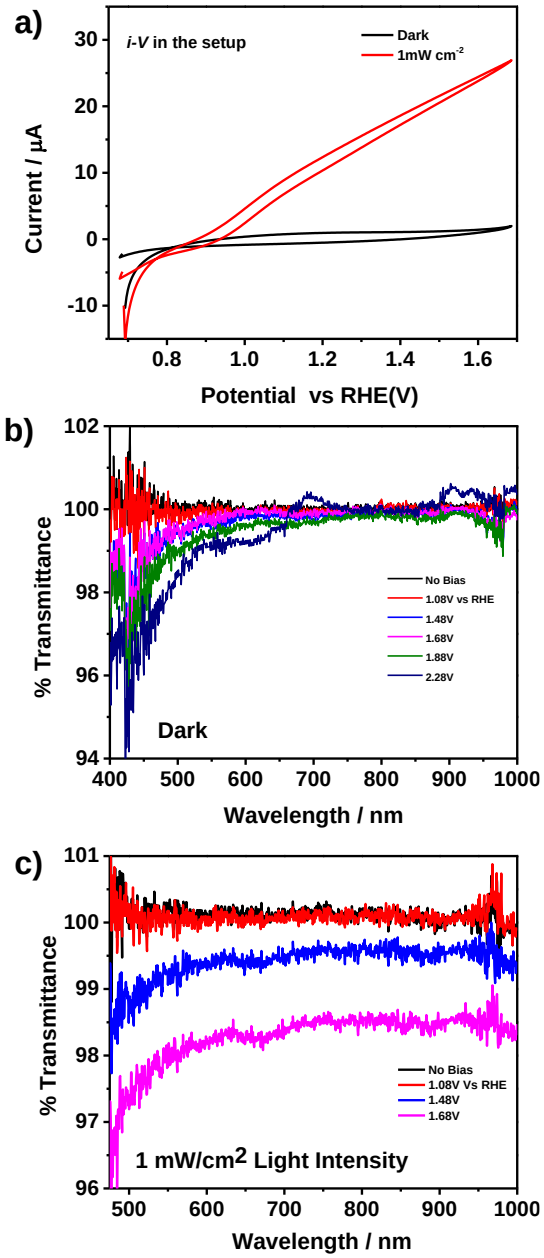

Figure 4.6: PIAS measurement in 1.0 M KBi in H_2O, pH 9. a) *i-V* response of $CuWO_4$ measured within the PIAS setup. b) in the dark. c) under monochromatic 405 nm laser and 1 mW/cm^2 intensity.

constraints and the use of a long-pass filter; however, under dark conditions, we extended the measurements into the UV range, revealing a notable peak around 440 nm. This peak

suggests the formation of intermediate species involving charge transfer transitions from oxygen *2p* orbitals to Cu^{2+} and W^{6+} ions. Initially, Cu^{2+} on the $CuWO_4$ surface can form oxo (Cu=O) and hydroxo (Cu–OH) species, which modify the local electronic structure. As the reaction progresses, more complex intermediates, such as peroxo (Cu-OOH) and superoxo ($Cu\text{-}O_2^-$) species, form from interactions between surface Cu^{2+} ions and adsorbed oxygen or water molecules. These intermediates facilitate charge transfer processes, contributing to the UV absorption peak. Furthermore, W^{6+} centers may participate in the reaction, enhancing charge transfer. The presence of these species confirms that $CuWO_4$ actively participates in the water oxidation process, with these intermediates playing a crucial role in catalysis.

This peak near 440 nm can be further verified in two ways: first, by reducing the working light intensity below 1 mW/cm² and optimizing the conditions to achieve a significant photocurrent while performing PIAS without the 475 nm long-pass filter. Second, an ATR-IR operando study could be conducted to provide additional verification. We also conducted an operando ATR-IR experiment. However, due to water's strong absorption in the expected range for oxo and peroxo vibrational modes (600-850 cm^{-1}) [12], we opted to use D_2O as the solvent to mitigate this issue (*Figure 4.7*). We prepared an electrolyte solution consisting of approximately 20 μL of 0.2 M KCl in D_2O. Initially, we measured the current-voltage (*j-V*) response to ensure that our system was operating correctly.

For the IR measurements, we held the $CuWO_4$ under a constant potential using chronoamperometry, starting the IR measurements only after three minutes to confirm system stability. Each spectrum was adjusted to reference the potential of 1.0 V_{RHE}, corresponding to the flatband potential where no photocurrent is expected.

In examining *Figure 4.8.a* and *Figure 4.8.b*, we observed a declining baseline, and post-experiment analysis revealed that the CuWO4 electrode appeared etched near the cathode. This etching suggests the potential production of acid, leading to a decrease in pH, which could destabilize the entire reaction setup. Similar phenomena 13 have previously been reported with WO3, where researchers conducted ICP-MS and chronoamperometry studies to investigate this issue. Therefore, before proceeding with ATR-IR measurements, it is essential to identify a suitable electrolyte that prevents etching. Then only optimized reaction setup will be achieved for further investigation of the surface state's chemical nature.

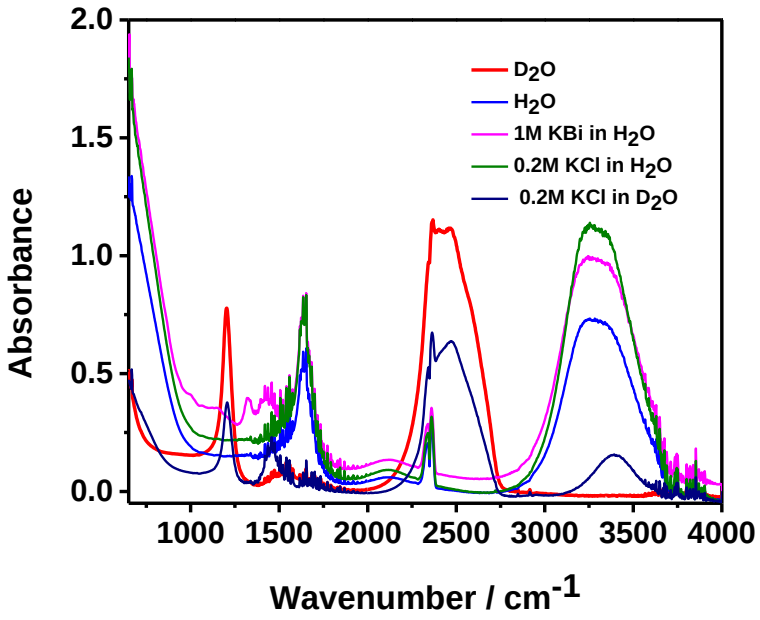

Figure 4.7: The Absorbance of the ZnSe ATR crystal in contact with D_2O (solid red line), H_2O (solid blue line), 1.0 M KBi in H_2O (solid majenta line), 0.2 M KCl in H_2O (solid olive line) and 0.2 M KCl in D_2O (solid deep blue line).

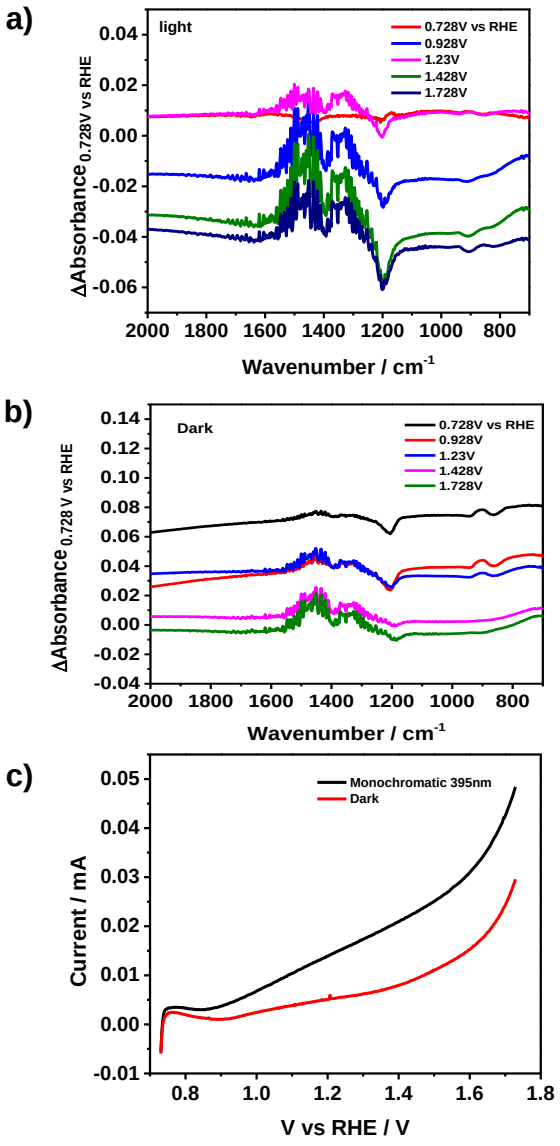

Figure 4.8: Operando ATR-IR measurement in 0.2 M KCl in D_2O. a) under monochromatic 395 nm illumination. b) in the dark. c) *i-V* response of $CuWO_4$ measured within the ATR-IR experimental setup. All the IR spectra were corrected with respect to the spectrum at flatband potential.

Despite the limitations of my experimental setup, we can still validate several observations that contribute to our conclusions. *Figure 4.8.a* and *Figure 4.8.b* shows a

small peak emerging at 750 cm^{-1}, accompanied by a decrease in the D_2O signal at 1200 cm^{-1}. The peak at 1500 cm^{-1} is attributed to the vibrational modes of the O-D bond stretch. The vibrational frequencies of the expected *oxo*, *peroxo*, and *superoxo* species are listed in the table below. Notably, the stretching mode of O-O in peroxides typically falls within the 730-920 cm^{-1} range, [12,14,15] suggesting that our observed peak at 750 cm^{-1} may indicate the formation of W-O-O-W/D or Cu-O-O-Cu/D surface states.

Species	Wavenumber (cm^{-1})	Species	Wavenumber (cm^{-1})
W=O	870-970[16,17]	Cu-O-O-Cu	832 [18]
W-O-O-D	900-950[19]	W-O-O·	1100-1300 [14,20]
W-O-O-W	900-950[19]	Cu-O-O·	1100-1300 [14]

Table 4.1: The list of potential functional groups and their anticipated IR absorption.

D_2O exhibits strong absorption in the 1100-1300 cm^{-1} region, where *superoxo* species are anticipated to appear. We conducted the same operando ATR-IR measurements in water (1.0 M KBi, pH = 9), but KBi also absorbs in the 1300-1700 cm^{-1} range, which limits our ability to investigate the IR characteristics of any surface states effectively. In *Figure 4.9,* some potential peak signatures are observed between 1050-1300 cm^{-1}, where we might expect superoxo species such as W-O-O or Cu-O-O. Distinguishing between W-O-O-W/D or Cu-O-O-Cu/D and W-O-O or Cu-O-O will be challenging. To address this, we could utilize isotope labeling; O-18 would be particularly useful for clearly identifying the

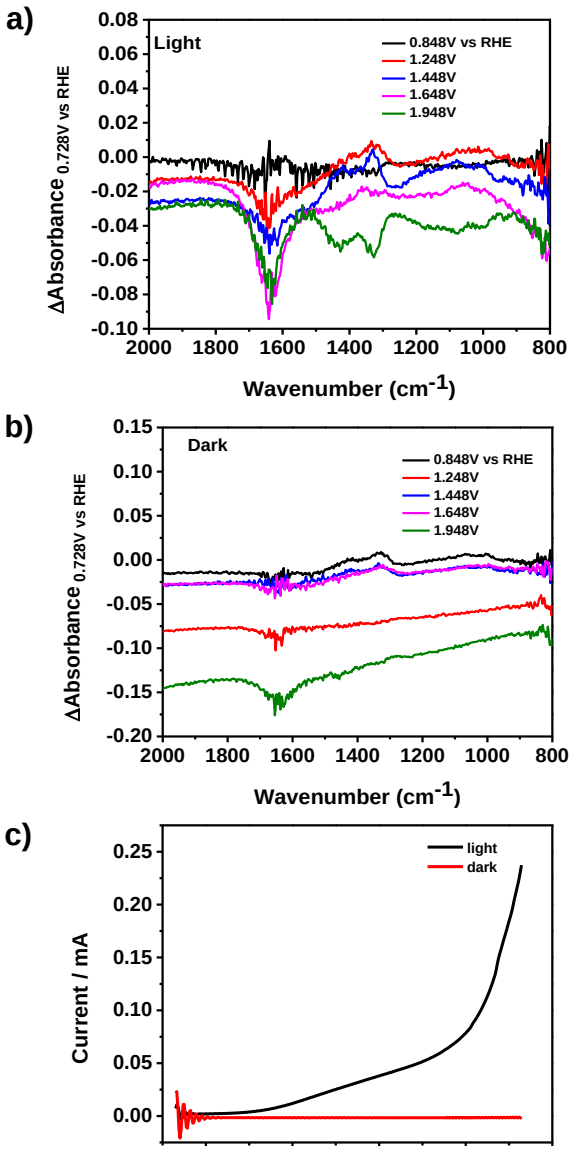

Figure 4.9: Operando ATR-IR measurement in 1.0 M KBi in H_2O, pH 9. a) under monochromatic 395 nm illumination. b) in the dark. c) *i-V* response of $CuWO_4$ measured within the ATR-IR experimental setup. All the IR spectra were corrected with respect to the spectrum at flatband potential.

species. involved in the OER of $CuWO_4$.

4.5 Conclusion

In this chapter, we examined the $CuWO_4$ electrode using PIAS and operando ATR-IR spectroscopy under PEC OER conditions. These experiments indicate the potential presence of oxo, peroxo, and superoxo surface states during the OER of $CuWO_4$. To gain further insights into the exact nature of these surface states, we need to address several key factors. First, we must identify a suitable electrolyte that prevents etching to ensure system stability and avoid corrosion. Second, during PIAS, we should utilize a very low intensity of 405 nm laser illumination (<1 mW/cm²) while ensuring the OER performance of $CuWO_4$ remains prominent. This may involve exploring different synthetic procedures, such as ALD or CVD, which could lead to fewer pinholes, reducing recombination and enhancing performance. Third, we can incorporate isotope labeling by selecting H_2O or D_2O for the operando ATR-IR measurements. Lastly, although ambitious, we could use isotope-labeled solvents during the synthesis of $CuWO_4$ thin films while adopt synthetic techniques that minimize the risk of air contamination.

REFERENCES

(1) Lhermitte, C. R.; Bartlett, B. M. Advancing the Chemistry of $CuWO_4$ for Photoelectrochemical Water Oxidation. *Acc Chem Res* **2016**, *49* (6), 1121–1129. https://doi.org/10.1021/acs.accounts.6b00045.

(2) Bohra, D.; Smith, W. A. Improved Charge Separation via Fe-Doping of Copper Tungstate Photoanodes. *Phys. Chem. Chem. Phys.* **2015**, *17* (15), 9857–9866. https://doi.org/10.1039/C4CP05565A.

(3) Gao, Y.; Hamann, T. W. Quantitative Hole Collection for Photoelectrochemical Water Oxidation with $CuWO_4$. *Chem. Commun.* **2017**, *53* (7), 1285–1288. https://doi.org/10.1039/C6CC09029J.

(4) Ye, W.; Chen, F.; Zhao, F.; Han, N.; Li, Y. $CuWO_4$ Nanoflake Array-Based Single-Junction and Heterojunction Photoanodes for Photoelectrochemical Water Oxidation. *ACS Appl Mater Interfaces* **2016**, *8* (14), 9211–9217. https://doi.org/10.1021/acsami.6b03176.

(5) Pyper, K. J.; Yourey, J. E.; Bartlett, B. M. Reactivity of $CuWO_4$ in Photoelectrochemical Water Oxidation Is Dictated by a Midgap Electronic State. *The Journal of Physical Chemistry C* **2013**, *117* (47), 24726–24732. https://doi.org/10.1021/jp408434v.

(6) Gao, Y.; Hamann, T. W. Elucidation of $CuWO_4$ Surface States During Photoelectrochemical Water Oxidation. *J Phys Chem Lett* **2017**, *8* (12), 2700–2704. https://doi.org/10.1021/acs.jpclett.7b00664.

(7) Lhermitte, C. R.; Bartlett, B. M. Advancing the Chemistry of $CuWO_4$ for Photoelectrochemical Water Oxidation. *Acc Chem Res* **2016**, *49* (6), 1121–1129. https://doi.org/10.1021/acs.accounts.6b00045.

(8) Zandi, O.; Hamann, T. W. Determination of Photoelectrochemical Water Oxidation Intermediates on Haematite Electrode Surfaces Using Operando Infrared Spectroscopy. *Nat Chem* **2016**, *8* (8), 778–783. https://doi.org/10.1038/nchem.2557.

(9) Shadabipour, P.; Raithel, A. L.; Hamann, T. W. Charge-Carrier Dynamics at the $CuWO_4$/Electrocatalyst Interface for Photoelectrochemical Water Oxidation. *ACS Appl Mater Interfaces* **2020**, *12* (45), 50592–50599. https://doi.org/10.1021/acsami.0c14705.

(10) Klahr, B.; Gimenez, S.; Fabregat-Santiago, F.; Hamann, T.; Bisquert, J. Water Oxidation at Hematite Photoelectrodes: The Role of Surface States. *J Am Chem Soc* **2012**, *134* (9), 4294–4302. https://doi.org/10.1021/ja210755h.

(11) Tian, C. M.; Jiang, M.; Tang, D.; Qiao, L.; Xiao, H. Y.; Oropeza, F. E.; Hofmann, J. P.; Hensen, E. J. M.; Tadich, A.; Li, W.; Qi, D. C.; Zhang, K. H. L. Elucidating the Electronic Structure of $CuWO_4$ Thin Films for Enhanced Photoelectrochemical Water Splitting. *J. Mater. Chem. A* **2019**, *7* (19), 11895–11907. https://doi.org/10.1039/C8TA12070F.

(12) Sivasankar, N.; Weare, W. W.; Frei, H. Direct Observation of a Hydroperoxide Surface Intermediate upon Visible Light-Driven Water Oxidation at an Ir Oxide Nanocluster Catalyst by Rapid-Scan FT-IR Spectroscopy. *J Am Chem Soc* **2011**, *133* (33), 12976–12979. https://doi.org/10.1021/ja205300a.

(13) Knöppel, J.; Kormányos, A.; Mayerhöfer, B.; Hofer, A.; Bierling, M.; Bachmann, J.; Thiele, S.; Cherevko, S. Photocorrosion of WO_3 Photoanodes in Different Electrolytes. *ACS Physical Chemistry Au* **2021**, *1* (1), 6–13. https://doi.org/10.1021/acsphyschemau.1c00004.

(14) Zhang, M.; de Respinis, M.; Frei, H. Time-Resolved Observations of Water Oxidation Intermediates on a Cobalt Oxide Nanoparticle Catalyst. *Nat Chem* **2014**, *6* (4), 362–367. https://doi.org/10.1038/nchem.1874.

(15) Bonnot, F.; Tremey, E.; von Stetten, D.; Rat, S.; Duval, S.; Carpentier, P.; Clemancey, M.; Desbois, A.; Nivière, V. Formation of High-Valent Iron–Oxo Species in Superoxide Reductase: Characterization by Resonance Raman Spectroscopy. *Angewandte Chemie International Edition* **2014**, *53* (23), 5926–5930. https://doi.org/https://doi.org/10.1002/anie.201400356.

(16) Rice, C. A.; Kroneck, P. M. H.; Spence, J. T. Tungsten(V)-Oxo and Tungsten(VI)-Dioxo Complexes with Oxygen, Nitrogen, and Sulfur Ligands. Electrochemical, Infrared, and Electron Paramagnetic Resonance Studies. *Inorg Chem* **1981**, *20* (7), 1996–2000. https://doi.org/10.1021/ic50221a012.

(17) Sugimoto, H.; Tano, H.; Tajima, R.; Miyake, H.; Tsukube, H.; Ohi, H.; Itoh, S. In Situ Generation of Oxo−sulfidobis(Dithiolene)Tungsten(VI) Complexes: Active-Site Models for the Aldehyde Ferredoxin Oxidoreductase Family of Tungsten Enzymes. *Inorg Chem* **2007**, *46* (21), 8460–8462. https://doi.org/10.1021/ic7012733.

(18) Root, D. E.; Mahroof-Tahir, M.; Karlin, K. D.; Solomon, E. I. Effect of Protonation

on Peroxo−Copper Bonding: Spectroscopic and Electronic Structure Study of $[Cu_2((UN-O-)(OOH)]^{2+}$. *Inorg Chem* **1998**, *37* (19), 4838–4848. https://doi.org/10.1021/ic980606c.

(19) Hazarika, P.; Kalita, D.; Sarmah, S.; Islam, N. s. New Oxo-Bridged Peroxotungsten Complexes Containing Biogenic Co-Ligand as Potent Inhibitors of Alkaline Phosphatase Activity. *Mol Cell Biochem* **2006**, *284* (1), 39–47. https://doi.org/10.1007/s11010-005-9011-8.

(20) Solomon, E. I.; Tuczek, F.; Root, D. E.; Brown, C. A. Spectroscopy of Binuclear Dioxygen Complexes. *Chem Rev* **1994**, *94* (3), 827–856. https://doi.org/10.1021/cr00027a013.

Chapter 5:

Conclusion and Future Directions

5.1 Conclusion

This research provides substantial insights into photoelectrochemical (PEC) water splitting, focusing on n-type metal oxide semiconductors as photoanodes for the oxygen evolution reaction (OER). The study centers on Hematite, synthesized via Atomic Layer Deposition (ALD), and $CuWO_4$, synthesized by Spray Pyrolysis. Each synthesis process was precisely optimized, offering scalable routes for material production with potential for further refinement. The synthesized semiconductors underwent detailed characterization through advanced spectroscopic techniques, including PXRD, Raman, UV-Vis, SEM, and XPS. This work addresses key challenges in charge separation, surface state dynamics, and intermediate formation, with each chapter's findings enhancing our understanding of material optimization for water-splitting applications.

- In earlier models of the OER,[1–3] the rate of oxygen production was thought to depend only on the density of holes at the surface, without any change in band positions or the water oxidation rate constant (k_{wo}). Our work in *Chapter 2* shows that increasing light intensity creates a significant shift of both Conduction and Valence Band Edges and moves it closer to the thermodynamic OER potential of $1.23V_{RHE}$. This shift reduces the external voltage needed for OER, making the process more efficient by aligning the semiconductor's energy bands favorably under light. Through photoelectrochemical impedance spectroscopy (EIS), we observed that as light intensity rises, the holes at surface state also increases until it levels off. This leveling indicates a bottleneck in the reaction, where sufficient charge build-up at the interface is essential to drive the multi-hole OER process.
- The higher photocurrent under intense illumination is primarily due to an increase in

k_{wo}, which accelerates hole transfer from the semiconductor to the electrolyte, subsequently reducing charge transfer resistance, supporting this observation. Thus disproves the primary assumption of the previous models, where it was assumed to be unchanged under various illuminations.

- *Chapter 2* explores two possible hypotheses for the mechanism of the multi-electron OER process under intense illumination. The *first hypothesis* suggests that under high light intensity, the band edges shift upwards, closer to the thermodynamic potential, additionally the rate of hole transfer from the semiconductor interface (surface state) to the solution increases. However, even after the hole density reaches saturation, OER continues to increase, raising questions about whether an alternative pathway exists for hole transfer. The second hypothesis proposes that while Fe^{IV}=O is known as the primary surface state where holes accumulate, another surface state might also participate in OER. If holes accumulate at this unidentified surface state and have a different transfer rate (k_{wo}) than those at the iron-oxo site, this parallel pathway could make the OER mechanism more complex, suggesting multiple active sites for hole transfer.
- *Chapter 3* investigates the second hypothesis introduced earlier. Our results suggest that modifying hematite's surface with a gallium monolayer may lead to the formation of a iron peroxo species during OER under light. This peroxo species seems to act as a "spectator," accumulating holes in the rate limiting step that eventually recombine, indicating that multiple surface states may play a role in water oxidation. This adds complexity to the typical 4-electron pathway, as it appears that both iron-oxo and peroxo states participate in OER on hematite, with these states possibly interchanging

dynamically. Understanding the exact nature and kinetics of this peroxo state remains a challenging task, underscoring the complexity of the OER mechanism on hematite.

- In *Chapter 4*, we aimed to understand the chemical nature of $CuWO_4$'s surface states to explore its OER mechanism. We used Photoinduced Absorption Spectroscopy (PIAS) and operando ATR-IR spectroscopy under PEC OER conditions. While PIAS didn't provide information on surface states, ATR-IR revealed the presence of oxo, peroxo, and superoxo surface states during OER. To further investigate these states, we identified several key points: first, selecting an electrolyte that prevents etching to maintain stability and avoid corrosion; second, ensuring high-quality $CuWO_4$ synthesis, as this can limit surface state detection in in-situ studies; third, using isotope labeling with H_2O or D_2O in ATR-IR measurements to gain more insights into surface states; and finally, employing isotope-labeled solvents during synthesis to help detect surface states in both PIAS and ATR-IR.

5.2 Future Directions

Understanding the mechanism of OER is crucial for deploying suitable electrocatalysts that can improve the efficiency of oxygen formation, which will ultimately reduce the cost of green hydrogen production at the R&D level. Based on the findings of this work, several open questions remain regarding hematite OER:

- If multiple surface states exist, what is the exact chemical nature of the peroxo species we expect, as discussed in *Chapter 3* to support our second hypothesis?
- Experimentally, detecting the 'Spectator' surface state is also challenging. While *operando* ATR-IR was used to detect species previously[4], the choice of electrolyte should be reconsidered. Additionally, the peroxo species is expected to be dynamic, making it nearly impossible to detect its stable form spectroscopically.
- Different synthetic methods have revealed varying surface chemistries of hematite during OER, the mechanism must be uniform across all synthetic methods. Instead of using ALD, we employed electrodeposition techniques to fabricate hematite to build on our work at *Chapter 2*.

Hematite electrodes were prepared by electrodepositing FeOOH from an $FeCl_2$ solution using a modified method[5]. Acidic electrodeposition was performed in 0.1 M $FeCl_2 \cdot 4H_2O$ (pH 4.2) at 60°C, applying 1.2 V vs. Ag/AgCl under gentle stirring. The film thickness was controlled by deposition time (total charge passed). This method produced planar films with excellent uniformity and reproducibility. After deposition, the electrodes were annealed at 800°C by placing them on a flat Si wafer in a preheated furnace for 10 minutes, followed by quenching at room temperature.

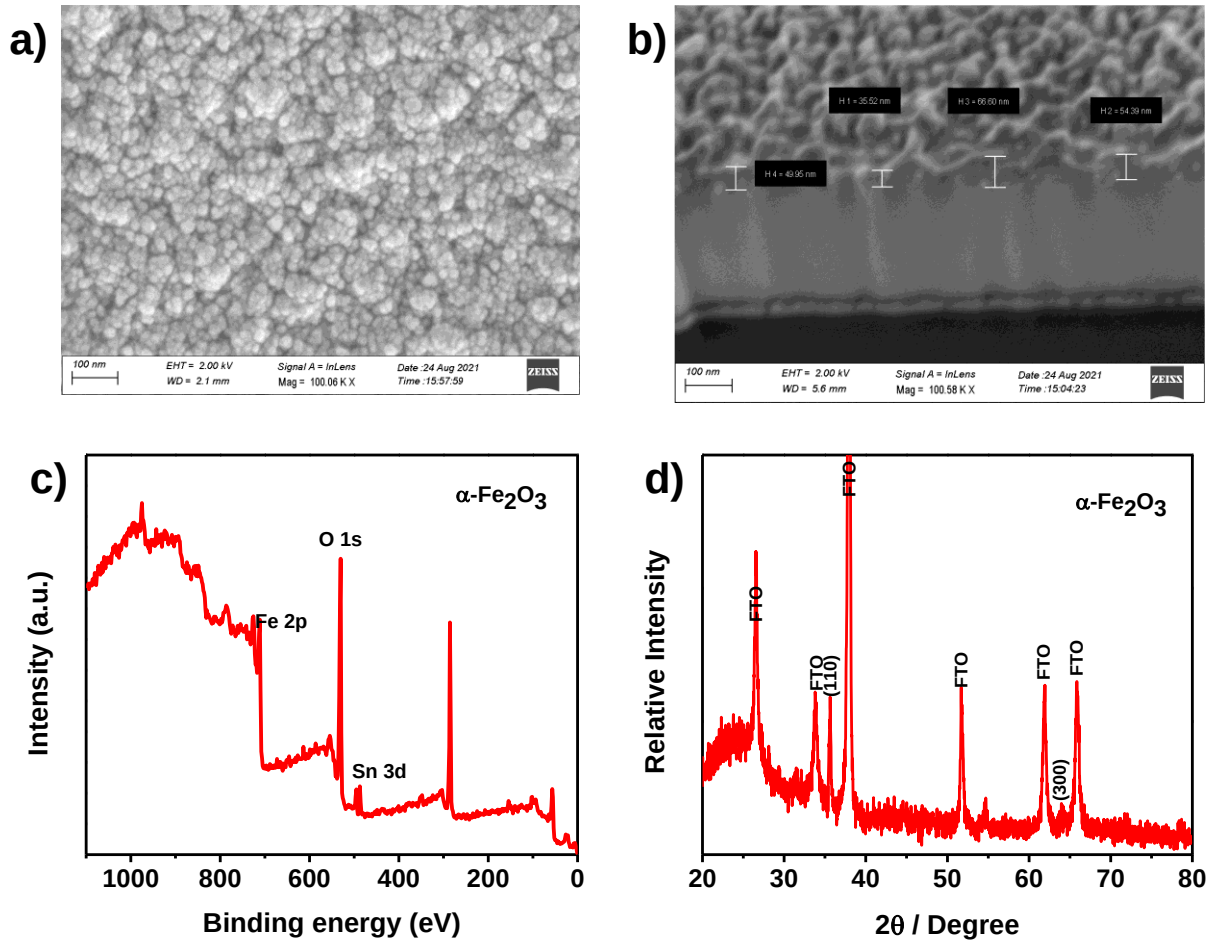

Figure 5.1: Anodic electrodeposition technique produces ED-Hematite. a) Uniform surface of ED-Hematite under SEM, b) Cross section SEM was performed to determine the thickness of the film on FTO substrate, which is 51 nm, c) XPS data, d) PXRD data.

The electrodeposited hematite sample (ED-Hematite) was prepared by 30 minutes of anodic deposition followed by 10 minutes of annealing at 800°C. The sample was thoroughly characterized using XPS, PXRD, and SEM. The cross-sectional SEM (*Figure 5.1.b*) shows the sample thickness to be approximately ~50 nm. Previous work in our lab has demonstrated that ED-Hematite outperforms[6] ALD-Hematite in OER performance in alkaline media, and our results further support this finding. The characterization results in *Figure 5.1* and *j-V (Figure 5.2.a)* measurements align well with our previous work.

However, during EIS studies, we observed some interesting phenomena that could help strengthen our peroxo hypothesis and its role in the kinetics of OER for hematite.

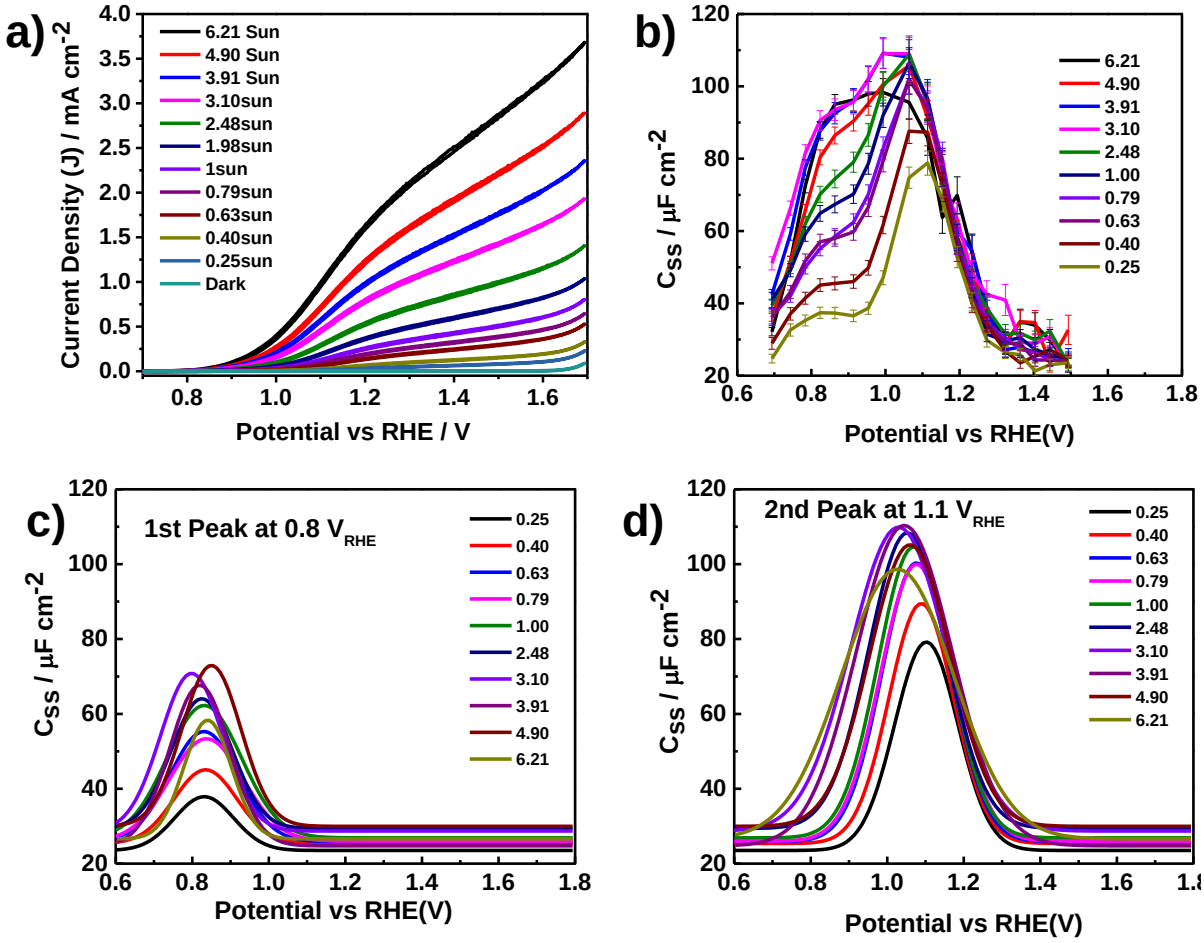

Figure 5.2: All electrochemical measurements ED-Hematite was performed in a similar setup used in Chapter 2, keeping the temperature variable constant a) *j-V* performance in 1 M KOH pH 13.6 electrolyte, where the scan rate is 20 mV/s, b) C_{ss} plot against applied potential vs RHE, derived from Nyquist plots obtained from EIS, The C_{ss} plots were fitted with bi-gaussian function to deconvolute both the peaks and plotted separately in c) and d), The C_{ss} curves were integrated in the wide potential region and quantified using the technique previously mentioned in *Chapter 2* to produce e).

Figure 5.2 (cont'd)

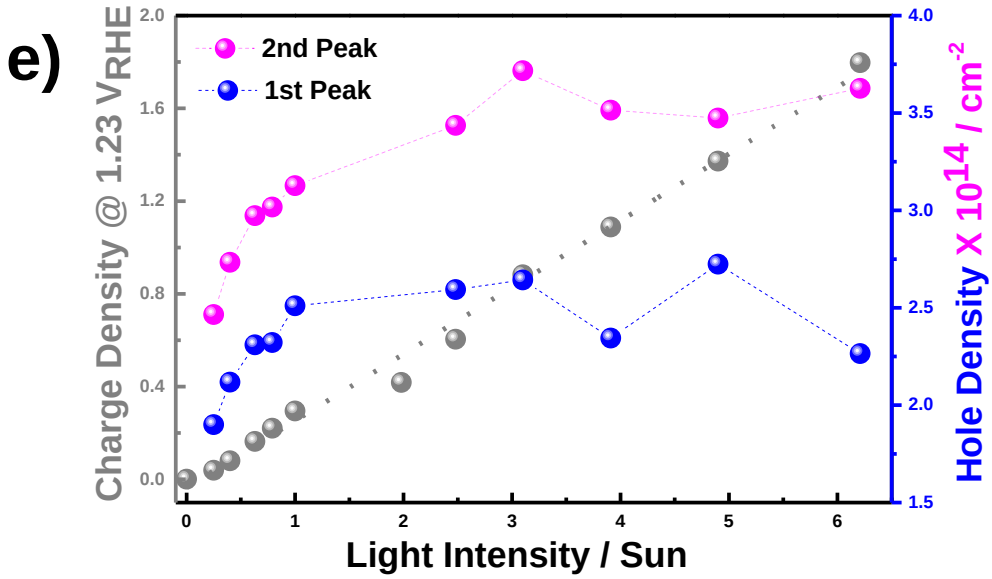

EIS data in *Figure 5.2.b* was analyzed (process explained in *Chapter 2*) by fitting the Nyquist plot to equivalent circuits, with surface state capacitance (C_{ss}) plotted against applied voltage. Unlike ALD-Hematite, ED-Hematite shows an additional peak at 0.8 V_{RHE}, which has also been observed in a recent hematite study, although its role in OER was not explored. The C_{ss} peaks were fitted with a bi-Gaussian function, revealing that both peaks behave similarly during OER, suggesting they represent hole accumulation prior to OER. The peaks saturate with increasing light intensity (*Figure 5.2.e)*, similar to ALD-Hematite (*Chapter 2*). While both peaks appear to participate in OER, it remains unclear whether they are dynamic or interchangeable. One peak at 1.1 V_{RHE} corresponds to the well-established iron-oxo surface state, while the state at 0.8 V_{RHE}, as discussed in *Chapter 3*, can be assumed to be the 'Spectator State' or peroxo surface state. Both surface states actively participate in OER, and further investigations, including Tafel and

Mott-Schottky analyses, are needed to understand the hole transfer rate at the ‘Spectator State’ and its role in the OER mechanism.

- To explore the surface states involved in the OER of $CuWO_4$, it is crucial to select a suitable electrolyte to prevent corrosion. Proper isotope labeling of the electrolyte should also be performed to identify the chemical nature of the oxo / peroxo surface / superoxo states. Alternatively, isotopic labeling of Cu or W during synthesis could help further clarify the surface states, though this approach can be costly and experimentally challenging.

REFERENCES

(1) Righi, G.; Plescher, J.; Schmidt, F.-P.; Campen, R. K.; Fabris, S.; Knop-Gericke, A.; Schlögl, R.; Jones, T. E.; Teschner, D.; Piccinin, S. On the Origin of Multihole Oxygen Evolution in Haematite Photoanodes. *Nat Catal* **2022**, *5* (10), 888–899. https://doi.org/10.1038/s41929-022-00845-9.

(2) Mesa, C. A.; Francàs, L.; Yang, K. R.; Garrido-Barros, P.; Pastor, E.; Ma, Y.; Kafizas, A.; Rosser, T. E.; Mayer, M. T.; Reisner, E.; Grätzel, M.; Batista, V. S.; Durrant, J. R. Multihole Water Oxidation Catalysis on Haematite Photoanodes Revealed by Operando Spectroelectrochemistry and DFT. *Nat Chem* **2020**, *12* (1), 82–89. https://doi.org/10.1038/s41557-019-0347-1.

(3) Le Formal, F.; Pastor, E.; Tilley, S. D.; Mesa, C. A.; Pendlebury, S. R.; Grätzel, M.; Durrant, J. R. Rate Law Analysis of Water Oxidation on a Hematite Surface. *J Am Chem Soc* **2015**, *137* (20), 6629–6637. https://doi.org/10.1021/jacs.5b02576.

(4) Zhang, Y.; Zhang, H.; Liu, A.; Chen, C.; Song, W.; Zhao, J. Rate-Limiting O–O Bond Formation Pathways for Water Oxidation on Hematite Photoanode. *J Am Chem Soc* **2018**, *140* (9), 3264–3269. https://doi.org/10.1021/jacs.7b10979.

(5) Spray, R. L.; Choi, K.-S. Photoactivity of Transparent Nanocrystalline Fe_2O_3 Electrodes Prepared via Anodic Electrodeposition. *Chemistry of Materials* **2009**, *21* (15), 3701–3709. https://doi.org/10.1021/cm803099k.

(6) Zandi, O.; Schon, A. R.; Hajibabaei, H.; Hamann, T. W. Enhanced Charge Separation and Collection in High-Performance Electrodeposited Hematite Films. *Chemistry of Materials* **2016**, *28* (3), 765–771. https://doi.org/10.1021/acs.chemmater.5b03707.